1-1-2014

Analysis Of A Dual Scissored-Pair,variable-Speed, Control Moment Gyroscope Driven Spherical Robot

Richard Chase
Wayne State University,

ANALYSIS OF A DUAL SCISSORED-PAIR,VARIABLE-SPEED, CONTROL MOMENT GYROSCOPE DRIVEN SPHERICAL ROBOT

by

RICHARD CHASE

DISSERTATION

Submitted to the Graduate School

of Wayne State University,

Detroit, Michigan

in partial fulfillment of the requirements

for the degree of

DOCTOR OF PHILOSOPHY

2014

MAJOR: ELECTRICAL ENGINEERING

Approved by:

_____

Advisor Date

_____

_____

_____

_____

DEDICATION

The exports of Libya are numerous in amount. One thing they export is corn, or as the Indians call it, "maize". Another famous Indian was "Crazy Horse". In conclusion, Libya is a land of contrast. Thank you.

TABLE OF CONTENTS

LIST OF TABLES

LIST OF FIGURES

VARIABLE LIST

Variable	Desription (All units are in SI)
α_n	Angular acceleration described by n
avg	Subscript for "average"
Δ	Steady state oscillation of a scissored-pair system
Δ^2	Steady state oscillation of a dual scissored-pair system
$\hat{\mathbf{e}}_n^{(x)}$	Direction n of frame x
g	Subscript for "gimbal"
H_n	Angular momentum described by n
h_n	Height of body n
m_n	Mass of body n
ω_n	Angular velocity described by n
$\Omega_n^{[x]}$	Angular velocity of linked-pair x in direction n with respect to the inertial frame
P_n	Power described by n
ϕ_n	Angle described by n
r	Subscript for "rotor"
r_n	Radius of small body n
R_n	Radius of larger body n
ρ_n	Density of body n
sp	Subscript for "Scissored-pair"
t_n	Time duration of event n
τ_n	Torque described by n
θ_n	Angle described by n
v	Translational velocity of body n
$x^{Y/Z}$	Variable x of frame Y with respect to frame Z

Table 1: Variable List

Chapter 1: A Review of Active Mechanical Driving Principles of Spherical Robots

Chapter Abstract

Spherical robotics is an emerging research field due to a ball's characteristic to be holonomic, have a sealed internal environment, and rebound from collisions easily. As the research moves forward, individual groups have begun to develop unique methods of propulsion, each having distinctive engineering trade-offs: weight is sacrificed for power; speed is forfeited for control accuracy, etc. Early spherical robots operated similar to a hamster ball and had a limited torque and a high-energy loss due to internal friction. Researchers have begun to develop various novel concepts to maneuver and control this family of robot. This chapter is an overview of the current research directions that various groups have taken, the nomenclature used in this subdiscipline, and the various uses of the fundamental principles of physics for propelling a spherical robot.

1.1 Introduction

Spherical robots are a promising area of research and have many unique features that are of interest to study. They can be designed to be sealed off from harsh environments, to operate holonomically (For the purpose of this paper, a holonomic system will be referred to in the robotics sense and not in the multi-body dynamics sense. A holonomic system in robotics is one whose orientation does not affect its desired direction of travel. For example, an automobile must point its front end towards its intended direction of travel. A spherical robot, if designed so, may change direction at any stage of movement without reorientating itself), and to rebound from collisions in a quick and non-destructive manner [1]. Spherical robots have begun to be used in underwater experiments [2, 3], child development studies [4], and security reconnaissance [5, 6, 7]. Some researchers have even begun to develop swarms of these of robots for task execution [8]. Due to the nature of a ball, a robot with a spherical shell will also follow the path of least resistance. The quintessential spherical robot would have true holonomy and hence would be able to move in any direction without having to change its orientation. The current research direction of spherical robots is heavily focused on the internal mechanics and the corresponding control systems. One design has not yet emerged dominantly among the others and diverse methodologies of internal driving mechanics have resulted in a wide range of robotic characteristics and capabilities. Due to the fact that research efforts are sporadic and uncoordinated, researchers have yet to create an optimized and efficient system [9].

Typically, the drive system of the spherical robot is located inside a shell. In order for the outer shell to rotate, the drive system must be able to transfer power to the outer shell in some manner: a fixed mechanical component such as a gear, an electromagnetic device such as a motor, etc. For true holonomy, the research challenge becomes developing an internal drive mechanism that can provide omnidirectional output torque to a sphere that can arbitrarily rotate around it, regardless of the orientation of either the sphere or the drive mechanism. In essence, the inner mechanics must be able to rotate three-

dimensionally independently from the outer shell. Since the outer shell must be connected to the inner mechanics in some manner, this poses a difficult design challenge. However, there are numerous ways to solve this problem, but each method has its own set of obstacles.

These obstacles have spawned many variations of internal propulsion devices, each one trading torque for holonomy, control for speed, etc. Some of these systems are simple, and some have complicated designs with even more complicated control algorithms. Teams have even begun to research propulsion by physically transforming the outer shell, which may lead to an entirely new family of robots. The following is a review of spherical robot internal-drive concepts and novel variations, the first being designs based on the concept of barycenter offset. The early and current majority of designs are based on the principle of shifting the equilibrium of a sphere [1], the most common of which is shifting the sphere's center of gravity.

This research has four main objectives. The first objective is to explore the current state of the art and develop an understanding of what the current obstacles in the field are. The second object is to propose a new type of spherical robot drive train that may perform better than the current state of the art. The third objective will be to develop a set of equations that will calculate key performance characteristics of spherical robots. This equation set will allow cross platform spherical robot designs to be compared in a controlled environment. The fourth objective will be to perform a series of parametric analysis using this equation set on the current state of the art designs and the design proposed in objective two. This research hopes to prove that designs using control moment gyroscopes will be more agile than designs that simply shift the center of mass.

This first chapter discusses the three major types of principles used to propel a spherical robot: barycenter offset (BCO) in Section 1.2, shell transformation (ST) in Section 1.3, and conservation of angular momentum (COAM) in Section 1.4. In the discussion of each type of principle, examples of how these types of principles are utilized will be discussed in the respective subsections. Also, novel enhancements such as legs, sensors,

and reconfiguration are discussed where appropriate. Finally, a table of taxonomy in Section 1.5 will be presented showing the principles, basic utilizations, and power limitations associated with each.

1.2 Barycenter Offset (BCO)

The term *barycenter offset* is used in spherical robots to describe the act of shifting a robot's center of mass (the barycenter) in order to produce a desired motion. Consider a robotic sphere resting in equilibrium. As its internal mechanisms move, the mass distribution of the ball will be shifted, causing the ball to roll to a new position of equilibrium. With proper timing and control methodologies, the robot can move smoothly through its environment. However, the main limitation of this method is that the maximum output torque is constrained because the center of gravity cannot be shifted outside of the shell. This can best be illustrated by picturing a pendulum inside a sphere, which is a common and straightforward design. A simplified two-dimensional model (See Figure 1.1) illustrates the torque that can be generated and mechanically applied to the outer shell. A weighted bob of a given mass swings on an armature about a support rod located through the center axis of the robot. As the bob rotates, the center of mass rotates accordingly and the robot rolls to equilibrium. The maximum value of the torque that can be applied

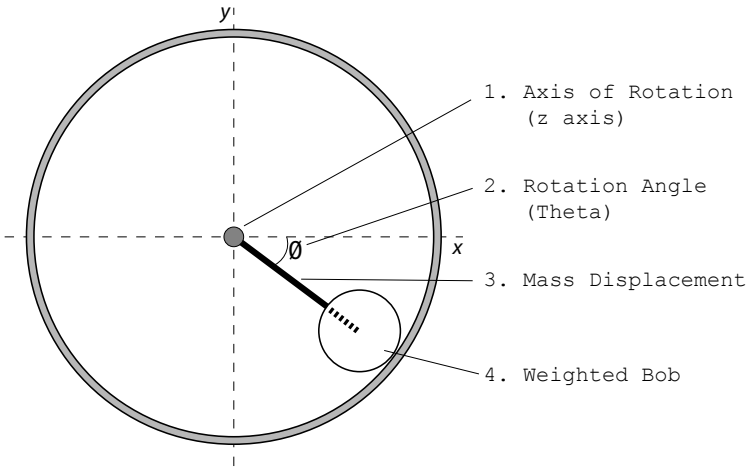

Figure 1.1: Cross section of a spherical robot model illustrating the pendulum drive armature and weighted bob.

is

$$\tau_{max} = mgr * \sin(\theta) \tag{1.1}$$

where τ is the output torque about the z-axis (Figure 1.1, item 1), mg is the weight of the bob (Figure 1.1, item 4), r is the displacement of the bob's center of mass from the shell's center of mass (Figure 1.1, item 3), and $\sin(\theta)$ corresponds to the rotation angle from the horizontal (Figure 1.1, item 2). What follows are variations of the barycenter offset designs.

1.2 Implementations of Governing Principle

Hamster Ball

An early design of a barycenter offset system is what is commonly referred to as the hamster ball design [10]. The design is nicknamed this because, simply enough, it mimics a hamster in a toy ball. A small-wheeled robot is placed inside the ball, in most cases a small remote control car, and the weight of the robot provides enough force to propel the robot when it moves (Figure 1.2). The shell is navigated non-holonomically similar to a car. The heading of the internal robot must be changed in order to change the direction of travel. Single-wheeled or multi-wheeled vehicles can be utilized, and a four-wheeled differential-drive vehicle will create different motion curves as opposed to a single wheeled vehicle [10]. A four-wheel drive system can act as a differential drive, giving the robot the ability to turn in place, which adds holonomic characteristics to the vehicle. Furthermore, the design is relatively easy to model, fabricate, and control. As long as the end task does not require extremely accurate tracking, control is fairly simple as well being that it maneuvers as any type of basic remote control car would maneuver. One of the major drawbacks is that some slipping of the internal robot or driving mechanism usually occurs. However, a closed loop control system combined with appropriate internal tracking sensors can calculate this slippage and may mitigate the problem [10]. Aside from the energy loss and control complications due to friction, another pitfall of this design is the behavior of the robot when it becomes airborne during vibration or encountering

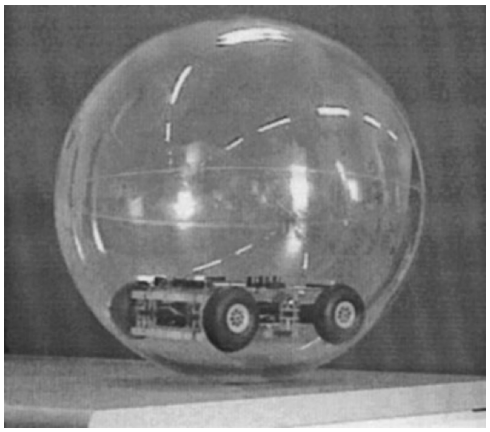

Figure 1.2: Prototype of a Hamster Ball design [10].

bumps. When the internal vehicle becomes airborne, traction between the shell and the internal robot's wheels becomes zero, and the shell will lose momentum. Furthermore, positional tracking may be affected. Although this problem can be somewhat managed with sensors and a proper control system, in tasks where accuracy of navigation is crucial, this shifting issue is unacceptable.

Internal Drive Unit (IDU)

To circumvent the shifting issue associated with an internal robot, a few barycenter offset designs have incorporated a system that forces the robot's wheels to be in constant contact with the outer shell, either by a spring-loaded or fixed mechanism. In a spring-loaded design, a rod and spring are attached to the top of the internal robot and then pressed up against the shell, forcing the wheels to be in constant contact with the shell. Attached on the top of the spring is a 3-degree-of-freedom (DOF) ball bearing that allows the spring to travel along the surface of the inner shell with little friction (Figure 1.3). One of the benefits of having a constant contact between the wheelbase and shell is that the mean speed of the ball can be easily controlled by the motor wheel speed, and at low speeds, the directional control of the system is moderately accurate [1]. The nature of the IDU also allows the system to have either a sealed or a honeycomb outer shell. As long as the wheels are larger than the holes in the outer shell, the robot will continue to operate. Furthermore, this is a simple system to design and is relatively inexpensive

to manufacture. It is an excellent research platform that can be used in academia but has challenges operating in real-world situations. Although this is still a commonly used

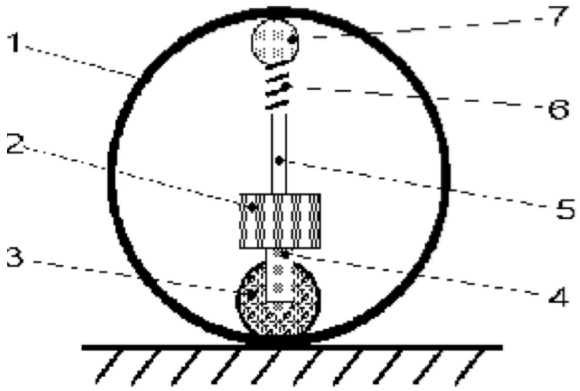

Figure 1.3: Structure of Spring-Loaded Design. 1. robot body (case), 2. controlling box, 3. driving wheel, 4. steering axis, 5. supporting axis, 6. spring, 7. balance wheel [1].

low-cost design, at high speeds an IDU-based robot's heading is difficult to control [1]. Slipping between the wheels and the shell can occur, as well as slipping between the shell and the medium it is traveling on. Slippage issues between the wheel and the shell can be minimized by adjusting the tension between the spring-loaded system and the internal robot, but a tighter fit means higher friction forces throughout the robot. Furthermore, an IDU system cannot make use of stored momentum: if the wheels stop, the robot will behave erratically. An IDU system traveling down a small incline must use power to keep its wheels spinning in order to move: it cannot roll down small inclines without assistance. On the other hand, rolling down steep inclines without controlled power from the internal mechanisms will cause unpredictable movement. From a design perspective, the IDU system must also be extremely well balanced. An off-axis center of mass may cause the robot to travel in an unwanted pattern.

Universal Wheel

Another design that incorporates the principles of barycenter offset is BHQ-3 [11]. The BHQ series of robots derive their name from the fact that their dynamic model was established from the Boltzmann-Hamel equation. This design is a combination of the hamster wheel and the previous IDU design. It can be conceptualized as a universal

wheel type system: the interior drive mechanism can rotate freely on the inside of the robot due to the combination of wheels attached to it. The IDU in the BHQ-3 is designed such that the internal mechanics will not shift when encountering bumpy terrains (Figure 1.4). Two DC drive motors control the robot: one motor controls the orientation of the IDU, and one motor controls the speed of the drive wheel. This allows the ball to move with a zero turning radius, creating a higher degree of holonomy than the previously described robots. In addition to having the ability to maneuver itself by the use of barycenter offset, the robot's velocity is also controlled by the angular velocity of the driving wheel. As the wheel spins faster, the translational velocity of the robot increases. This means that the internal weight of the IDU is not the only factor controlling the momentum of the robot. This particular robot is able to travel in water, sand, as well as up a small slope. However, it may have high energy loss due to friction from the sponge wheels as well as the inability to roll unpowered down a slope, depending on the motors and control method used. The HIT Spherical Robot [12] was designed to behave

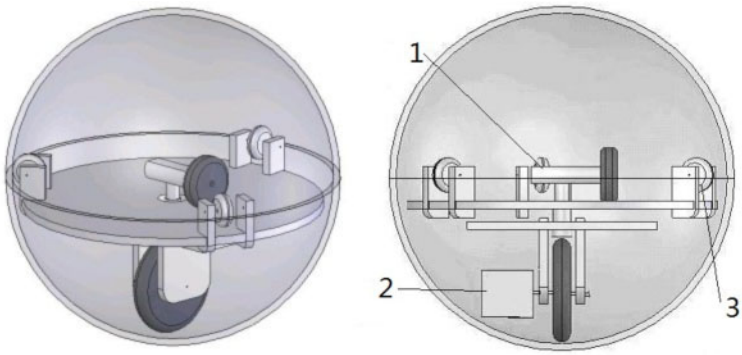

Figure 1.4: Structure of BHQ-3: 1–Motor, 2–Motor, 3–Sponge wheels [11].

in a manner where the steering and driving mechanisms are independent of one another (Figure 1.5). In a pendulum-based designed, the steering and turning mechanisms are dependent on each other, creating a non-holonomic robot. For a robot to be able to move in any direction regardless of orientation (holonomy), the steering and driving mechanisms must be mechanically independent. HIT is only controlled by two motors: a turning and a driving motor. The turning motor (Item 1, Figure 1.4) rotates the entire inner assembly

of the robot along a rim at the equator, and the driving motor (Item 2, Figure 1.4) shifts the center of gravity of the robot, causing it to move.

Figure 1.5: A picture of HIT and its internal driving mechanism [12].

Pendulum Driven

A popular design used by industry and academia is a pendulum-driven design (Figure 1.6). The pendulum model consists of a fixed shaft through the center of the outer shell of the robot, with a pendulum and bob that rotates around the shaft. Rotating the pendulum shifts the center of mass outward from the center and the shell begins to roll. Shifting the pendulum left or right along the equator will shift the center of mass left or right, and the robot will begin to turn in the corresponding direction. Shown in Figure 1.6 below is a photo of a commercialized pendulum robot, Rotundus. As the weight of

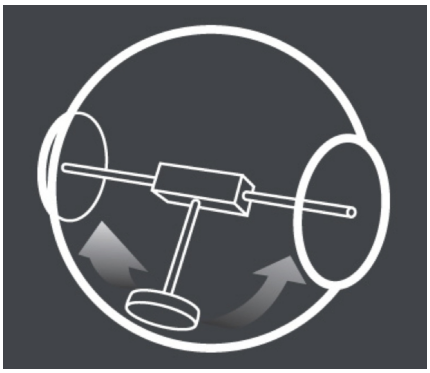

Figure 1.6: A commercialized pendulum-driven robot, Rotundus [13].

the bob increases, so does the amount of torque that can be used to drive the robot. However, a heavier bob means a heavier robot. The most notable setback to this design is its inability to go up a steep slope. If the bob is where the majority of the weight of the system is located, the robot can go up a steep slope. However, in practice, a well designed spherical robot can usually only go up about a 30° slope [14]. A spherical robot that can traverse an incline greater than 30° may require design techniques that are not commercially or economically practical. Even though there are some limitations to the pendulum drive, it is a low-power easy-to-implement design that allows the shell to be sealed. Rotundus can roll at speeds of 6mph, through snow, ice, mud, and sand, and can float. In addition, it can carry a 1.81 kg payload [13]. One drawback to this design is that the movement of the shell is non-holonomic: there is a turning radius associated with its movement. Like all other barycenter offset designs, the center of mass cannot be shifted outside of the boundaries of the shell. It is also important to consider that as the radius of the shell becomes larger and the pendulum bob becomes more massive, the output torque increases. However, as these items become larger, the energy required to move them also becomes larger. There is a delicate balance of design when considering material compositions and the physical sizes of the internal elements. Designed to be a child's toy,

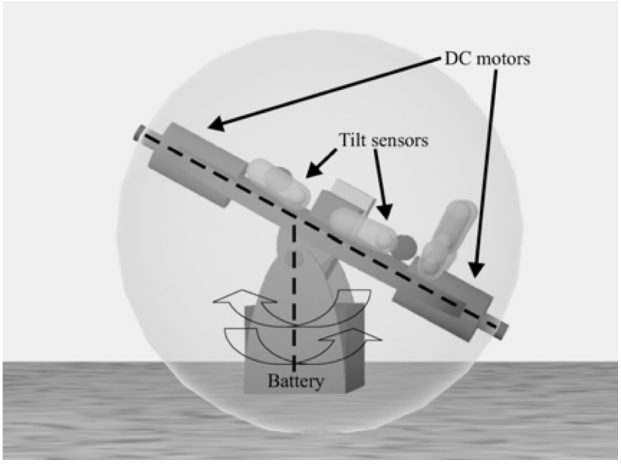

Figure 1.7: Rear view of Roball's steering mechanism [15].

Roball [15] is a pendulum-based spherical robot with an added tilt mechanism allowing it to turn as shown in Figure 1.7. The robot was designed to operate in unconstrained

environments and have minimal cost and complexity. Onboard sensors allow the robot to navigate its environment autonomously. All elements are placed on a plateau of the robot (the equator), and steering is done using a counterweight. In this particular model, the counterweight is a battery. In this design, the counter weight is designed to stay at the bottom of the shell, and the shell moves around it, causing propulsion. In previous examples, the internal masses are designed to move within the shell and the robot rolls to equilibrium.

Double Pendulum

Another novel concept proposed in recent literature is a drive system with two pendulums on the inside. B. Zhao proposes such a device with an elliptical shell. Paired with a double pendulum, this allows the robot to turn in place [16, 17]. Parameters such as speed and maximum incline are not optimized in this design because the research is focused mainly on proof of concept and path planning. Springs are added to the system to dampen impacts on the internal mechanisms when traversing rough terrain or large bumps. The literature presents the theory, which is verified by simulation, and is then demonstrated on a proof-of-concept physical prototype (Figure 1.8). The robot is able

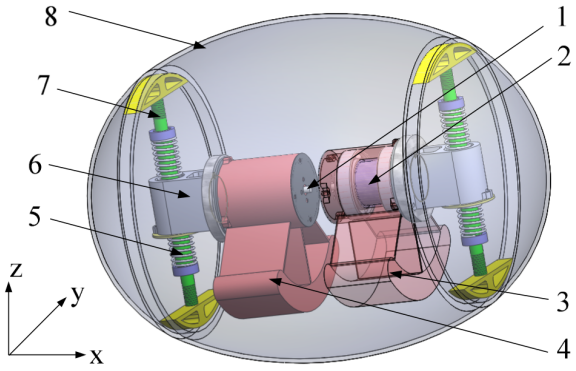

Figure 1.8: Mechanical structure of dual pendulum robot designed by Zhao: (1) Motor A; (2) Motor B; (3) Ballast B; (4) Ballast A; (5) Spring; (6) Linear Bearing; (7) Guide; (8) Outer Shell [16, 17].

to turn in place by usage of the "Stick-Slip" principle. In the first stage (stick), each pendulum is rotated up to a horizontal position slowly, but in opposite directions. This will cause a shift in the equilibrium and the robot will want to turn, but because the

pendulums are rotated up slowly, the shift in equilibrium is not large enough to overcome the static friction force holding the robot in place. In the next stage (slip), the pendulums are quickly forced down to their original vertical orientation. This also causes a shift in equilibrium, but the rapid movement is enough to overcome the static friction force causing the robot to slip and turn in place. Another type of dual pendulum design is seen in Kisbot II. Its predecessor, Kisbot I, was based on a single pendulum design and had adaptive legs allowing it to climb stairs (discussed below). Kisbot II overcomes the need for utilization of the stick-slip principle by allowing the internal mechanics to rotate about an axis perpendicular to the axis of pendulum movement [18]. The axes of rotation of Kisbot II are pictured below. The side view of Kisbot II is shown in Figure 1.9(a),

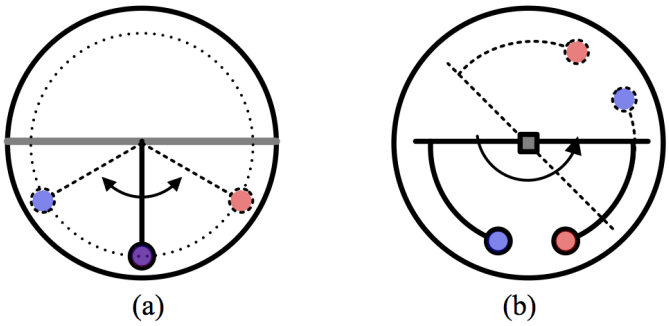

Figure 1.9: Axes of rotation of pendulums for Kisbot II. (**a**) Side view (**b**) Front view [18].

and the front view is shown in Figure 1.9(b). The side view illustrates the ability of the pendulums to rotate independently of each other in either direction about the diameter of the robot. Theoretically, the stick-slip principle described by B. Zhao could also be used to turn the robot in place. However, by adding the extra degree of freedom shown in Figure 1.9(b), the pendulums can rotate Kisbot II from left to right as well as from front to back, eliminating the need for the stick-slip principle. Some teams have devised another method altogether for barycenter offset designs. By placing the bulk of materials in the center of robot, the energy required to spin the sphere is reduced. Shafts connect the center mass to the outer shell and weights are designed to traverse these shafts as shown in Figure 1.10. By moving the weights up and down the shaft, the center of mass

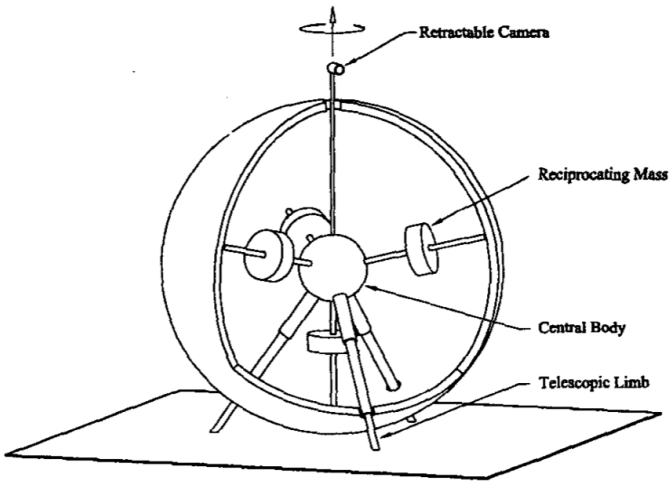

Figure 1.10: Picture of Spherobot and its system of shifting masses [19].

is changed and the ball begins to roll [19]. A few main differences separate this shifting mass design from the pendulum design. First, this design is holonomic. Regardless of its orientation, it can move in any direction. However, the controls are more complicated because the main processor must keep real time orientation data as well as distance data of all masses. Another downside to this design is that the internal weights traverse their respective shafts slowly, resulting in a slow moving robot. It also may have a hard time rolling downhill freely depending on state of the masses.

Notable Enhancements

Novel add-ons to spherical robots are as diverse as the methods used to drive them. Designs incorporate sensors, telescopic cameras, reconfigurable legs, and even jumping mechanisms. Some designs even have the ability to transform completely. N. Chadill presents a reconfigurable robot that can transform from a sphere into a dual hemisphere platform with three legs and omnidirentional wheels [20] (Figure 1.11). The ideology behind the vehicle is that it can compact itself into a sphere for transportation and deployment but will function as a leg-wheeled robot after reconfiguration. The once spherical robot can then navigate pathways autonomously as any other wheeled vehicle can. Currently, the design does not actively roll when in its spherical configuration, but this idea can be applied to current spherical robot designs. Another reconfigurable

Figure 1.11: Image of spherical robot after reconfiguration [21].

spherical robot with deployable legs is Kisbot I, the predecessor to Kisbot II, which is mentioned in Section 2.2.5. Kisbot I has two types of drive modes: a pendulum-driven mode and wheel-driven mode [22]. While the legs are retracted to the interior of the robot, the robot can maneuver as a pendulum model. In its wheeled mode, the legs extend, stabilizing the robot, and it can be driven like a wheeled vehicle. The legs can also be deployed for stopping and climbing, seen in Figure 1.12. Each leg resides in an independent hemisphere that can rotate independently of the other semi-sphere. Because the hemispheres are independent, the legs may not necessarily need to be deployed on the same Cartesian plane. This allows for the possibility of the robot to stabilize itself in unusual terrains. Another way to allow a spherical robot to climb large obstacles would be to give it the ability to jump. In a paper presented by L. Bing, a spherical robot driven by dual pendulums is retrofitted with a mechanism that gives it the ability to jump [23]. The jumping mechanism on the robot allows it to jump at a desired angle and direction once it has reconfigured itself to do so as shown in Figure 1.13. This is an extremely useful characteristic for robots of this nature because of their inability to climb steep slopes. In order to jump, the robot stores energy in a spring by extending it with a large mass attached to it. When the spring is released, the mass is accelerated upwards and collides with the top of the robot. Due to the laws of conservation of momentum,

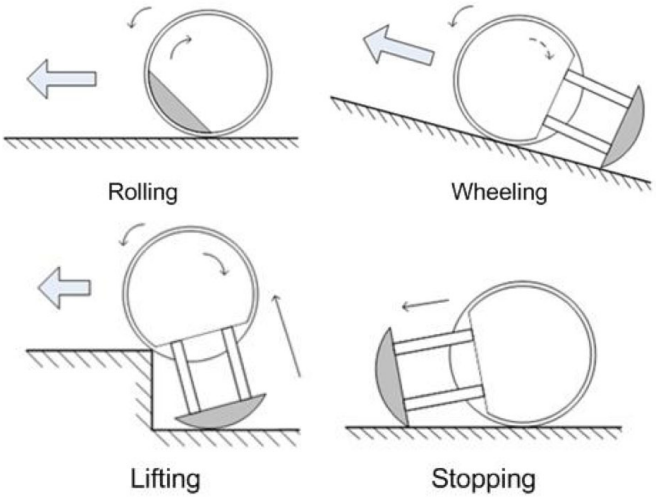

Figure 1.12: Movement types of Kisbot I [22].

the entire robot continues upwards with the mass.

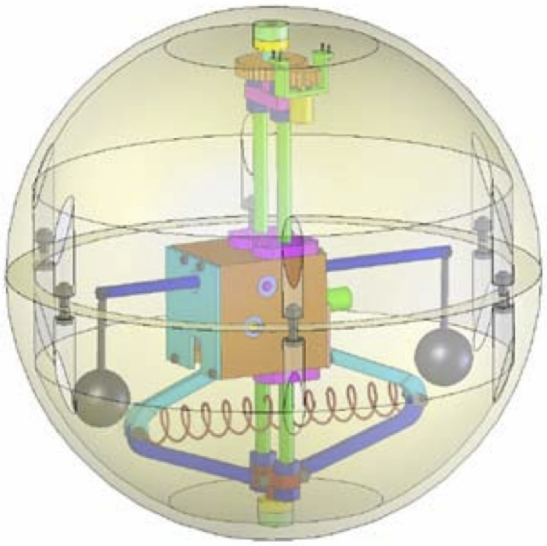

Figure 1.13: Image of hopping robot and its jumping mechanism [23].

1.3 Shell Transformation

Although not as common as barycenter offset designs, shell transformation is also a novel method of propelling a spherical robot. This idea is fairly new and has some interesting concepts associated with it. Instead of a complicated internal mechatronics system to propel the sphere, the robot relies on transformation of its outer body. This can be achieved by deformation of the encompassing shell, or having environmental elements,

such as wind or water, act on the body itself. Depending on the design, this family of robots may prove to be more versatile than a barycenter offset type of system. However, this concept is still in its infancy compared with the designs discussed above and it has potential for future research. Hence, the ideas are novel and deserve further investigations.

1.3 Implementations of Governing Principle

Pressurized Air Bladders

A basic deformable spherical rover is proposed by M. Artusi [24]. The outer shell consists of four dielectric elastomer actuators sections, which can be transformed by applying an electric field. Transformation of the sections in sequence will cause the robot to roll. K. Wait proposes a similar, yet more advanced idea that utilizes pressurized air bladders. The robot is extremely similar to a soccer ball where each pentagonal section of the outer sphere can inflate and deflate [25]. Each section of the outer sphere is actually an elastomer bladder that can be filled with air. Depending on which sections are filled with air, the sphere can be pushed along a path as shown in Figure 1.14. Ingeniously, this type of system can provide holonomic movements. Multiple bladders can be inflated allowing for a various directions of travel. A notable outcome resulting from this research

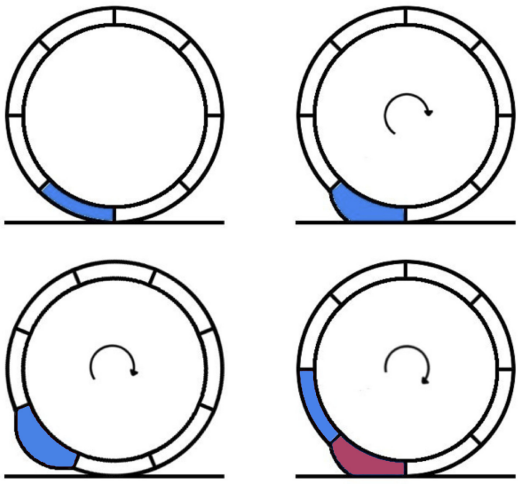

Figure 1.14: Soccer ball type robot movement [25].

is the design of the control method, which is for the most part non-computational when

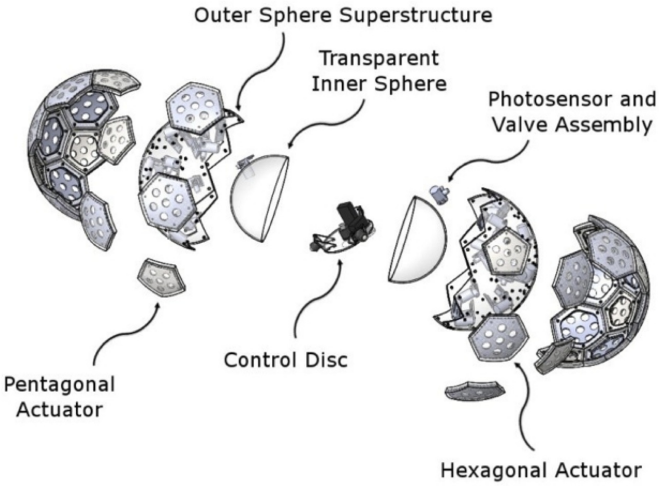

Figure 1.15: Breakaway view of the soccer ball robot [25].

compared with the previously discussed designs. Inside of the soccer ball shell there is another spherical robot altogether, designed extremely similar to the hamster ball and IDU design discussed in Section 2. On the rear of the control disc, which is inside the inner shell (shown in Figure 1.15, there is a high power LED. Each of the pentagonal bladders is equipped with a photo diode. As the control disc moves via radio control, the LED shines on the photo diodes of the bladders, inflating the proper bladders and thus moving the robot.

Shape Memory Alloys

Others have even proposed deforming the outer shell in such a way that will allow the robot to jump. T. Yamanaka proposes such a robot with "Super-ball-like" properties [26]. Superballs have a unique way of bouncing due to their spin and elastic properties. By manipulating the outer shell and placing a rotor in the internal structure, the robot should be able to have controlled hops. Sugiyama proposes and demonstrates locomotion entirely by manipulation of the outer shell [27]. The robot is comprised of shape memory alloy (SMA) coils that can be extended/retracted when voltage is applied to them. This allows the robot to flatten like a pancake and spring back to its original form in an instant, causing it to jump. When controlled properly, it can also be used for smooth locomotion

as shown in Figure 1.16.

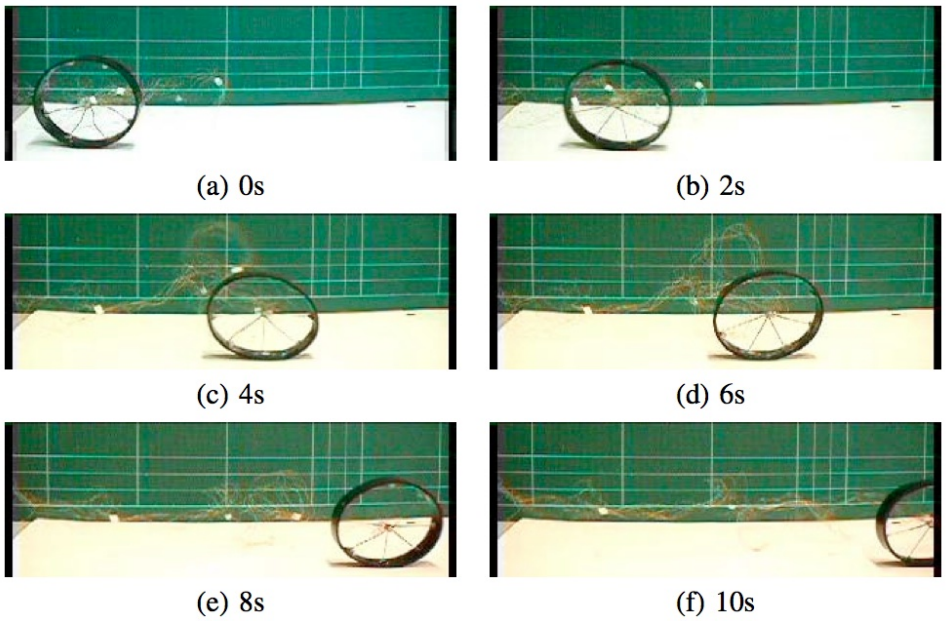

Figure 1.16: Locomotion by deformation of SMA coils [27].

1.4 Conservation of Angular Momentum

Barycenter offset designs are by far the most widely used design due to their lack of complication and ease of control, with shell transformation the next most frequent design. Although barycenter offset designs are commonly implemented, a major limitation is that because the center of mass can never go outside of the sphere, it becomes a torque-limited system. In the last 20 years, the concept of adding control moment gyroscopes (CMGs) to a spherical robot has started to be investigated by various research groups. By spinning a large flywheel rapidly and rotating it about an axis, the laws of conservation of angular momentum can be used to control the movement of the sphere. Using this method relates the output torque of the internal mechanism to the angular velocity of the CMGs. As the angular velocity of the CMGs increase, so does the output torque. This is the most recent method in obtaining an output torque greater than that can be produced by a barycenter offset type system. To date, there have been multiple designs incorporating flywheels, each with varying successes and failures. A unique feature of using a CMG is that these systems have reaction forces in all three spatial dimensions. If a CMG is

spinning about the X-axis, and is rotated about the Y-axis, then there will be a torque about the Z-axis (precession). This feature has an obvious useful potential (generating a torque in the intended direction) but also causes control issues. Depending on the design of the robot, the precession torque can be utilized to control or augment the robot's angular momentum. However, if the design does not take this extra dimension of torque into account, it may steer the robot in an unwanted direction. Therefore, although a gyro-based or gyro-augmented spherical robot may be able to outpower—in terms of torque—a barycenter offset robot, there are other design challenges that must be faced before that can occur.

1.4 Implementations

Balancing

An early approach was Gyrover, a disc-like object that balanced on its edge [28, 29]. An internal gyroscope was used to balance the robot, and the effects from the precession torque were used to steer it. Although novel in its design, it may be impractical for commercial usage. The literature states that it can be used at high speeds and on rough terrain. It can also turn in place, which can provide some degrees of holonomy. On the other hand, the robot may have difficulty correcting its orientation if it were to fall on its side. Furthermore, it may be difficult to make precision movements of the robot unless the embedded electronics and mechanics are extremely well designed.

Uni-Dimensional COAM

A UNI-Dimensional COAM design of this type is presented by Shu [30]. In this design, a variable speed rotor is used for a bob. However, this particular design utilizes the CMG bob in a different manner than a standard pendulum-type drive system does. The acceleration from spinning the CMG faster or slower will cause the shell to turn. Furthermore, if the CMG is already spinning at a high rate, maneuvering it up and down as if it were a bob will cause a precession torque that may achieve higher torques than a normal pendulum-based design (see Figure 1.18). This robot utilizes COAM in a one-dimensional manner, but has the ability to reorientate that dimension in order to control

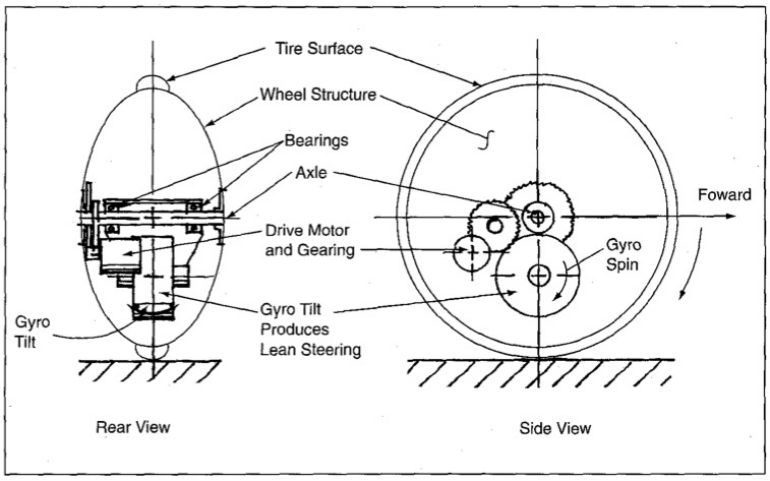

Figure 1.17: Mechanical breakdown of Gyrover [28, 29].

its movement. V. Joshi presents a robot that is controlled by two pairs of diametrically

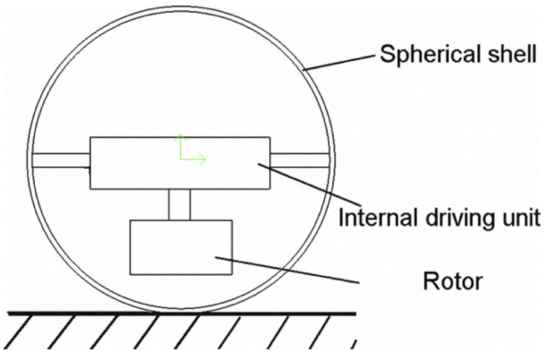

Figure 1.18: Schematic of rotor-based bob presented by S. Guanghui [30].

opposed CMGs as shown in Figure 1.19 [31, 32]. A single motor controller controls each CMG pair. As a pair's angular velocity increases, the shell will rotate in the opposite direction in order to maintain the system's total angular momentum. Having a second pair inside the ball means the ball's movement has a second degree of freedom and can move in a true holonomic manner. The state space calculations for this type of robot are much more complicated than a simple barycenter offset design, but true holonomy can be achieved. This is categorized as a Uni-Directional COAM robot because it has two systems that utilize the laws of COAM, but each system only involves one spatial plane in its COAM dynamics.

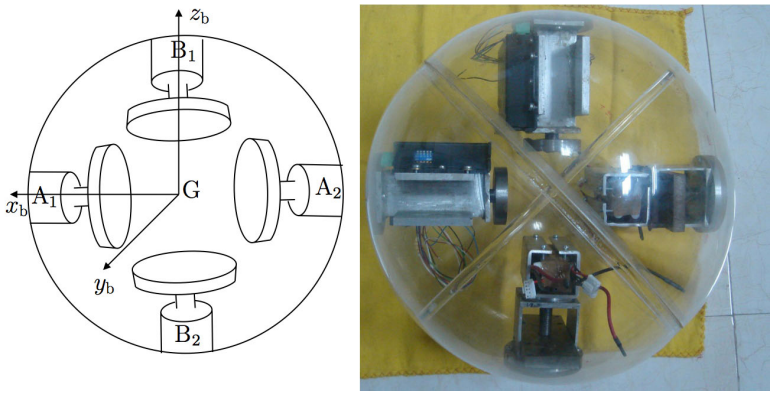

Figure 1.19: V. Joshi's diametrically opposed rotor pair design [31, 32].

Tri-Dimensional COAM

The fifth robot in the BHQ series, BHQ-5, uses a pendulum type of drive system with a control moment gyroscope to augment the stability of the robot as shown in Figure 1.20 [33]. With the CMG placed where the bob of the normal pendulum system would be, the robot is able to rotate itself depending on how the CMG rotates. Furthermore, depending on the orientation of the CMG and how it is moved, it can also increase the angular momentum of the robot as well, providing more torque than just a normal pendulum and bob would. Simplifying the idea for explanatory purposes, this can be thought of as a pendulum-type robot with a bob of variable mass. As with a pendulum type robot, the bob on this particular design can either steer or propel the robot, but in this case with varying levels of power. The BHQ-5 utilizes precession torque of a CMG, and it therefore incorporates all three spatial dimensions into its COAM dynamics.

Scissored-Pairs

The idea of using gyroscopes for conservation of angular momentum based spatial control has been utilized to control large space structures such as the International Space Station and to stabilize large telescopes [34]. More complex designs can even be used as inertial dampers in space. Based on the mission, four to six variable-speed control moment gyroscopes can be configured in such a system [35]. As mentioned before, use of control moment gyroscopes has an advantage and a disadvantage: an action on the gyroscope causes a reaction in two orthogonal planes of space. This means that unless

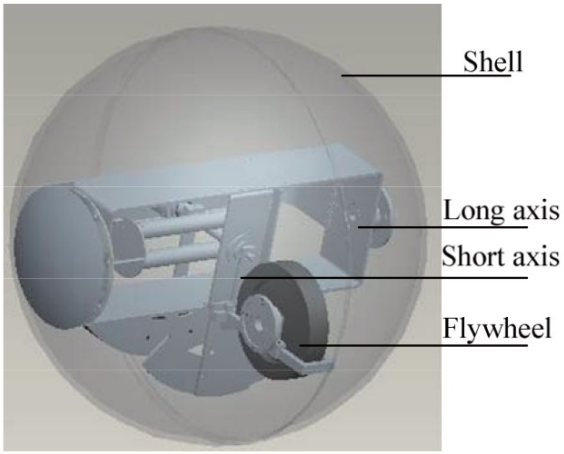

Figure 1.20: BHQ-5, a pendulum type robot with a CMG in place of a bob [33].

this is accounted for in the design, it can cause unwanted problems. One novel way to circumvent this issue is the use of a scissored-pair (Figure 1.21). By pairing each control moment gyroscope with another that is spinning in the opposite direction at the same magnitude (h_1 and h_2), the reaction from the changing spin of the gyroscopes cancel each other out and now an action on gyroscope pair (τ_1 and τ_2), causes a reaction in only one direction (h_{net}). However, one downside of this configuration is that h_{net} switches direction after θ becomes 180° or more. After that, the direction of h_{net} is pointed in the opposite direction, and goes back to the original direction when θ becomes zero. Spinning the CMGs down to zero angular velocity or spinning the CMGs in the opposite direction can neutralize this phenomenon. This configuration has recently been used in space robotics applications for low power actuators [36], and even more recently been used in augmenting spherical robot control. Usage of such a device is exhibited in G. Schroll's Master's thesis as well as patent [14, 37]. The robot can be thought of as an enhanced pendulum-type design. It incorporates a variable-speed scissored pair into its bob, allowing it to have a torque greater than $mgr * \sin(\theta)$ (shown in Figure 1.1). The output torque can be thought of as

$$\tau_{max} = mgr * \sin(\theta) + h_{net} \tag{1.2}$$

where $h_{net}$is the torque from the scissored pair, m is the mass of the bob, and r is the radius of the bob from the center of the robot. Since h_{net} is a function of the angular velocity of the CMG pair, the output torque is no longer dependent on the weight of the bob, proverbially allowing the center of mass to be shifted outside of the shell. Videos show the robot climbing out of steep holes and making sharp turns. Although the control system is still being researched, this is a viable solution to the torque limit analogous with pendulum-based designs. Although this is an innovative approach, it is only a

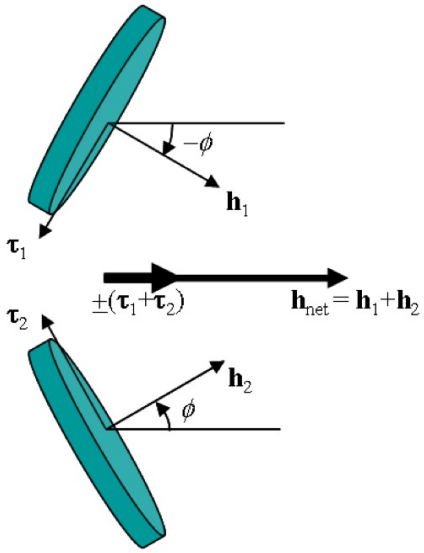

Figure 1.21: Picture of a Scissored-Pair configuration [38].

Figure 1.22: G. Schroll's spherical mobile robot internal assembly and prototype [14, 37].

momentary boost of torque and does not provide a continuous driving force. As mentioned

above, the torque boost only lasts for a rotation of 180°. After that boost, the CMGs must be reconfigured either through mechanical or control methods in order to prevent an unwanted secondary boost in the opposite direction. This presents a whole new area of research for spherical robots, as there are many possibly ways to achieve such an effect: gearing, controlling spin of the gyroscope speed, etc. A proper control method or mechanical design to change the output torque direction of a scissored pair from an oscillating to a uni-directional state may lead to a highly advanced spherical robot design.

1.5 Summary and Conclusions

Spherical robots have an abundant number of usages with an equal number of methods to control them. A brief table of taxonomy is shown in Table 1.1. Most of the types of active drive designs are based on three main principles: offset of center of gravity (barycenter offset), outer-shell deformation, or conservation of angular momentum. Compared with the other methods, the designs based on barycenter offset tend to be the least complex and can be controlled relatively easily. Generally speaking, barycenter offset designs can be analyzed with a single model (Figure 1.3). However, the power in these robots is limited because the center of gravity cannot be moved outside of the shell. Common types of barycenter offset designs include a single wheel model, car model, universal wheel model, and a pendulum model. These are the most commonplace of the designs with a large amount of research data available on them. Designs utilizing methods of conservation of angular momentum typically involve creating torque by manipulating a single axis or three axes of a CMG. Designs can either utilize the counter rotational force generated when spinning a CMG faster or slower (single-axis), or the precession torque created when rotating an already spinning CMG orthogonal to its axis of spin (triple-axis). The magnitude of torque generated in single axis designs is controlled by the amount of acceleration of the spinning CMG, whereas in triple axis designs, the precession torque is controlled by the angular velocity times the rotational acceleration. CMGs integrated into a spherical robot offer a way to solve the power constraints placed

on spherical robots by barycenter-offset designs, but this method has its own unique set of hurdles to overcome. Shell transformation designs are a rather new concept and may be more difficult to design but can be maneuvered with an almost calculation-less control method. Groups have begun merging these three concepts together producing robots that have advantages over designs based on a single concept. Marriages of multiple principles, such as a pendulum type with a CMG bob, have proved to be noteworthy concepts. Future research on gyroscope-augmented designs may lead to technology that can be integrated into a fast, agile, holonomic spherical robot.

Table 1.1: Table of Taxonomy: Type Number, Governing Principle, Source of Movement, and Dominant Power Factor.

Principle	**Method**	**Source of Movement**	**Power Factor**	**Example**
BCO	Shifting COG	COG Shift	m_{drive}/m_{shell}	R. Mukherjee et al. [19]
BCO	Single Wheel	Equilibrium Change	m_{drive}/m_{shell}	Halme et al. [1]
BCO	Universal Wheel	Downward Force on Shell	m_{drive}/m_{shell}	Zhan et al. [11]
BCO	Pendulum	Torque about Diameter	m_{bob}/m_{shell}	Michaud et al. [15]
COAM	Single-Axis	Reaction force from spin	τ_x	Guanghui et al. [30]
COAM	Triple-Axis	Precession Torque	$\tau_x \times \tau_y$	Schroll et al. [14, 37]
OST	Shell Transformation	Various	Various	Artusi, Wait, Yamanaka, Sugiyama et al. [24, 27, 25, 26]

Chapter 2: An Analytical Approach to the Development of a Spherical Robot Drive Train Based on Scissored-Pair Control Moment Gyroscopes

Chapter Abstract

The current methodology of maneuvering a spherical robot is to shift the center of mass to a set of coordinates confined by the external shell. Varying techniques of shifting the center of mass offer different characteristics of output torque. This methodology has a constraint on the location of the center of mass: it must be internal to the robot. This constraint limits the maximum amount of torque that can be designed into the system. Scissored-pair control moment gyroscopes (SP-CMGs) have recently been implemented alongside conventional drive methodologies in order to provide a momentary boost of torque to the robot. The work described herein is an investigation of the use of SP-CMGs as a sole means of propulsion for a spherical robot. By utilizing variable speed control moment gyroscopes (VSCMGs) in a SP-CMG system (SP-VSCMG), singularities that restrict other SP-CMG drive systems to momentary bursts can be mitigated, allowing for a continuous, controllable high torque output in a single direction. Furthermore, the addition of a second SP-CMG system will eliminate zero-points in the net torque equation. Analysis of the fundamental output torque equations are provided as well as theoretical and practical control theory that create a steady output torque.

2.1 Introduction

In this chapter, the design theory behind developing a SP-VSCMG system will be investigated. The fundamental limitations of creating a high torque drive train for a spherical robot will be examined, and the basic physics of CMG will be explained. The variations of how a SP-VSCMG system functions compared to a barycenter offset system will also be discussed. Furthermore, the principle equations defining the system limitations and the base for its control theory will be derived. The behavior of the output equation will be investigated by means of mathematical proofs and simulations. A series of metrics will also be developed in order to evaluate the system against other non CMG based systems. Finally, the behavior of dual SP-VSCMG system will be analyzed and a control theory will be developed.

2.2 Fundamental Problem

Developing a drivetrain for a spherical robot has many different methods of approach. The most common methods utilize the concepts of barycenter offset, outer shell transformation, or conservation of angular momentum. The dominant challenge in designing such a robot is the task of incorporating a high torque drive train into a small shell that rotates around it. Most of the technology is based off of shifting the center of gravity (barycenter offset), and since the center of gravity can never be shifted outside of the shell, the output torque is limited. Because of the limitation on output torque, the ball can passively roll to a new equilibrium. This means that there is not a motor actively driving the outer shell, and the shell spins along an axle through the center of the robot. If by some means the center of gravity could be shifted outside of the shell, the robot could be actively driven, meaning that a motor would drive the outer shell. The problem is best conceptualized by analyzing a simple conservation of angular momentum problem.

Figure 2.1 shows a system of two conical tubes, the inner solid, and the outer a simple shell. These two tubes are related in that their total angular momentum must always stay the same, and no outside forces act on the system. The engineering goal would be to

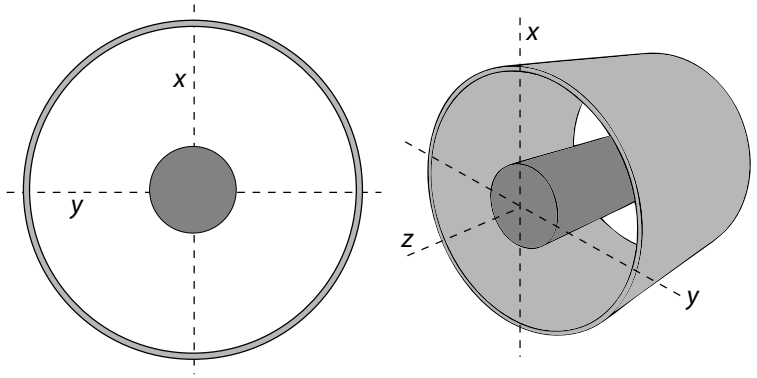

(a) (b)

Figure 2.1: Image of closed system of two concentric tubes that must obey the laws of conservation of angular momentum in 2d (a) and 3d (b)

spin the outer shell as fast as possible, with as much power as possible. This is essentially the concept of a spherical robot. In this particular example, the model is shown as a tube for clarity, but the concept can be applied to two conical spheres of similar nature. In this case, we can say that the inner tube is a motor controlled by a set of electronics and a battery, and is physically connected in some manner to the outer shell to satisfy the constraints stated above. As the inner tube spins about the z-axis, there would be a reaction spin from the outer shell in the opposite direction in order to keep the system at equilibrium. If the tube were placed in a system with no gravity or friction, floating in outer space, starts from rest, and has no outside forces acting on it, we know from the laws of conservation of angular momentum that

$$I_I\omega_I + I_O\omega_O = 0 \tag{2.1}$$

where I_I and I_O refer to the inner and outer inertias of the tubes, and ω_I and ω_O refer to the angular velocities of the tubes. Solving for ω_O, we get

$$\omega_O = -\omega_I \frac{I_I}{I_O} \tag{2.2}$$

In order to maximize ω_O, I_I must be much greater than I_O.

This raises the question of why not just design the inner tube with as much inertia as possible and the outer tube with as little as possible? Regardless of how much inertia the inner tube has, the inner tube will have to rotate in order for the outer shell to rotate, which is shown in the equation above. This means that there will be some power loss associated with the rotation of the inner tube, and also the system will be extremely heavy. The theoretical system would work, but the design constraints include mass of the system and power requirements.

From general physics, we know that torque, $\tau = I\alpha$, where α refers to angular acceleration, and therefore $\tau/\alpha = I$. So, if τ can be maximized and α minimized, we can therefore maximize the inertia of the system without increasing the mass to an unreasonable amount. For the case of a robot, the ideal situation would be for the internal tube to transfer all of its power to the outer shell. In order for this to happen, the inner tube must not rotate, since this will use up power to transfer to the outer shell. This can be made possible by predicting the output torque of the inner tube and applying an opposing torque from a motor that is attached to the inner tube on one side and the outer shell on the other. This will keep the total angular momentum of the system at zero, while the majority of the power is transferred to the outer shell. This is easily accomplished with a motor.

Figure 2.2 illustrates the inner tube, attached to one side of a motor and the outer shell attached to the other. The inner tube could be any type of system used to propel a spherical robot: a pendulum and bob, car, universal wheel, etc. Regardless of the system, the model shown below used to solve the problem is the same. The more inertia the inner tube has, the faster the outer shell will spin. The pendulum and bob, car, universal wheel and other systems based of barycenter offset have one thing in common: the amount of torque output from the inner tube depends on the mass of the tube. If the mass goes up, so does the torque. Unless a different type of system is developed, a high torque inner tube will result in an extremely heavy robot.

Robots utilizing the technique of conservation of angular momentum do not have this

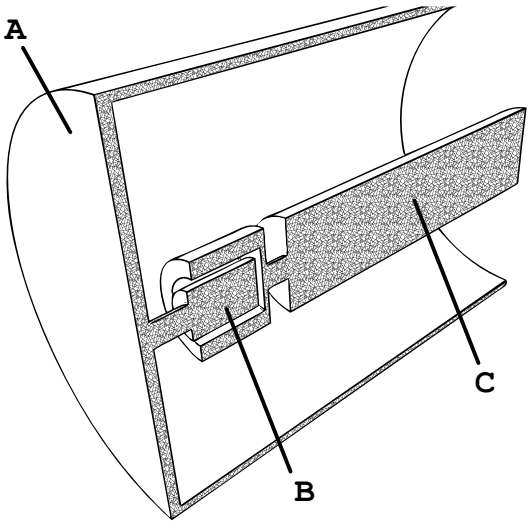

Figure 2.2: Mechanical cross section of a hypothetical tubular system showing the outer shell with low inertia (a), motor and its mechanical linkages (b), and inner tube with large inertia (c)

constraint. They are constrained by how fast the CMG is spinning. Although mass is a factor in the output torque, the magnitude can be increased by spinning the CMG faster, not just making it more massive. For this reason, gyroscopic forces are a novel consideration when developing spherical robot mechanics. However, they have their own set of trade-offs and limitations just as barycenter offset systems do.

2.3 Physics of a Control Moment Gyroscope

Depicted in figure 2.3, a control moment gyroscope (CMG) consists of a mass with inertia $I = I_x + I_y + I_z$ rotating at an angular velocity ω_x about the x-axis. While the CMG remains spinning about the x-axis, if an intermediate rotation is applied about its y-axis, it will generate a torque, τ along the z-axis due to the laws of conservation of angular momentum. Constraining the intermediate rotation to the y-axis, this can be viewed mathematically as

$$\tau_z = \dot{\theta}_y \times (I \cdot \omega_x) \tag{2.3}$$

This phenomenon can be used to create large amounts of torque in a small package due to the fact that τ_z is a factor of ω_x, the angular velocity as shown in figure 2.3. If a

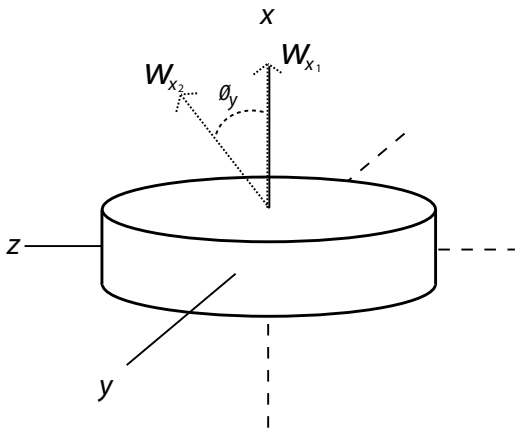

Figure 2.3: A control moment gyroscope showing its angular velocity, ω_{x_1}, the change of angular velocity as the CMG rotates about the y-axis, ω_{x_2}, and the angle the between the two velocity vectors, θ_y

system of such a nature was on a fixed position and orientation and attached to the crust of the earth, τ_z could simply be controlled by a motor, and there would be no consequent reaction forces. However, when integrated into an internal shell of spherical robot, this is not the case. If, for example, a torque in the τ_y direction was used to propel such a robot, a torque from the τ_z direction must be applied. The reaction torque associated with τ_z would spin the robot as well as the torque from τ_y causing an overly complicated control system and, more importantly, an unwanted force vector on the system.

To negate this phenomena, a scissored pair system can be utilized. The usage of scissored-pair CMGs was conceived more than a century ago and was originally thought of as a method to stabilize large vehicles [10]. Over the century, this technology has been transitioned to be used in a multitude of devices such as large structures in space [35], robotic stabilization platforms, and most recently, as an alternative to controlling robot end effectors from traditional methods such as actuators and motors [39, 40] . The mechanism consists of two CMGs of equal magnitude and opposite sign gimbal angles, each on a parallel gimbal axis [41]. As mentioned above, a single CMG produces unwanted singularities in the output torque, thereby complicating the control system, or completely nullifying the feasibility of the drive system all together. By creating a scissored-pair of

CMGs, these singularities cancel each other out, creating an output torque in a single direction. The variable direction of output torque is one of the most difficult principles to overcome in CMG array design, and a scissored-pair allows for unidirectional output torque [41].

2.4 Derivation of Key Equations

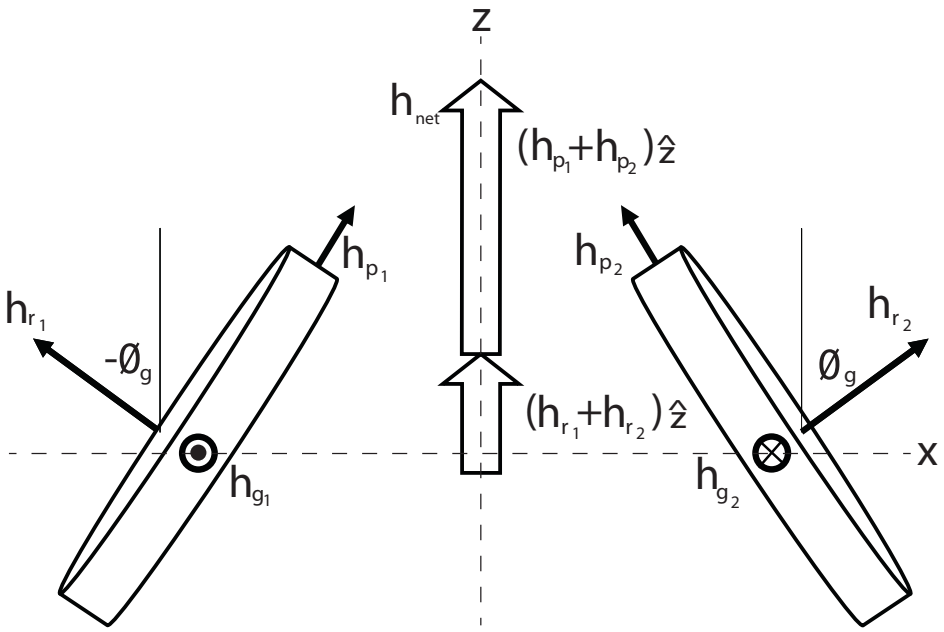

Figure 2.4: View of a scissored-pair CMG configuration showing the angular momentums (h_n) acting on closed system. Note that the projection of h_{r_1} and h_{r_2} will cancel with each other, and that h_{g_1} and h_{g_2} are equal and opposite.

Figure 2.4 depicts a scissored pair configuration of CMGs. Each CMG has its own spin momentum, h_r, its own input momentum, h_g, and each are generating a precession momentum, h_p. From rigid body dynamics [42], we know that precession torque is equal to

$$\vec{\tau_p} = \dot{\theta}_g \times h_r \tag{2.4}$$

The magnitude of which is

$$|\vec{\tau_p}| = |\vec{h_r}||\dot{\theta}_g| sin(\theta_g) \tag{2.5}$$

where θ_g is the angle between $\vec{h}_r$ and the z-axis. The torque output of the scissored pair , τ_{sp}, has been derived in previous works ([37],[14],[43],[39],[34],[44]), and its general form

is

$$\tau_{sp} = -2\dot{\theta}_g I_r \omega_r \cos\theta_g \tag{2.6}$$

where ω_r is the magnitude of angular velocity of the spin momentum of the CMG, Using electronics, we can control the gimbal rotation position and rotor spin of each CMG, θ_g and θ_r, respectively. Although τ_{sp} is derived from first principles in [39],[34], and[44], the system used in this work is based on the system designed in [37],[14], and [43]. For clarity, the scissored pair system used in this body of work will be described from first principles. Figure 2.5 shows a scissored-pair system composed of two rotors (3A and 3B) attached to two gimbals (2A and 2B) which are attached to a rod (1). In the final application, the rod will be attached to two diametrically opposed points inside of a spherical shell. Figure

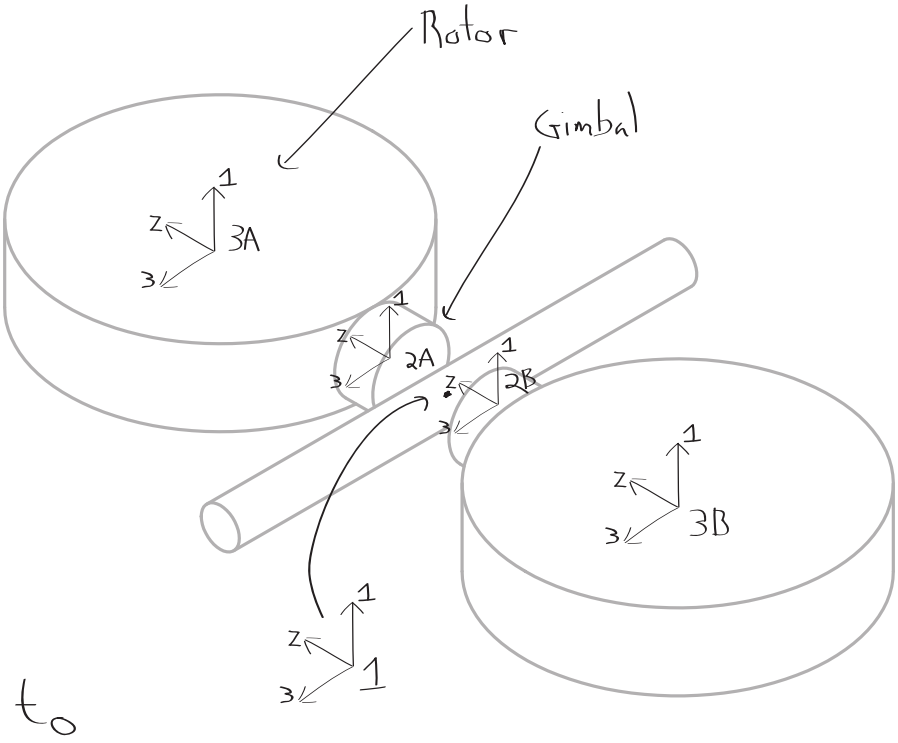

Figure 2.5: Scissored pair system showing rotors, gimbals, rod (frame 1). The coordinate systems for all bodies are shown and all $\hat{\mathbf{e}}_2$ axis are collinear

2.6 depicts the direction of the angular momentums of the scissored-pair system from an initial starting position. The angular velocities of the gimbals with respect to frame one

are equal and opposite. With respect to frame one, the angular velocities of the rotors are also equal and opposite. However, the inital starting position of rotor/gimbal 3A/2A is rotated 180 degrees about the $\hat{\mathbf{e_g}}$ axis, meaning that although the angular velocities are opposite with respect to frame 1 at the starting position, they are equal with respect to their respective rotor frame.

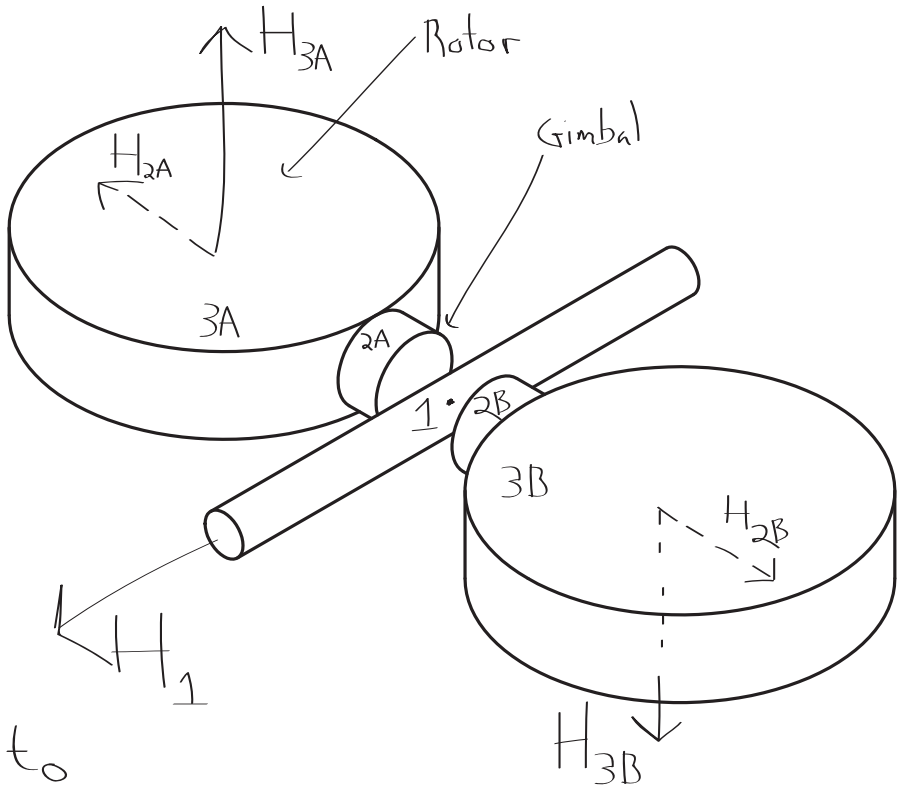

Figure 2.6: Scissored pair system shown at time zero. The direction of the angular momentums of each body are also depicted.

Figure 2.7 depicts the scissored pair system after a period of time when the gimbal rotation has had an effect. The angle between frames 2A and 1 is shown as θ_g. This is also the angle between frames 3A and 1 due to the fact that 2A and 3A rotate together about the $\hat{\mathbf{e_2}}$ axis, although the angle from nA and nB frames are equal and opposite due to the equal and opposite rotation of the gimbals.

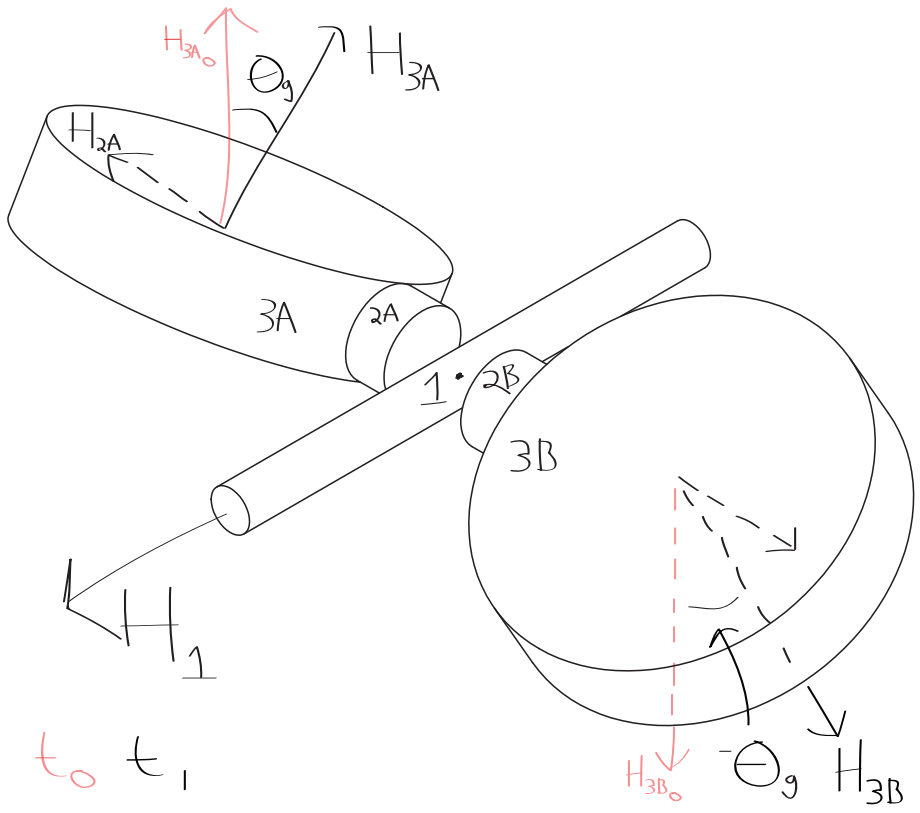

Figure 2.7: Scissored pair system shown at time 1. The direction of the angular momentums of each body are also depicted, as well as the change of the angular momentums from time 0.

In order to solve for the angular momentum on body 1, $\boldsymbol{H}_1$, we will start by using conservation of angular momentum on the system. The inertial frame is at the center of of mass of body 1. This yields the equation

$$0 = \boldsymbol{H}_0 + \boldsymbol{H}_1 + \boldsymbol{H}_{2A} + \boldsymbol{H}_{3A} + \boldsymbol{H}_{2B} + \boldsymbol{H}_{3B} \tag{2.7}$$

The angular momentum of the inertial frame, $\boldsymbol{H}_0$, is zero, so we will solve for $\boldsymbol{H}_1$ and expand individual terms.

$$-\boldsymbol{H}_1 = I^{2A/0}\boldsymbol{\omega}^{2A/0} + I^{3A/0}\boldsymbol{\omega}^{3A/0} + I^{2B/0}\boldsymbol{\omega}^{2B/0} + I^{3B/0}\boldsymbol{\omega}^{3B/0} \tag{2.8}$$

where notation $x^{Y/Z}$ is read as variable x of frame Y with respect to frame Z. The next

step is to expand the angular velocities to the sum of the individual frames.

$$\begin{aligned} -I^{1/0}\boldsymbol{\omega}^{1/0} =& I^{2A/0}(\boldsymbol{\omega}^{2A/1} + \boldsymbol{\omega}^{1/0}) + I^{3A/0}(\boldsymbol{\omega}^{3A/2A} + \boldsymbol{\omega}^{2A/1} + \boldsymbol{\omega}^{1/0}) \\ &+ I^{2B/0}(\boldsymbol{\omega}^{2B/1} + \boldsymbol{\omega}^{1/0}) + I^{3B/0}(\boldsymbol{\omega}^{3B/2B} + \boldsymbol{\omega}^{2B/1} + \boldsymbol{\omega}^{1/0}) \end{aligned} \tag{2.9}$$

Rearranging the $\boldsymbol{\omega}^{1/0}$ terms yields

$$\begin{aligned} -(I^{1/0} + I^{2A/0} + I^{3A/0} + I^{2B/0} + I^{3B/0})\boldsymbol{\omega}^{1/0} =& \\ I^{2A/0}(\boldsymbol{\omega}^{2A/1}) + I^{3A/0}(\boldsymbol{\omega}^{3A/2A} + \boldsymbol{\omega}^{2A/1}) & \\ + I^{2B/0}(\boldsymbol{\omega}^{2B/1}) + I^{3B/0}(\boldsymbol{\omega}^{3B/2B} + \boldsymbol{\omega}^{2B/1}) & \end{aligned} \tag{2.10}$$

For notation purposes, $I^{1/0} + I^{2A/0} + I^{3A/0} + I^{2B/0} + I^{3B/0} = I_T$. Substituting yields

$$\begin{aligned} -I_T\boldsymbol{\omega}^{1/0} =& I^{2A/0}(\boldsymbol{\omega}^{2A/1}) + I^{3A/0}(\boldsymbol{\omega}^{3A/2A} + \boldsymbol{\omega}^{2A/1}) \\ &+ I^{2B/0}(\boldsymbol{\omega}^{2B/1}) + I^{3B/0}(\boldsymbol{\omega}^{3B/2B} + \boldsymbol{\omega}^{2B/1}) \end{aligned} \tag{2.11}$$

As described before, a scissored-pair undergoes a sequenced of body fixed rotations. This is shown in figure 2.8. The configuration of the coordinate systems is shown before any rotations occur.

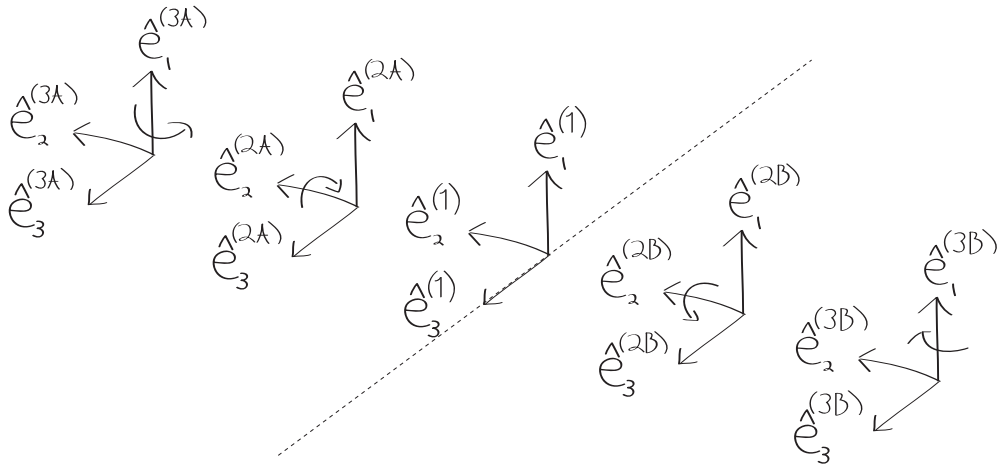

Figure 2.8: Initial configuration of coordinate system. A sequence of body-fixed rotations occurs between individual coordinate systems where body 1 refers to the rod, bodies 2A and 2B refer to the gimbals, and bodies 3A and 3B refer to the rotors.

The rotation between the frame 1 and 2A can be described as

$$\begin{Bmatrix} \hat{\mathbf{e}}_1^{(2A)} \\ \hat{\mathbf{e}}_2^{(2A)} \\ \hat{\mathbf{e}}_3^{(2A)} \end{Bmatrix} = \begin{bmatrix} \cos\theta_g & 0 & -\sin\theta_g \\ 0 & 1 & 0 \\ \sin\theta_g & 0 & \cos\theta_g \end{bmatrix} \begin{Bmatrix} \hat{\mathbf{e}}_1^{(1)} \\ \hat{\mathbf{e}}_2^{(1)} \\ \hat{\mathbf{e}}_3^{(1)} \end{Bmatrix} \tag{2.12}$$

where θ_g is the gimbal angle of rotation, which is the same magnitude for both gimbal 2A and 2B. Graphically, this is shown in figure 2.9. Similarly, the rotation between frame 1

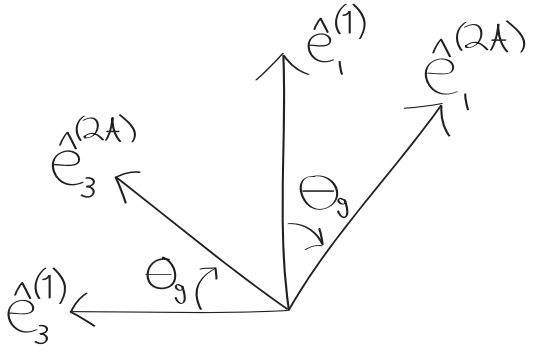

Figure 2.9: Rotation between frame 1 and frame 2B, where θ_g equals the gimbal angle of rotation, which is the same magnitude for 2A and 2B, but opposite direction

to 2B can be described as

$$\begin{Bmatrix} \hat{\mathbf{e}}_1^{(2B)} \\ \hat{\mathbf{e}}_2^{(2B)} \\ \hat{\mathbf{e}}_3^{(2B)} \end{Bmatrix} = \begin{bmatrix} \cos\theta_g & 0 & \sin\theta_g \\ 0 & 1 & 0 \\ -\sin\theta_g & 0 & \cos\theta_g \end{bmatrix} \begin{Bmatrix} \hat{\mathbf{e}}_1^{(1)} \\ \hat{\mathbf{e}}_2^{(1)} \\ \hat{\mathbf{e}}_3^{(1)} \end{Bmatrix} \tag{2.13}$$

and graphically represented in figure 2.4.

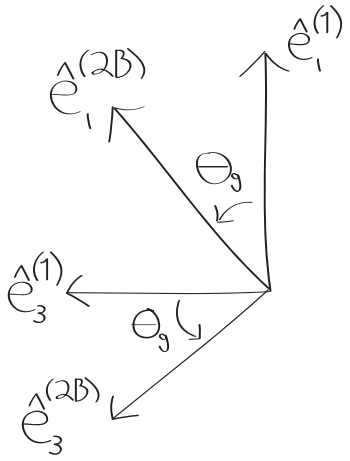

Figure 2.10: Where θ_g equals the gimbal angle of rotation, which is the same magnitude for 2A and 2B

From equations 2.12 and 2.13 it is important to note that

$$\hat{\mathbf{e}}_2^{(2A)} = \hat{\mathbf{e}}_2^{(1)} \tag{2.14a}$$

$$\hat{\mathbf{e}}_2^{(2B)} = \hat{\mathbf{e}}_2^{(1)} \tag{2.14b}$$

Therefore

$$\hat{\mathbf{e}}_2^{(2A)} = \hat{\mathbf{e}}_2^{(2B)} \tag{2.15}$$

The angular velocity of the gimbal rotation, ω_g, is equal magnitude and opposite direction

for each gimbal. This can be described as

$$\boldsymbol{\omega}^{2A/1} = \dot{\Theta}_g \hat{\mathbf{e}}_2^{(1)} = \omega_g \hat{\mathbf{e}}_2^{(1)} \tag{2.16a}$$

$$\boldsymbol{\omega}^{2B/1} = -\dot{\Theta}_g(-\hat{\mathbf{e}}_2^{(1)}) = -\dot{\Theta}_g \hat{\mathbf{e}}_2^{(1)} = -\omega_g \hat{\mathbf{e}}_2^{(1)} \tag{2.16b}$$

thus

$$\boldsymbol{\omega}^{2A/1} = -\boldsymbol{\omega}^{2B/1} \tag{2.17}$$

Substituting equation 2.17 into equation 2.11 yields

$$\begin{aligned} -I_T \boldsymbol{\omega}^{1/0} =& \cancelto{0}{I^{2A/0}(\boldsymbol{\omega}^{2A/1})} + I^{3A/0}(\boldsymbol{\omega}^{3A/2A} + \cancelto{0}{\boldsymbol{\omega}^{2A/1}}) \\ &+ \cancelto{0}{I^{2B/0}(\boldsymbol{\omega}^{2B/1})} + I^{3B/0}(\boldsymbol{\omega}^{3B/2B} + \cancelto{0}{\boldsymbol{\omega}^{2B/1}}) \end{aligned} \tag{2.11}$$

Therefore

$$-I_T \boldsymbol{\omega}^{1/0} = I^{3A/0}(\boldsymbol{\omega}^{3A/2A} + \boldsymbol{\omega}^{3B/2B}) \tag{2.18}$$

where $\boldsymbol{\omega}^{3A/2A}$ and $\boldsymbol{\omega}^{3B/2B}$ are the rotor spins with respect to their respective gimbals. In other words

$$\boldsymbol{\omega}^{3A/2A} = \omega_r \hat{\mathbf{e}}_1^{(3A)} = \omega_r \hat{\mathbf{e}}_1^{(2A)} \tag{2.19a}$$

$$\boldsymbol{\omega}^{3B/2B} = -\omega_r \hat{\mathbf{e}}_1^{(3B)} = -\omega_r \hat{\mathbf{e}}_1^{(2B)} \tag{2.19b}$$

Where ω_r is the magnitude of rotor spin angular velocity. Imposing the transformations described in equations 2.12 and 2.13 yields

$$\boldsymbol{\omega}^{3A/2A} + \boldsymbol{\omega}^{3B/2B} = \omega_r \hat{\mathbf{e}}_1^{(2A)} - \omega_r \hat{\mathbf{e}}_1^{(2B)} \tag{2.20a}$$

$$\begin{aligned} &= \omega_r(\cos\theta_g \hat{\mathbf{e}}_1^{(1)} - \sin\theta_g \hat{\mathbf{e}}_3^{(1)}) \\ &\quad -\omega_r(\cos\theta_g \hat{\mathbf{e}}_1^{(1)} + \sin\theta_g \hat{\mathbf{e}}_3^{(1)}) \end{aligned} \tag{2.20b}$$

Therefore

$$\boldsymbol{\omega}^{3A/2A} + \boldsymbol{\omega}^{3B/2B} = -2\omega_r \sin\theta_g \hat{\mathbf{e}}_3^{(1)} \tag{2.21}$$

Substituting in equation 2.21 into equation 2.18

$$-I_T \boldsymbol{\omega}^{1/0} = I^{3A/0}(-2\omega_r \sin\theta_g \hat{\mathbf{e}}_3^{(1)}) \tag{2.22}$$

or

$$I_T \boldsymbol{\omega}^{1/0} = 2I^{3A/0}\omega_r \sin\theta_g \hat{\mathbf{e}}_3^{(1)} \tag{2.23}$$

To evaluate $\frac{d}{dt}\left(I_T \boldsymbol{\omega}^{1/0}\right)$ we will take the time derivative of 2.23

$$\frac{d}{dt}\left(I_T \boldsymbol{\omega}^{1/0}\right)\Big|_0 = \frac{d}{dt}\left(2I^{3A/0}\omega_r \sin\theta_g \hat{\mathbf{e}}_3^{(1)}\right)\Big|_0 \tag{2.24}$$

which yields

$$\begin{aligned} I_T \boldsymbol{\alpha}^{1/0} =& 2I^{3A/0}\alpha_r \sin\theta_g \hat{\mathbf{e}}_3^{(1)} + 2I^{3A/0}\omega_r\omega_g \cos\theta_g \hat{\mathbf{e}}_3^{(1)} \\ &+ 2I^{3A/0}\omega_r \sin\theta_g \boldsymbol{\omega}^{1/0} \times \hat{\mathbf{e}}_3^{(1)} \end{aligned} \tag{2.25}$$

In matrix form, this yields

$$I_T \boldsymbol{\alpha}^{1/0} = \left\{ \begin{array}{c} 2I^{3A/0}\omega_r\Omega_2 \sin\theta_g \\ -2I^{3A/0}\omega_r\Omega_1 \sin\theta_g \\ 2I^{3A/0}\alpha_r \sin\theta_g + 2I^{3A/0}\omega_r\omega_g \cos\theta_g \end{array} \right\} \tag{2.26}$$

where

$$\omega^{1/0} = \Omega_1 \hat{\mathbf{e}}_1^{(1)} + \Omega_2 \hat{\mathbf{e}}_2^{(1)} + \Omega_3 \hat{\mathbf{e}}_3^{(1)} \tag{2.27}$$

is the angular velocity of the rod with respect to the inertial frame. Ω_n is the magnitude of the velocity in the n direction. Next, we will look at two special cases of equation 2.26. The first special case is when Ω_1 and Ω_2 are equal to zero, which means that body 1 is

only rotating about the $\hat{\mathbf{e}}_3^{(1)}$ axis. This will yield

$$I_T \boldsymbol{\alpha}^{1/0} = \left\{ \begin{array}{c} 0 \\ 0 \\ 2I^{3A/0}\alpha_r \sin\theta_g + 2I^{3A/0}\omega_r\omega_g \cos\theta_g \end{array} \right\} \tag{2.28}$$

By examination of the equation 2.28 we can see that the only output torque of the system will be along the $\hat{\mathbf{e}}_3^{(1)}$ axis. The second special case we will examine will be when the acceleration of the rotor is zero. This will yield

$$I_T \boldsymbol{\alpha}^{1/0} = \left\{ \begin{array}{c} 0 \\ 0 \\ 2I^{3A/0}\omega_r\omega_g \cos\theta_g \end{array} \right\} \tag{2.29}$$

In a realistic environment, a scissored-pair's torque can be described as shown in equation 2.26, which will be difficult to control when combined with a control system. However, it will be helpful to understand the scissored-pair in an ideal state, when rotor speed is constant and Ω_1 and Ω_2 are equal to zero. Furthermore, equation 2.29 is the same as equation 2.6, the torque equation cited in the other publications, thus further solidifying the equation set presented in this section is correct.

2.5 Torque in Ideal Conditions

The scissored pair system shown in figure 2.4 shows the angular momentums acting on the system. h_r is the angular momentum associated with the spin of the CMG, h_g is the angular momentum of the gimbal CMG which is controlled by the user, and h_p is the generated angular momentum due to precession. We can assume that h_g is controlled by a single or set of motors and is ideal. In a scissored pair configuration, the angular momentum vectors of h_g are equal and opposite, and therefore cancel each other out. In this instance h_{g_1} is directed out of the paper, and h_{g_2} is directed into the paper. Furthermore, because each CMG is mirrored about the z axis, the projection of each h_{r_n}

angular momentum along the x axis cancels with its mirrored counterpart as long as they are of equal magnitude. Further assuming that the rotors maintain constant speeds, and that there are no torques in the $\hat{\mathbf{e}}_2^{(1)}$ and $\hat{\mathbf{e}}_3^{(1)}$, the resultant output torque of the system can be described as

$$\tau_{sp} = 2I_R\omega_g\omega_r cos\theta_g \tag{2.30}$$

where I_R is the inertia dyadic of the rotor with respect to the inertial frame. In this specific case it is $I^{3A/0}$. Equation 2.30 is the same as equation 2.6, the equation derived in previous literature, and its general form can be looked at as

$$\tau_{sp} = A\cos\theta_g \tag{2.31}$$

where A is dependent on design parameters such as inertia and maximum angular velocity of the rotors. In terms of mathematical equations $A = 2I_R\omega_g\omega_r$. The scissored-pair introduces a constraint such that the uni-directional output torque is only advantageous within a certain envelope of maneuver: after 180 degrees of rotation, the torque reverses direction. If using a scissored-pair as a means to manipulate an end effector, the CMG controlled linkage could only rotate 180 degrees before it reverses direction. The goal of this research is to manipulate the magnitude of the gimbal and rotor torques so that the scissored pair may provide a continuous output torque.

Equation 2.31 is sinusoidal in nature. If A was a constant value, and θ_g had no limit of rotation, meaning that the scissored pair continues to spin forever and has no mechanical stopping point where it has to be reversed, the output torque would switch between positive and negative. A possible solution to this would be to have a geared system that could switch mechanical connections when one needs to produce an all positive (or negative) output. Another solution would be to attempt to manipulate parameters in A through design and control methods.

Figure 2.11 is a normalized graphical representation of the general output form of equation 2.31, where A is equal to one. Parameter A is set to one in this example in order

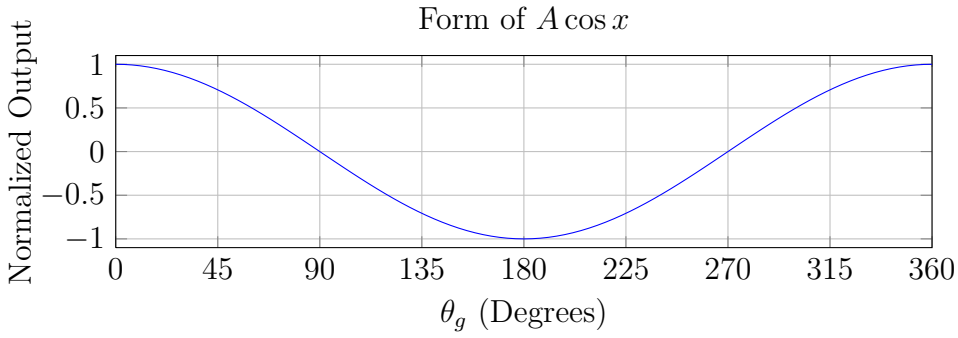

Figure 2.11: Plot showing the sinusoidal nature of the torque output of a scissored pair

to visualize the periodic nature of the function and examine its behavior. In practice, A will be changing dependent upon the design of the control system. The x-axis ranges from 0 to 2π, representing a full rotation of the scissored-pair system. The y-axis depicts the output torque of the pair where accelerations and velocities are constant during the system's rotation. By visual inspection, there are points in which the system switches polarity in its magnitude. In practice, the positive or negative magnitude moves the robot forward or backward. It would be ideal for this output function to have either a continuous positive or negative magnitude so that a robot can be rolled in one direction continuously. For the duration of this paper, we will be addressing the issue of creating a purely positive output.

2.6 Changing Torque in Ideal Conditions

The first important piece of information is to determine when τ_{net} switches polarity. From 2.31 we know that τ_{net} will switch polarity when

$$\theta_g = \frac{\pi}{2}, \frac{3\pi}{2} \tag{2.32}$$

When the output torque switches polarity, a component of A must be manipulated so that output polarity stays positive. From 2.30 we can see that the possible options are changing ω_r or ω_g. Knowing this information, there are three possible ways to change the variables in the specific output form: 1) change the magnitude of ω_g or ω_r to zero, 2) change the sign of the magnitude of ω_g or 3) change the sign of the magnitude of ω_r.

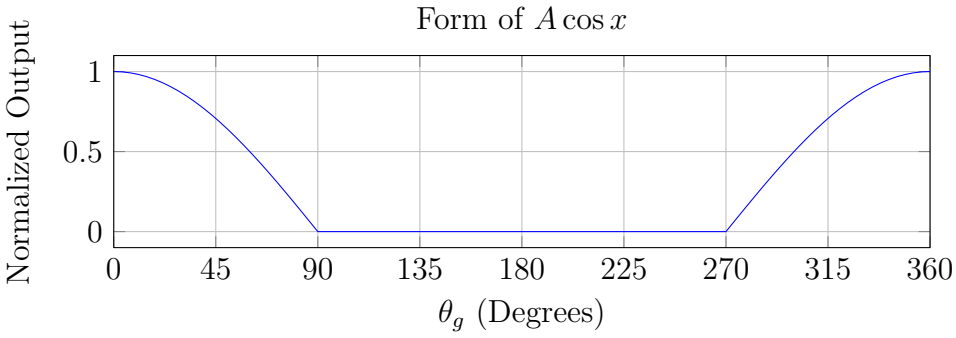

Figure 2.12: View of the output torque of a scissored pair when ω_S is set to zero if output torque is below zero

Option 1 involves changing either ω_g or ω_r to zero, and τ_{sp} is shown in figure 2.12. Changing the gimbal angular velocity to the system, ω_g, to zero would mean that the system stops rotating, but the rotors are active and gyroscopic effects will take place if outside forces act on the system. Changing the rotor angular velocity, ω_r to zero means that there will be no gyroscopic effect, but the CMGs will still rotate about the gimbal axis. If there is no gyroscopic effect, then the system can be reorientated to its initial state with minimal effect on the output torque. Once the system is reconfigured, ω_r can change to a nonzero number, recreating gyroscopic effect, and then the process repeats. Figure 2.12 is a view of what the output torque would look like if ω_r was decreased to zero during periods when the output is in the negative.

It is important to note that the x-axis of this graph is θ, a unit of space, not time. During the phase where the output torque is zero, the system may be reset to the next phase quickly, resulting in a time domain graph where the peaks are much closer together. In other words, the positive region of the graph last much longer than the zero portion.

Option 2 involves reversing the polarity of the A term by reversing the gimbal speed. When the gimbal speed is reversed, θ_g also changes direction. This means that as θ_g approaches $\pi/2$ from 0, if ω_g changes direction, so does θ_g. Therefore, θ_g will oscillate between $3\pi/2$ and $\pi/2$. This means that ω_r would also need to switch polarity in order for the equation to become positive.

Option 3 would be to switch the magnitude of ω_r when θ_g equals $\pi/2$ or $3\pi/2$. This

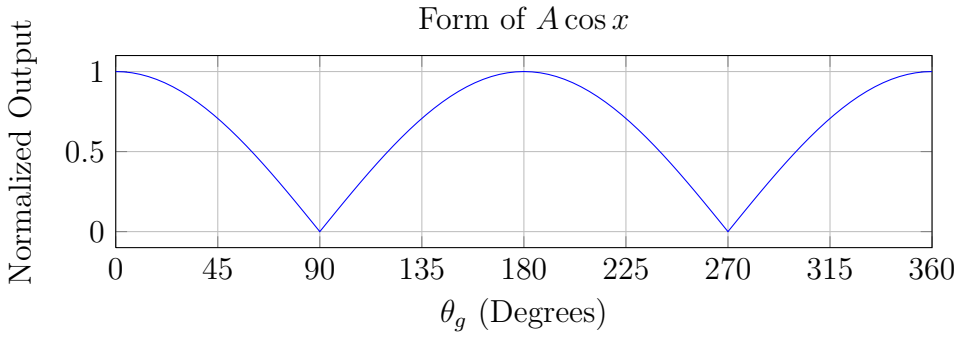

Figure 2.13: View of the output torque of a scissored pair when ω_S is set to $-\omega_S$ if output torque is below zero

would result in a torque output function that is mathematically similar to

$$|\vec{\tau}_{sp}| = abs(2I_r\omega_g\omega_r \sin\theta_g) \tag{2.33}$$

which is graphically shown in figure 2.14

The graph represents an instantaneous switch of $\omega_{r_{max}}$ to $-\omega_{r_{max}}$ at $\pi/2$ and $3\pi/2$. In practice, an instantaneous polarity change of this type would result in high current spikes and extreme torques that the motors may not be able to handle. In the final design, a switch in polarity of this nature will require time for the CMG to accelerate and decelerate.

All three options discussed are possible solutions to making an all positive output torque. However, stopping the rotation of the CMGs and reconfiguring their position will result in large times where τ_{sp} is zero. As mentioned previously, the goal of this research is to create a continuous, non-zero, positive output torque. The first option will create an all positive output, but will not be constant due to the time it would take to reconfigure the system. The second option has the ability to be continuous, and this is what the research will focus on. It is important to note, however, that it may not be necessary for the scissored pair to have a constant output, such as in matters of coasting. So although option one may not provide the most power, it still may be useful in the design.

This concept can be visualized in figures 2.14 and 2.15. The blue lines represent the

potential output torque of the system, and the black dotted lines represent the normalized plot of the angular velocity of the VSCMGs. Figure 2.14 depicts a control system where the angular velocity of the VSCMG is halted while the system reorientates, and then the VSCMG is speed up in the same direction. Figure 2.15 depicts a control system where the angular velocity of the VSCMG is spun in the opposite direction instead of re-orientating the system. As previously indicated, there is no down time associated with this control system since the system does not need to reconfigure itself.

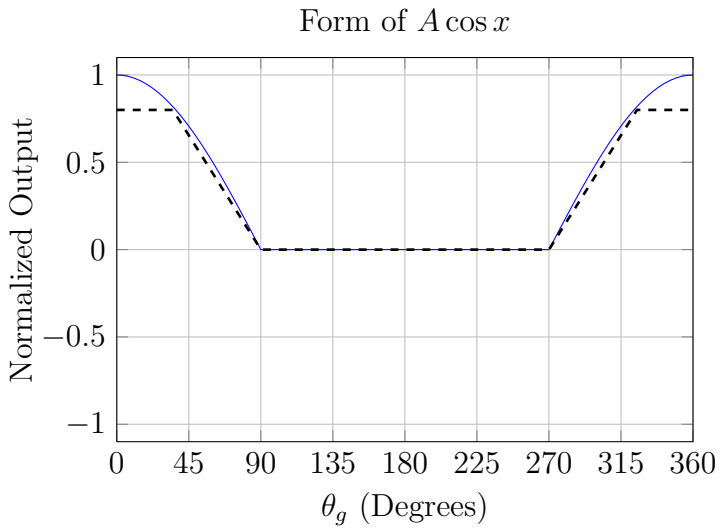

Figure 2.14: Control option 1, where the scissored-pair is reconfigured when output torque becomes negative. The time for reconfiguring the system may be extremely short, depending on the hardware.

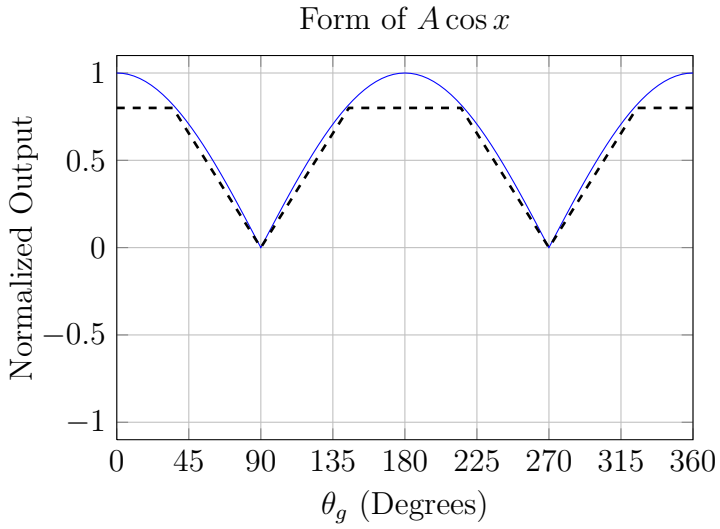

Figure 2.15: Control option 2, where the scissored-pair continues to rotate and ω_r is reversed when the output torque is below zero. Since the system does not need to be reconfigured as in option 1, there is little to no system down time.

2.7 Controls in Ideal Conditions

To define a global, governing control equation for such a complicated system is an overly daunting task. Below is the view of the output torque equation in terms of derivatives of θ_g.

$$\tau_{sp}(\theta_g) = 2I_r\omega_r\dot{\theta}_g\cos\theta_g \tag{2.34}$$

The output function is dependent on θ_g, but also on its first derivitive, which makes forming a general solution an overly complex problem. Therefore, the approach that will be to examine the controls at a steady system state and then develop a control logic based on the steady state conditions. Through inspection and simulation, two steady states were selected, Δ and Γ. The Δ steady state consists of switching the magnitude of ω_r when the output torque changes from positive. The Γ steady state consists of switching the magnitude of ω_g when the output torque becomes negative. Each state has unique properties which are discussed in the next sections. It is important to note that the Δ and Γ oscillations are steady state and do not involve transient start up issues. To begin the discussion, we will look at both the Δ and Γ steady states in ideal conditions before examining them in non-ideal conditions.

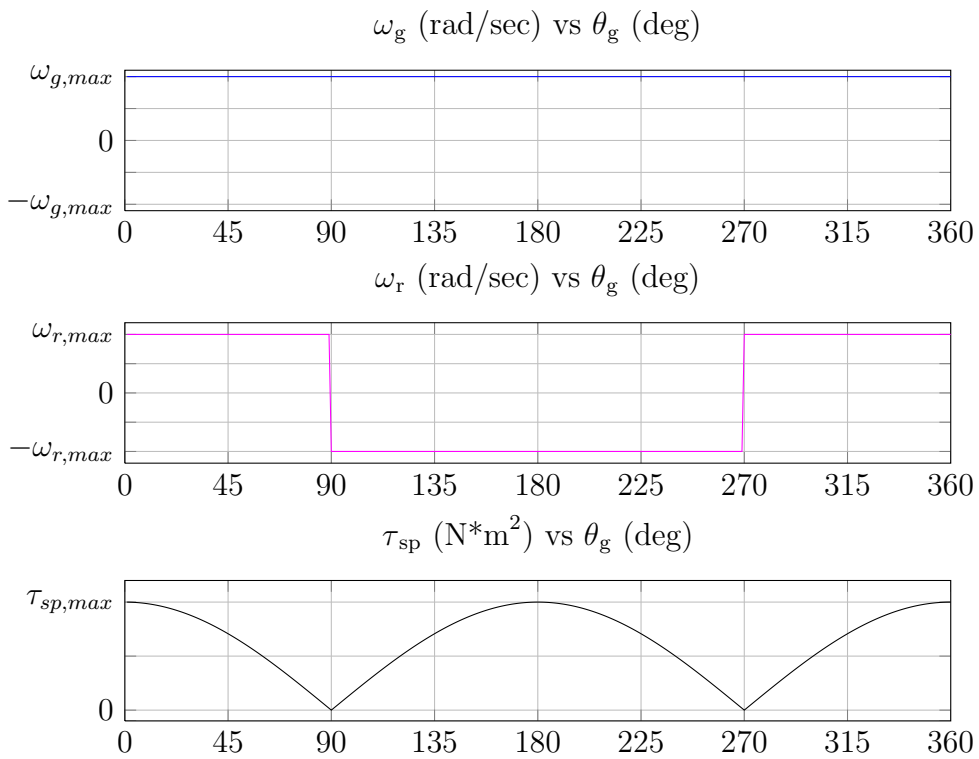

Figure 2.16: Control signals ω_g and ω_r and the corresponding output torque, τ_{sp} shown in a spacial domain in the Δ steady state.

The Delta (Δ) state of oscillation has an output form that appears like a rectified cosine function as shown in figure 2.16. This oscillation state is achieved by changing the polarity of ω_r when the torque becomes negative. θ_g oscillates from 0 to 2π, meaning that the system can spin continuously without having to reverse direction. Furthermore, the angular flywheel velocity, ω_r switches magnitude polarity twice per period.

The Gamma (Γ) state of oscillation has an output form that resembles a rectified sine function as shown in figure 2.17. This state is achieved by switching polarity of ω_g when the output torque becomes negative. The angular gimbal velocity, ω_g, switches polarity twice per period.

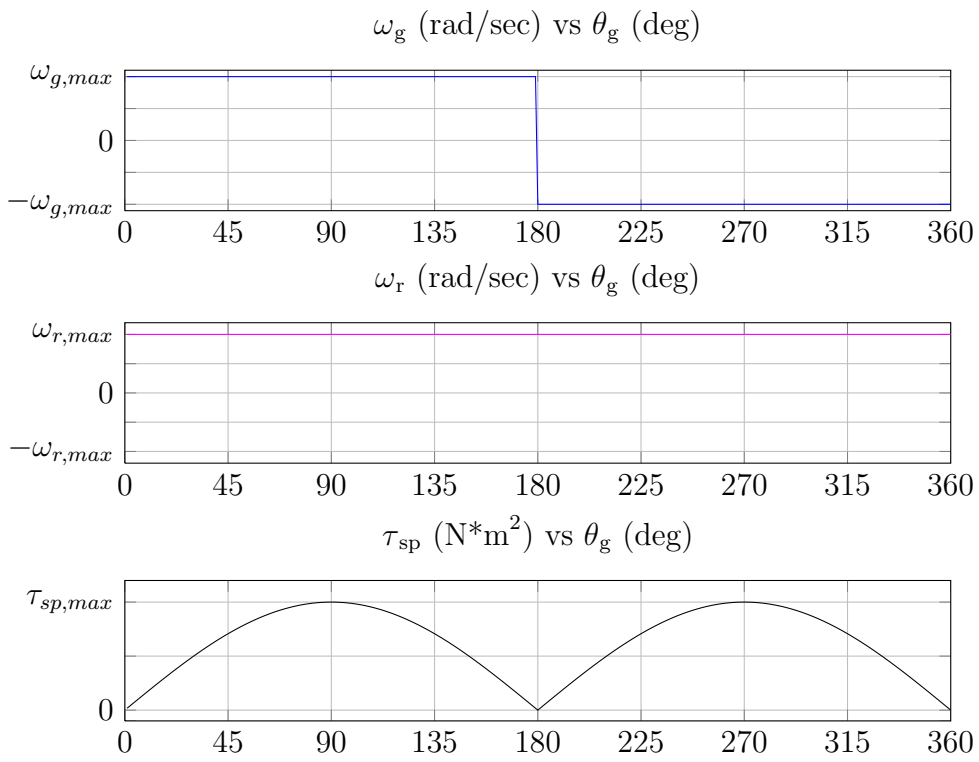

Figure 2.17: Control signals ω_g and ω_r and the corresponding output torque, τ_{sp} shown in a spacial domain in the Γ steady state.

However, the Γ oscillation state of figure 2.17 is not easily achievable in a time domain. For example, as θ_g goes from 0 and reaches 180 degrees, ω_g needs to change orientation to keep the output torque positive. However, the x-axis, θ_g is dependent upon ω_g. Thus, if ω_g becomes negative, θ_g will travel in the reverse direction. Unfortunately any value of θ_g that is less than 180 degrees requires a positive value of ω_g. In short, the system would become stuck when θ_g reaches 180 degrees, and ω_r would have to switched as well. Due to the fact that Γ oscillation state requires switching of both ω_r and ω_g, this work will focus on the simpler control method of the Δ steady state which requires only switching the polarity of ω_r.

2.8 Peak Torque in Ideal Conditions

When designing such a system, it is helpful to know the possible maximum output torque in order to have a basis to compare an individual design to. This can be done by taking the derivative of the ideal torque function, equation 2.29, solving for zero, and

substituting that answer back into the original equation. Since the goal is to determine the peak maximum of the function, the maximum value of ω_r and ω_g will be used. These parameters are selected during the design phase and are characteristics of the motor assemblies. The derivation of $\tau_{sp,max}$ is shown below.

$$\tau_{sp} = 2I_r\omega_r\omega_g \cos\theta_g \tag{2.35a}$$

$$\frac{d}{d\theta}(\tau_{sp}) = \frac{d}{d\theta}(2I_r\omega_r\omega_g \cos\theta_g) \tag{2.35b}$$

$$0 = -2I_r\omega_r\omega_g \sin\theta_g \tag{2.35c}$$

$$0, \pi = \theta_g \tag{2.35d}$$

Substituting equation 2.35d into equation 2.29 yields

$$\tau_{sp,max} = 2I_r\omega_r\omega_g \cos 0 \tag{2.36a}$$

$$\tau_{sp,max} = 2I_r\omega_r\omega_g \tag{2.36b}$$

When evaluating the system against itself and other designs, equation 2.36b can be used to determine the maximum peak output possible of an ideal system.

2.9 Potential Average Torque in Ideal Conditions

Another good quantitative metric to use when designing a scissored-pair system is the comparison of the potential average output of the system to an individual design. This can be done using simple calculus. The average of any function can be determined by using the formula:

$$\tau_{sp,avg} = \frac{1}{b-a}\int_a^b f(x)d(x) \tag{2.37}$$

where $f(x)$ is the function of the output torque, and a and b are the upper and lower limits. In this case, we will examine the output torque average in terms of 2π, or one full rotation of θ_g. Substituting in equation2.29 to equation 2.37 yields

$$\tau_{sp,avg} = \frac{1}{b-a}\int_a^b \left(2I_r\omega_r\omega_g\cos\theta_g\right)d\theta_I \tag{2.38a}$$

$$\tau_{sp,avg} = \frac{2I_r\omega_r\omega_g}{b-a}\int_a^b \left(\cos\theta_g\right)d\theta_I \tag{2.38b}$$

$$\tau_{sp,avg} = \frac{2I_r\omega_r\omega_g}{2\pi-0}\int_0^{2\pi} \left(\cos\theta_g\right)d\theta_I \tag{2.38c}$$

$$\tau_{sp,avg} = \frac{4I_r\omega_r\omega_g}{2\pi-0}\int_0^{\pi} \left(\cos\theta_g\right)d\theta_I \tag{2.38d}$$

$$\tau_{sp,avg} = \frac{4I_r\omega_r\omega_g}{\pi} \tag{2.38e}$$

When evaluating the system against itself and other designs, equation 2.38e can be used to determine the possible average torque output of an ideal system.

2.10 Torque in Non-Ideal Conditions

As mentioned previously, non-ideal output torque is when the speed of the rotors is non-constant, $\alpha_r \neq 0$, or when body 1 is rotating in the inertial frame, meaning $\Omega_1 \neq 0$ and or $\Omega_2 \neq 0$ as discussed in equation 2.27. For this research, we are not concerned with body 1 rotation in the inertial frame, so we will focus soley on the non-ideal case when $\alpha_r \neq 0$ which is

$$\left\{I_T\alpha^{1/0}\right\}\hat{\mathbf{e}}_3^{(1)} = \left\{2I_r\alpha_r\sin\theta_g + 2I_r\omega_r\omega_g\cos\theta_g\right\}\hat{\mathbf{e}}_3^{(1)} \tag{2.28}$$

The introduction of the acceleration of the rotor, α_r, introduces a sine term into the equation which changes where the zero crossings of the function are. We can start to find the zero crossing by setting 2.28 equal to zero and solving for θ_g. We will call this special

value of θ_g, θ_0. θ_0 is the gimbal angle when the output torque along $\hat{\mathbf{e}}_3^{(1)}$ is equal to zero.

$$0 = 2I_r\alpha_r \sin\theta_0 + 2I_r\omega_r\omega_g \cos\theta_0 \tag{2.39a}$$

$$-\alpha_r \sin\theta_0 = \omega_r\omega_g \cos\theta_0 \tag{2.39b}$$

$$\tan\theta_0 = -\frac{\omega_r\omega_g}{\alpha_r} \tag{2.39c}$$

Therefore

$$\theta_0 = \tan^{-1}\left(-\frac{\omega_r\omega_g}{\alpha_r}\right) \tag{2.40}$$

Unlike the zero crossing in ideal settings, the zero crossings for non-ideal settings may change dependent on equation 2.40. In the best possible control setting for non-ideal conditions, the gimbal rate and acceleration will be at their maximum whenever possible. Therefore, we can look at equation 2.40 as a function of ω_r and set both α_r and ω_g to 1. The graph of this is shown in figure 2.18

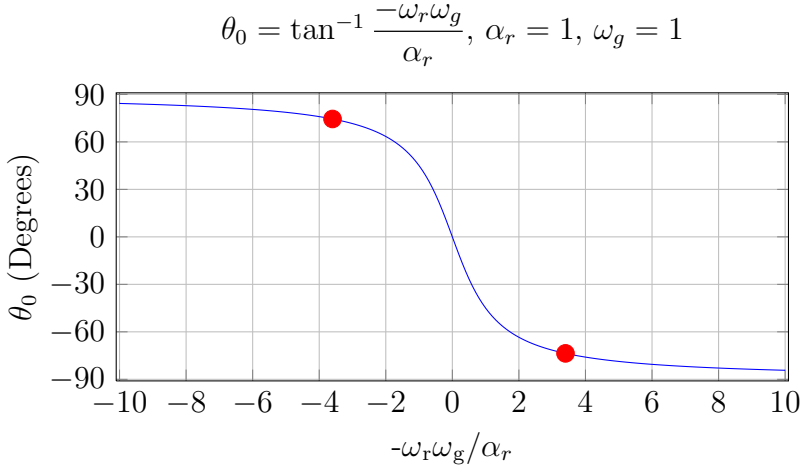

Figure 2.18: Control signals ω_g and ω_r and the corresponding output torque, τ_{sp} shown in a spacial domain in the Γ steady state.

We can see as ω_r increases or decreases in magnitude, the zero crosses are closer to $\pm\pi/2$. As ω_r is closer to zero, the zero crossings also come closer to zero, meaning that the output torque has a smaller span where it is negative.

The worst case scenario for a non-ideal configuration is when the the rotors are con-

stantly accelerating or decelerating, meaning that the sin term of equation 2.28 is always non zero. In the worst case, the velocity will change from $+\omega_{r,max}$ to $-\omega_{r,max}$ over a period of π radians. This event will take place dependent upon the gimbal rate, ω_g. Meaning that ω_g has a direct correlation to the magnitude of α_r through the equation

$$\alpha_r = \frac{\omega_{r,max}\omega_g}{\pi} \tag{2.41}$$

Equation 2.41 specifies the magnitude of the acceleration, but not the direction which in this instant is either positive of negative. The direction is based on the control algorithm and varies upon the specific use case. For that reason, we will add in a step function $u(t)$ to the acceleration component which can be either 1 or -1 depending upon the direction of the acceleration. Substituting this into equation 2.28 yields

$$\left\{I_T\alpha^{1/0}\right\}\hat{\mathbf{e}}_3^{(1)} = \left\{2I_r\frac{\omega_{r,max}\omega_g}{\pi}\sin\theta_g u(t) + 2I_r\omega_r\omega_g\cos\theta_g\right\}\hat{\mathbf{e}}_3^{(1)} \tag{2.42}$$

Furthermore, ω_r will be $\omega_{r,max}/2$ in a worst case scenario and substituting and simplifying yields

$$\left\{I_T\alpha^{1/0}\right\}\hat{\mathbf{e}}_3^{(1)} = 2I_r\omega_{r,max}\omega_g\left\{\frac{\sin\theta_g}{\pi}u(t) + \frac{cos\theta_g}{2}\right\}\hat{\mathbf{e}}_3^{(1)} \tag{2.43}$$

2.11 Controls in Non-Ideal Conditions

The control logic in non-ideal situations is similar to the ideal control logic shown in figure 2.16 except for two differentiations. First, ω_g is not at its maximum value for the entire duration. Second, ω_r does not switch instantaneously. In figure 2.19, ω_r requires a full 180 degrees to accelerate from its peak value to its peak value in the opposite direction. However, certain designs may not require this event to take place over 180 degrees.

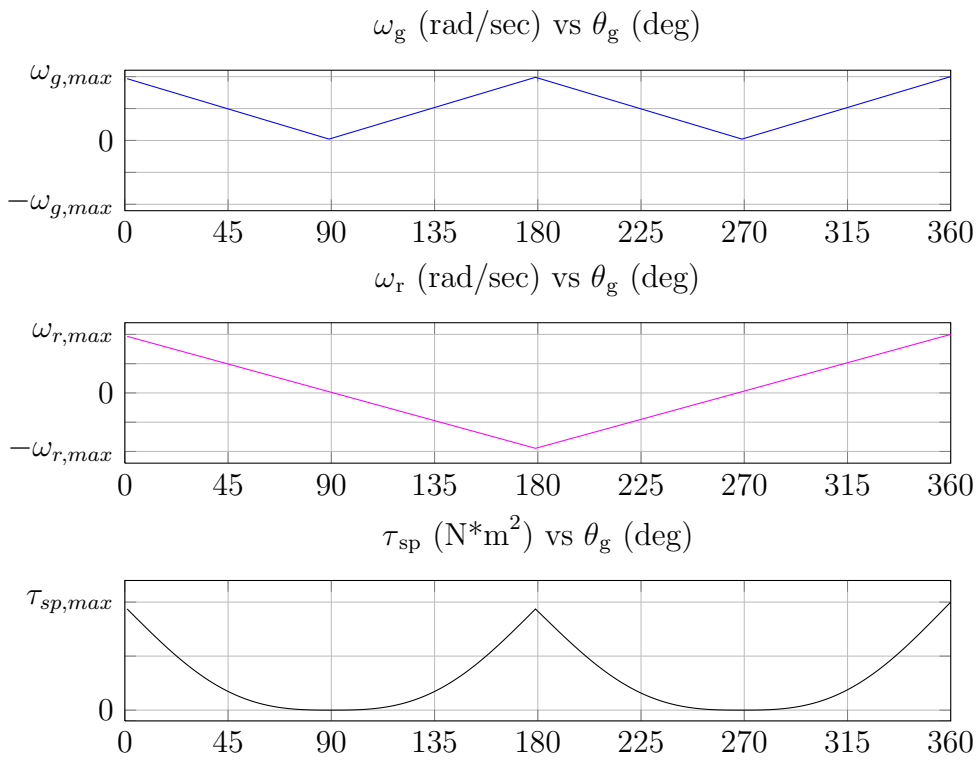

Figure 2.19: Control signals, θ_I, and output torque showing lumps of the Δ state. In this state, the torque is more evenly distributed across t

Figure 2.20 depicts what the output torque might look like if the acceleration of the rotor took place over a shorter period of time. The dotted lines in figure 2.20 show the deadband region of the output torque that is effected by the rotor acceleration/deceleration event. Furthermore, the size of the deadband has an effect on the potential output torque of the system. The larger the deadband, the less torque. If the deadband was zero, meaning that a rotor could instantaneously switch its rotation direction, there would be no loss in efficiency. Figure 2.21 shows the degree of the deadband vs the efficiency. Even in worst case scenario where the rotor requires a full 180 degrees to switch is rotational direction, the system is still around 65% efficient.

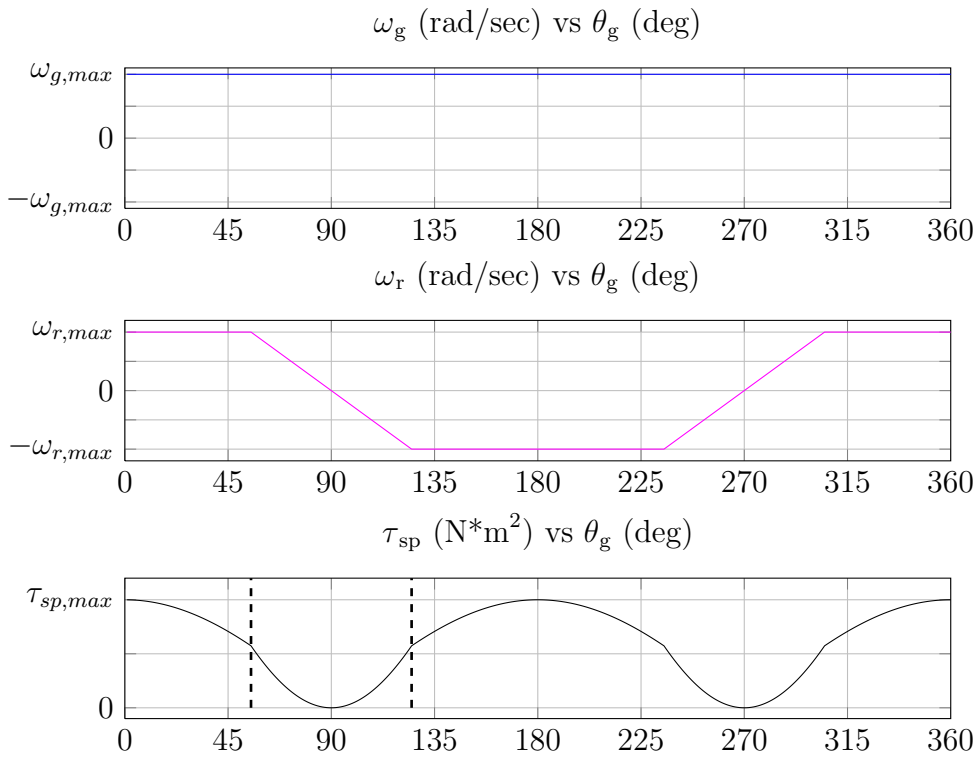

Figure 2.20: Control signals, θ_I, and output torque showing peaks of the Λ state. Torque is less evenly distributed across t, and represents a rectified sine wave.

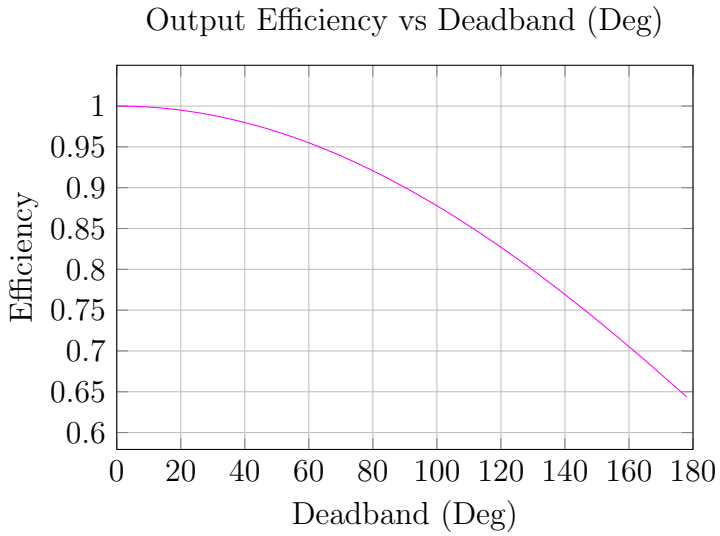

Figure 2.21: Control signals, θ_I, and output torque showing peaks of the Λ state. Torque is less evenly distributed across t, and represents a rectified sine wave.

Metrics calculated for ideal conditions, such as average and peak torques, are easily calculated due to the fact that the steady-states do not vary. However, for non-ideal conditions,ω_g, ω_r, and α_r vary during steady state conditions, and it is therefore easier to calculate in simulated environment as opposed to evaluation by a standardized equation as done before.

2.12 Dual SP-VSCMG Configurations

As previously mentioned, a scissored-pair system only offers a boost of torque, whereas a barycenter offset system can offer a constant torque. An approach to creating a constant output torque will be to design a dual scissored pair system, whose θ_g angles are offset from each other. Figure 2.22 is a visual depiction of this concept. A scissored pair system, shown as a dark box, is rigidly connected to a second system by the rod in the center of the system. The net torque for such a system was derived in equation 2.26. Due to the symmetry of the design, we can say that moments created when combining two pairs together will cancel out, and thus we can simply add the two torque matrices together. This addition yields

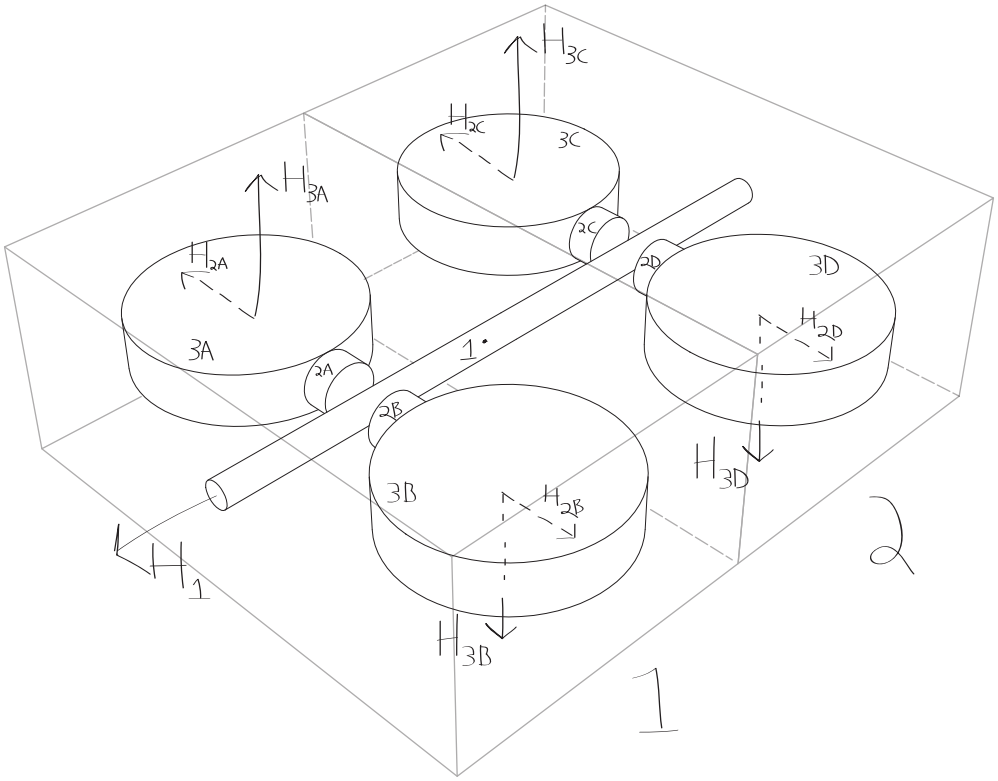

Figure 2.22: Combination of two scissored pairs with a rigid connection. Boxes indicate linkage number of the pair.

$$I_T\boldsymbol{\alpha}_1^{1/0} + I_T\boldsymbol{\alpha}_2^{1/0} = \left\{ \begin{array}{c} 2I_r^{[1]}\omega_r^{[1]}\Omega_2^{[1]}\sin\theta_g^{[1]} \\ -2I_r^{[1]}\omega_r^{[1]}\Omega_1^{[1]}\sin\theta_g^{[1]} \\ 2I_r^{[1]}\alpha_r^{[1]}\sin\theta_g^{[1]} + 2I_r^{[1]}\omega_r^{[1]}\omega_g^{[1]}\cos\theta_g^{[1]} \end{array} \right\} + \left\{ \begin{array}{c} 2I_r^{[2]}\omega_r^{[2]}\Omega_2^{[2]}\sin\theta_g^{[2]} \\ -2I_r^{[2]}\omega_r^{[2]}\Omega_1^{[2]}\sin\theta_g^{[2]} \\ 2I_r^{[2]}\alpha_r^{[2]}\sin\theta_g^{[2]} + 2I_r^{[2]}\omega_r^{[2]}\omega_g^{[2]}\cos\theta_g^{[2]} \end{array} \right\} \tag{2.44}$$

where the superscript $[n]$ notes what pair in the linkage the variable is referring to. Also, for notation, we will say that the sum of the torques of the two systems is

$$\tau_{dsp} = I_T\boldsymbol{\alpha}_1^{1/0} + I_T\boldsymbol{\alpha}_2^{1/0} \tag{2.45}$$

Previously, we defined

$$\omega^{1/0} = \Omega_1 \hat{\mathbf{e}}_1^{(1)} + \Omega_2 \hat{\mathbf{e}}_2^{(1)} + \Omega_3 \hat{\mathbf{e}}_3^{(1)} \tag{2.27}$$

which is the angular velocity of body 1 (the rod) with respect to the inertial frame. With the addition of the second scissored pair system, we will use the notation

$$\omega^{[n],1/0} = \Omega_1^{[n]} \hat{\mathbf{e}}_1^{(1)} + \Omega_2^{[n]} \hat{\mathbf{e}}_2^{(1)} + \Omega_3^{[n]} \hat{\mathbf{e}}_3^{(1)} \tag{2.46}$$

where $[n]$ is the number used to differentiate between linked scissored pairs. Since the two pairs are rigidly connected, the reference frames to each do not change. Substituting this into equation 2.44 yields

$$\tau_{dsp} = \left\{ \begin{array}{c} 2I_r^{[1]}\omega_r^{[1]}\Omega_2^{[1]} \sin\theta_g^{[1]} + 2I_r^{[2]}\omega_r^{[2]}\Omega_2^{[2]} \sin\theta_g^{[2]} \\ -2I_r^{[1]}\omega_r^{[1]}\Omega_1^{[1]} \sin\theta_g^{[1]} + 2I_r^{[2]}\omega_r^{[2]}\Omega_1^{[2]} \sin\theta_g^{[2]} \\ 2I_r^{[1]}\alpha_r^{[1]} \sin\theta_g^{[1]} + 2I_r^{[1]}\omega_r^{[1]}\omega_g^{[1]} \cos\theta_g^{[1]} + 2I_r^{[2]}\alpha_r^{[2]} \sin\theta_g^{[2]} + 2I_r^{[2]}\omega_r^{[2]}\omega_g^{[2]} \cos\theta_g^{[2]} \end{array} \right\} \tag{2.47}$$

Furthermore, we know that $I_r^{[1]} = I_r^{[2]}$, and substituting this into 2.47 and combining terms yields

$$\tau_{dsp} = \left\{ \begin{array}{c} 2I_r(\omega_r^{[1]}\Omega_2^{[1]} \sin\theta_g^{[1]} + \omega_r^{[2]}\Omega_2^{[2]} \sin\theta_g^{[2]}) \\ -2I_r(\omega_r^{[1]}\Omega_1^{[1]} \sin\theta_g^{[1]} + \omega_r^{[2]}\Omega_1^{[2]} \sin\theta_g^{[2]}) \\ 2I_r\left(\alpha_r^{[1]} \sin\theta_g^{[1]} + \omega_r^{[1]}\omega_g^{[1]} \cos\theta_g^{[1]} + \alpha_r^{[2]} \sin\theta_g^{[2]} + \omega_r^{[2]}\omega_g^{[2]} \cos\theta_g^{[2]}\right) \end{array} \right\} \tag{2.48}$$

Similar to the single scissored-pair, we can look at this equation in terms of ideal and non-ideal equations. The non-ideal situation we are interested in is when the system is not rotating with respect to the inertial frame, but the rotors have a non-zero acceleration.

This can be viewed as

$$\tau_{dsp} = \left\{ \begin{array}{c} 0 \\ 0 \\ 2I_r\left(\alpha_r^{[1]}\sin\theta_g^{[1]} + \omega_r^{[1]}\omega_g^{[1]}\cos\theta_g^{[1]} + \alpha_r^{[2]}\sin\theta_g^{[2]} + \omega_r^{[2]}\omega_g^{[2]}\cos\theta_g^{[2]}\right) \end{array} \right\} \tag{2.49}$$

The ideal situation is when the rotors have a zero acceleration as well, which yields

$$\tau_{dsp} = \left\{ \begin{array}{c} 0 \\ 0 \\ 2I_r\left(\omega_r^{[1]}\omega_g^{[1]}\cos\theta_g^{[1]} + \omega_r^{[2]}\omega_g^{[2]}\cos\theta_g^{[2]}\right) \end{array} \right\} \tag{2.50}$$

The offset between θ_g and $\theta_g^{[2]}$ determines the maximum, minimum, and average of the output torque. Figure 2.23 shows the normalized the ideal dual, scissored-pair output torque function, equation 2.50, plotted as a function of the difference between θ_g and $\theta_g^{[2]}$. The graphs were created using the ideal output torque for a dual scissored pair, as well as the ideal control logic, Δ. Due to the fact that we now have a second scissored pair, we will refere to the control logic as Δ^2.

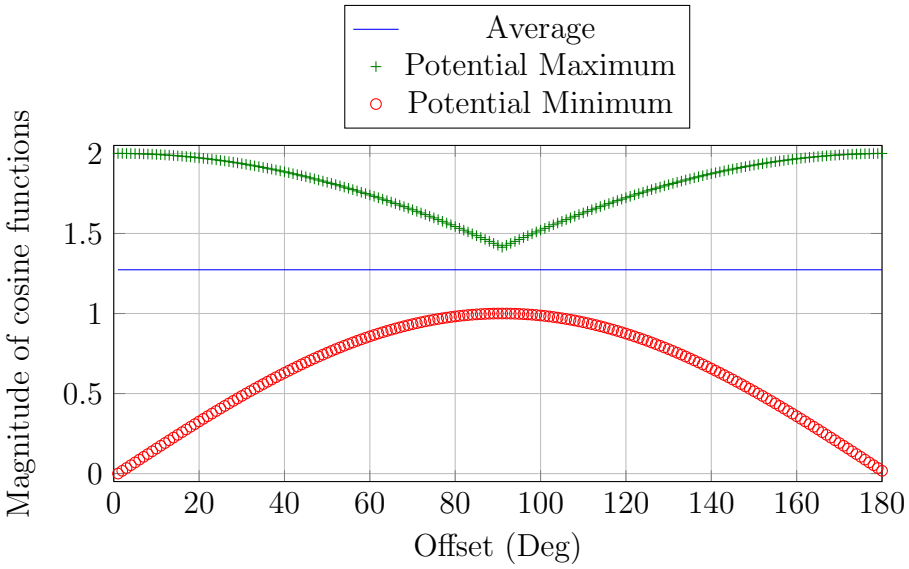

Figure 2.23: Plot showing the maximum, minimum and average potential torque of a dual scissored-pair system with respect to a varying offset

The figure shows three important facts. The first is that the average of the function remains the same regardless of the what the offset is. The second is that with a 0 or 180 degree offset, the output function can reach its maximum physical potential. However, the value will also drop to zero. The behavior of the output function with a 0 degree offset is shown in figure 2.24. The third fact is that at a 90 degree offset, the output function has its lowest maximum and highest minimum. This means that the output function has the smallest ripple at this point. The behavior of the output function with a 90 degree offset is shown in figure 2.25. It is important to note that with a 90 degree offset, the torque does not reach zero as it does in a single pair system.

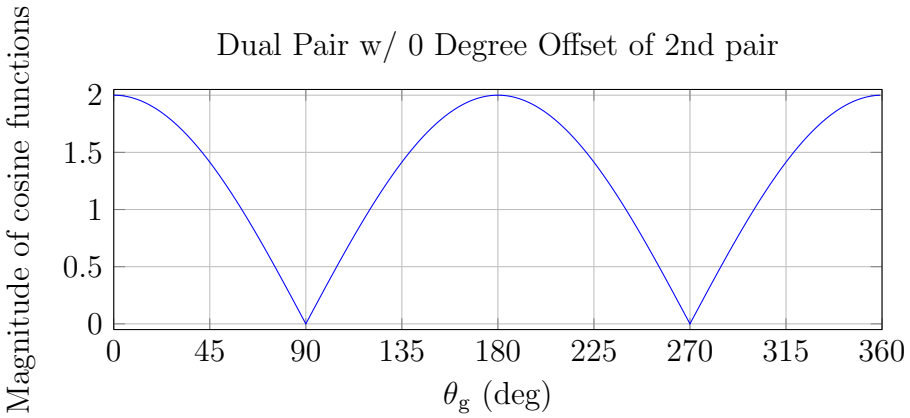

Figure 2.24: Normalized Δ^2 steady state with 0 offset between pairs, $\tau_{dsp,peak}$ of 2, $\tau_{dsp,min}$ of 0

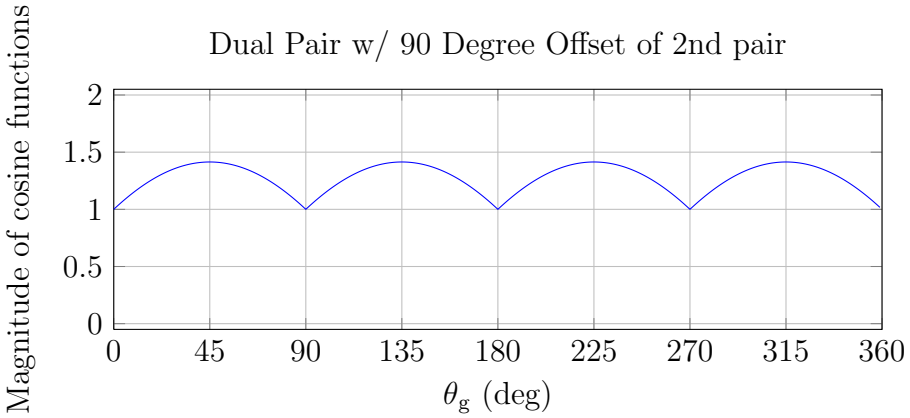

Figure 2.25: Normalized Δ^2 steady state with $\pi/2$ offset between pairs, $\tau_{dsp,peak}$ of 1.4, $\tau_{dsp,min}$ of 1

2.12 Conclusion

In this section we discussed the fundamental problem of the design, and how the center of gravity can never be shifted outside of the shell. The concept of transferring angular momentum to the outer shell as opposed to shifting the center of gravity was also introduced. Next, a brief review of control moment gyroscopes was given, followed by an introduction to the properties of a scissored pair. A set of torque equations of a scissored pair was then derived from first principles, followed by a discussion on an ideal scissored-pair system as well as potential minimum, maximum and average output torques. Non-ideal conditions were also discussed, as well as how these conditions effect the control logic as well as the net torque. With a single scissored pair described, the idea of adding a second scissored pair with a different phase than the first pair was introduced. The addition of the second scissored-pair creates the possibility of an entirely positive, non-zero output torque as shown by plotting the net torque with a varying phase angle. The next section will discuss how the system will be constructed and how it will be compared to a barycenter offset design.

Chapter 3: Modeling Conventional and Gyroscopic Spherical Robot Designs

Chapter Abstract

One of the key elements of the this research is to determine whether a spherical robot based on conservation of angular momentum will perform better than a spherical robot based on barycenter offset. In order to do this, the first step must be to determine what is actually being compared between the two systems and what defines a better performance. An analogy between two automobiles can be used to illustrate how the two types of robotic designs will be compared. How would a scientist compare an extremely light weight automobile versus a large sedan. The light weight automobile may be able to accelerate faster from resting, but may have a slower top speed than the sedan. The small automobile may be able to have a smaller turning radius, but the sedan may be able to handle turning with more weight on board. How can one be defined as having a better performance? They are both differently vehicles for different types of transport and have different characteristics. A small vehicle provides a certain need to the customer as does a large vehicle. Similarly, a spherical robot with a conservation of angular momentum based design will have different parameters than a barycenter offset design, but each will have its own specific set of advantages and disadvantages.

3.1 Introduction

Chapter 1 discussed the state of the art of actively driven spherical robots, and Chapter 2 discussed a theoretical actively driven system composed of a pair of SP-VSCMGs operating out of phase. In order to evaluate the performance of the Dual SP-VSCMG system, it must be compared to a barycenter offset system. With the theoretical Dual SP-VSCMG system introduced in Chapter 2, Chapter 3 will discuss the methods of using parametric analysis to improve the design and the fundamental equations related to the analysis. The analysis parameters will include, but are not limited to, peak and average torques, weight, velocity curves, acceleration curves, maximum incline, physical geometry, CMG geometry, and power considerations. Some of the design parameters that need to be calculated will be the spatial envelope in which a CMG occupies as it rotates, the weight of the sytem and the individual sub components, the maximum speed and torque of the motors, the physics of the robot on an incline, the bob size and weight, etc. A list of equations discussed throughout Chapters 1-3 will be summarized at the end of this chapter.

3.2 Key Elements to Model

In order to decide what aspects of the robot's construction need to be enhanced, the overall performance of the robot needs to be modeled. In a spherical robot, the main things to examine are power consumption, speed, and agility since other characteristics are simply derivations or combinations of those three main principles. Power consumption will be defined as the power and energy needed to maneuver the robot at the intended speed set out in the design. Speed is defined as the tangential velocity of the robot along its plane of travel. This is not to be confused with rotational speed of the robot. Due to equation of $v = \omega R_o$, two balls of varying outer radii may have the same tangential velocity if the angular velocity changes. This means that the angular velocity is a design parameter, and the tangential velocity is a performance parameter. Agility is how graceful the robot behaves and how quick and nimble it is. For example, does

it have a large or small turning radius? What is the stopping distance? Can it change direction instantaneously or does it need to reconfigure its position to traverse a different direction. Other important parameters to consider consist of, but are not limited to, incline plane, translational velocity and translational acceleration. In order to discuss the enhancements further, it would be best to have a clear understanding of the physics, orientations, and variables of the Dual SP-VSCMG system. The rotation of the system will be the first to be explained. A visual representation of the coordinate system is show in Figure 3.1. The bodies are as previously described, with the addition of two rotors and two gimbals, the second scissored pair. The rod is body 1, and has for gimbals attached to it, bodies 2A-2D. Attached to each gimbal is a rotor, bodies 3A-3D. Each body has its own frame, $\hat{\mathbf{e}}^{(n)}$. Each rotor will spin about its own $\hat{\mathbf{e}}_1^{(3n)}$-axis, in either a positive or negative direction depending on the configuration of the system. Each gimbal will rotate about its $\hat{\mathbf{e}}_2^{(2n)}$-axis, and the rod will rotate about its $\hat{\mathbf{e}}_3^{(1)}$-axis. The torque along this direction is what propels the robot forwards and backwards.

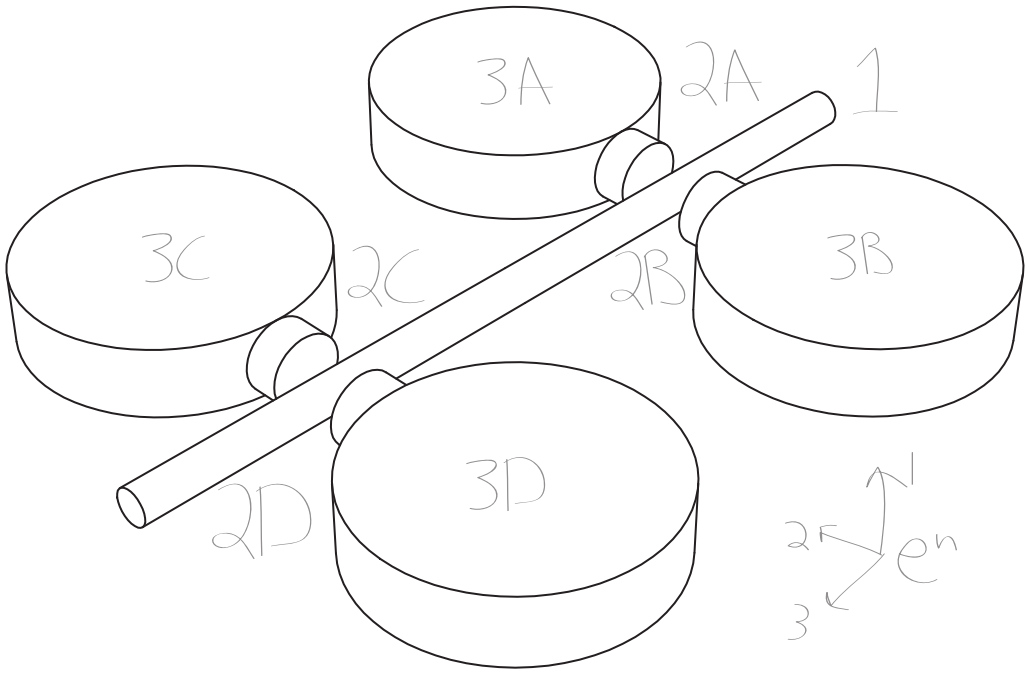

Figure 3.1: Layout of a dual, scissored-pair system in a spherical robot. The $\hat{\mathbf{e}}_1^{(3n)}$ axis is the direction of rotor torque, $\hat{\mathbf{e}}_2^{(2n)}$, the direction of gimbal torque, and $\hat{\mathbf{e}}_3^{(1)}$, the direction of output torque.

3.3 Description of the Three Types of Models

The basis for a barycenter offset model is pictured in Figure 3.2. Pictured is the outer shell radius, R_{shell}, the bob, the armature, the rod, and a physical placeholder for an output motor. The bob is the weighted mass that gives the output torque most of its value, and is currently pictured parallel to the horizon. At this position, the bob can generate the most torque on the motor. The armature connects the bob to the output rod. The output shaft goes through the diameter of the sphere and is connected to the output motor, which is turn drives the outer shell.

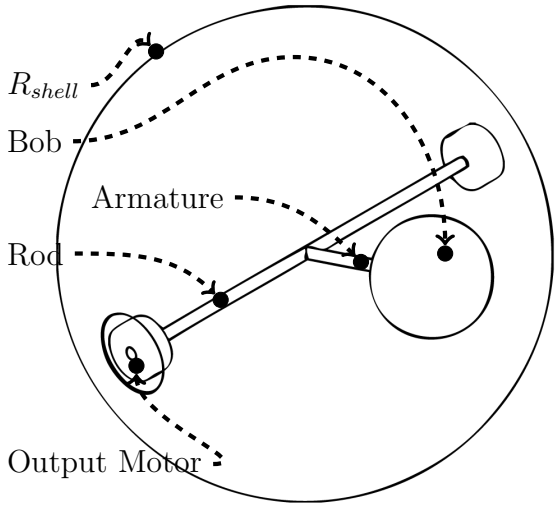

Figure 3.2: Basic barycenter offset model showing the outer shell radius, the bob, the center rod, the armature holding the bob, and the output motor that connects the rod to the outer shell

A basic SP-VSCMG model is pictured in Figure 3.3. Pictured is the outer shell radius, R_{shell}, the CMGs, the rod, and a placeholder for an output motor. The CMG is the weighted mass that gives the output torque part of its value. The CMG spins in both directions which are orthogonal to the output rod. As the CMGs spin, a precession torque is generated along the direction of the output rod allowing the robot to spin. In this case, the armature is the C-shaped device holding the CMG to the output rod.

A DSP-VSCMG model is pictured in Figure 3.3. Pictured is the outer shell radius, R_{shell}, the CMGs, the rod, and a placeholder for an output motor. The CMG is the

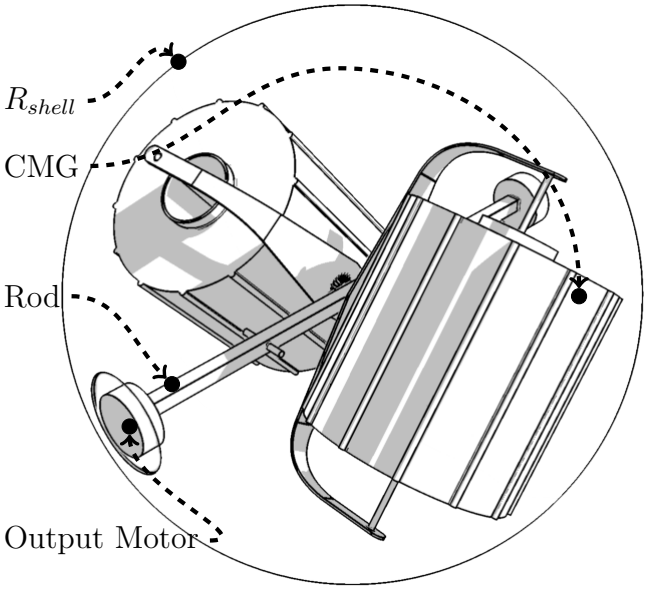

Figure 3.3: Basic SP-VSCMG model showing the outer shell radius, the CMGs, the center rod, and the output motor that connects the rod to the outer shell

weighted mass that gives the output torque part of its value. The CMG spins in both directions which are orthogonal to the output rod. As the CMGs spin, a precession torque is generated along the direction of the output rod allowing the robot to spin. In this case, the armature is the C-shaped device holding the CMG to the output rod. The DSP-VSCMG is similar to the SP-VSCMG except there are two pairs of CMGs instead of one.

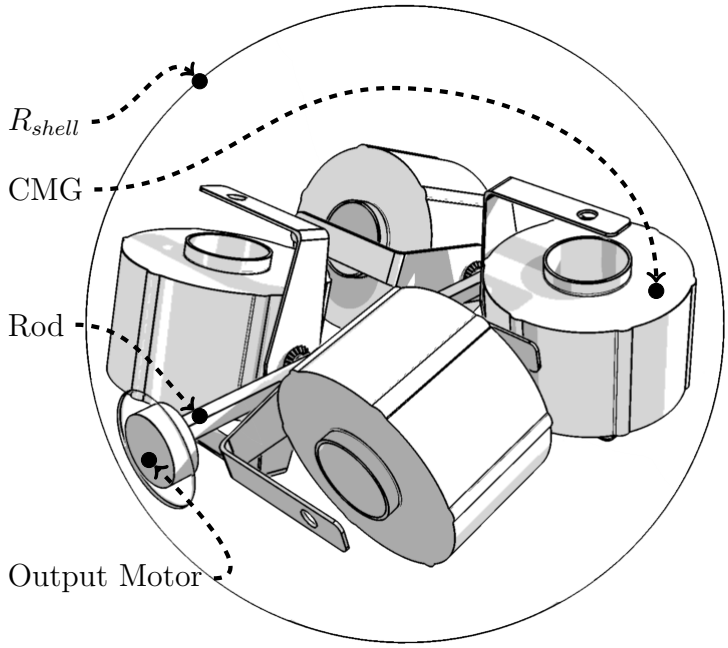

Figure 3.4: Basic Dual SP-VSCMG model showing the outer shell radius, the CMGs, the center rod, and the output motor that connects the rod to the outer shell

3.4 Modeling Power Consumption

At is current level of design, the power consumption is modeled at a high level. A manufacturable design will have many additional components modeled into it such as motors, bearings, gears, etc. All of these will have an effect on the power required to control the robot. At this current stage, a system level model will provide suitable information to determine the power needs of the robot. The system level model for the spherical robot will be a simple configuration: a battery provides power to the motors, the motors rotate the CMGs, and mechanical constraints provide power to the output shaft due to the laws of conservation of angular momentum.

The first step in modeling the power is to determine how much power is required by the battery. The battery is converted to mechanical energy by the motors with an efficiency loss, the motors transfer the mechanical energy to rotational energy with some energy loss (not modeled), and the rotational energy position is changed through mechanical constraints with some energy loss (not modeled).

However, for the system level model, it will be assumed that the final manufacturable design of the system will be made as power efficient as possible. The following assumptions will be made. First, there will be no loss of energy through the wiring from the batteries to the motors. This loss will be small in the final design, but will be ignored at this state. There will be no power loss from the motor to the CMG's, however, there will be an efficiency coefficiant correlated to the motors. This means that it will take energy to convert the electrical power from the batteries to the motor, but it will not take extra energy to transfer the motor energy to the CMGs. Thirdly, there will be no loss in the mechanical system between the rotation of the CMGs and the power seen at the output shaft. In the final design, gears, bearings, and friction will have increased this loss but is neglected at this point.

The derivation of the equation used to estimate power is show in the text below. Firstly, we have assumed that there is no loss between the battery and the motor. So

$$P_{battery} = P_{motor}$$

Factoring in the efficiency of the motor, the equation becomes

$$P_{battery} * \eta_{motor} = P_{mechanical}$$

It is important to note that the efficiency of the motor, η_{motor}, will be determined by the properties of the motors described from the motor manufacturer. η_{motor} may change at certain RPMs and power levels. It is also assumed that the mechanical energy from the motor will be stored in the CMGs as rotational power, $P_{rotational}$, without loss as seen in the equation below.

$$P_{mechanical} = P_{rotational} = \tau_o \omega_{avg}$$

where ω_{avg} is the angular velocity of the CMG over a period of time. Also, electrical

Power is equal to

$$P_{battery} = VI$$

Putting this altogether, these equations can be modeled as

$$VI\eta_{motor} = \tau_o \omega_{avg} \tag{3.1}$$

where τ_o is the torque along the rod on the $\hat{\mathbf{e}}_3^{(1)}$, or in other words the output torque.

3.5 In-Depth Look at Power Consumption Model

Assuming the model discussed above is accurate and discounting the losses from friction, air, etc, discussed above, a more in depth modeling equation will be needed in order to calculate power and torque requirements in real time. Since it is assumed that the ball is rotating without unecessary friction, the torque of the system will only change when the speed of the system changes. For example, if the ball is moving along at a certain speed, the ball will continue to roll until friction slows it down. In this model, friction is neglected, so the only force able to slow the ball down will be a torque in the opposite direction. Below is the derivation of the equation that illustrates the power required to change the velocity of the ball given a set of initial conditions.

Assume that ball is traversing on a flat plane. The outside shell of the ball will be rotating and moving forward, thus having an angular and translational velocity. The inside of the ball, the armature, will not be rotating and only have a translational velocity associated with it. From modern physics, it has been proven that change in energy is equal to rotational kinetic energy plus translational kinetic energy of the system.

$$\Delta K_E = \frac{1}{2} m_{system} v^2 + \frac{1}{2} I \omega_{system}^2$$

and

$$\Delta K_E = \text{Work} = \text{Energy loss of a system}$$

Expanding this equation know the fact that the armature of the ball is not rotating yields

$$\Delta K_E = \frac{1}{2} I_s(\Delta\omega_o^2) + \frac{1}{2} m_{shell}(\Delta v_o^2) + \frac{1}{2} m_{arm}(\Delta v_{arm}^2) \tag{3.2}$$

where I_s is the intertia of the shell. Since no outside forces are acting on the system, torques generated on the output shaft are the only forces at work. This work can be quantified as

$$W = \tau_o \theta_o$$

thus

$$\Delta K_E = \tau_o \theta_o \tag{3.3}$$

Substitutin in (3.1) into 3.3 yields

$$\Delta K_E = \frac{V I \eta_{motor} \theta_o}{\omega_{avg}} \tag{3.4}$$

The translational velocity of the shell and the armature are the same since the are attached, the translational velocites can be combined. Furthermore, the mass of the shell plus the mass of the armature is equal to the mass of the entire system. Combining these elements and substituting (3.4) into 3.2 yields

$$\frac{\left(\frac{1}{2} I_s(\omega_{o,f}^2 - \omega_{o,i}^2) + \frac{1}{2} m_{net}(v_{o,f}^2 - v_{o,i}^2)\right) * \omega_{avg}}{\theta_o \eta_{motor}} = VI$$

Also

$$\frac{(\omega_{o,f}^2 - \omega_{o_i}^2)}{2\alpha_o} = \theta_o$$

so

$$\frac{\left(\frac{1}{2}I_s(\omega_{o,f}^2 - \omega_{o,i}^2) + \frac{1}{2}m_{net}(v_{o,f}^2 - v_{o,i}^2)\right)\omega_{avg}2\alpha_o}{\eta(\omega_f^2 - \omega_i^2)} = VI$$

Multiplying coeffiecients through in the numerator and substituting in $v = \omega r$ yields

$$\frac{\left(I_s(\omega_{o,f}^2 - \omega_{o,i}^2) + m_{net}R_o^2(\omega_{o,f}^2 - \omega_{o,i}^2)\right)\omega_{avg}\alpha_o}{\eta(\omega_f^2 - \omega_i^2)} = VI$$

Simplifying this equation gives an equation for estimating the power of the system at finite point in time

$$\frac{(I_s + m_{net}R_o^2)\omega_{avg}\alpha_o}{\eta_{motor}} = VI \tag{3.5}$$

An alternate form of this equation that will be useful to determine power usage over a period of time which can be solved knowing that

$$\frac{\omega_f - \omega_i}{t} = \alpha \text{ and } \frac{\omega_f + \omega_i}{2} = \omega_{avg}$$

$$\frac{(I_s + m_{net}R_o^2)(\omega_{o,f}^2 - \omega_{o,i}^2)}{2t\eta_{motor}} = VI \tag{3.6}$$

3.6 Modeling CMG Power Usage

The rotational kinetic energy used to bring a CMG's rotational velocity from 0 rad/sec to ω rad/sec is

$$E_r = \frac{1}{2}I_r\omega_r^2 \tag{3.7}$$

In each of the oscillation states, the rotational velocity goes from $+\omega_s$ to $-\omega_s$ and from $-\omega_s$ to $+\omega_s$ meaning that the total energy used by the CMGs in one rotation of θ_I is

$$\Delta K_E = 4I_r\omega_r^2 \tag{3.8}$$

This energy is dissipated over a period of 2π, or one full rotation of the gimbals. The time it takes to dissipate the energy is determined by the gimbal rate, or

$$t = \frac{2\pi}{\omega_g} \tag{3.9}$$

meaning that the power used to spin the CMGs for one cycle of a SPVSCMG system is

$$P_r = 4I_r\omega_r^2\left(\frac{\omega_g}{2\pi}\right) \tag{3.10}$$

3.7 Modeling Translational Velocity

Translational velocity can simply be described as

$$\omega_f = \omega_i + \alpha t \text{ and } \frac{\tau}{I} = \alpha$$

yields

$$\omega_f = \omega_i + \frac{\tau}{I}t \tag{3.11}$$

Furthermore, this equation can also be used with (3.5) and 3.6 to determine how much power is required to accelerate to the final angular velocity. Also, the translational velocity can be determined simply by using $v = \omega r$.

3.8 Maximum Inclined Plane

The maximum plane of incline is also important to determine when doing physical modeling of the robot. Creating a set of equations corresponding to the incline will allow the modeling enviroment to solve for the amount of torque need to move the robot up an incline, which then can be used to solve for the amount of power needed. A picture of the robot traversing up an incline is shown in Figure 3.5.

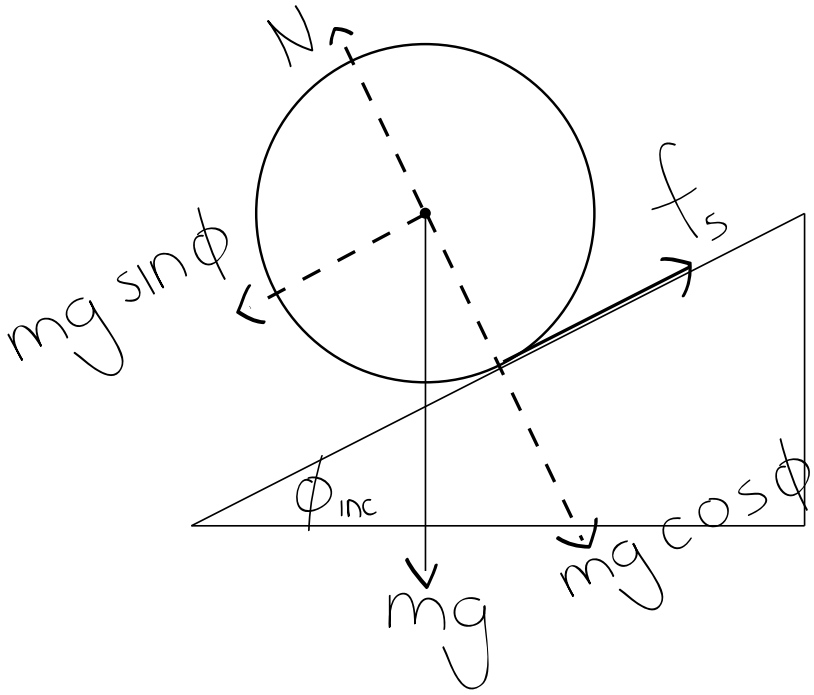

Figure 3.5: Force diagram of a spherical robot rolling up an incline, ϕ_{inc}

The torque acting on the output shaft from gravity can be described as

$$\tau_{gravity} = m_{net} g R_o \sin \phi_{inc} \tag{3.12}$$

where m_{net} is the total mass of the robot, R_o is the radius of the outer shell, ϕ_{inc} is the incline, and $\tau_{gravity}$ is the torque applied at the center point of the robot due to gravity. Assuming no loss from friction or air, the only other torque acting on the output shaft is the torque generated by the drive mechanism on the inside of the ball, τ_o. This torque can be from any type of drive system. In this instance, it can be from either a barycenter offset system or a Dual SP-VSCMG system. Consider a situation where a spherical robot is motionless on an inclined plane. For the robot to remain in its position, the sum of the torques must equal zero. If the robot is to accelerate upwards, the torque output by the drive mechanism must be greater than the torque from gravity. Using these conditions, we can solve for the an estimation of the maximum slope that the robot can accelerate up by the method below.

$$\tau_o - \tau_{gravity} = \Delta\tau \tag{3.13a}$$

Set $\Delta\tau$ to 0 to solve for stall torque (3.13b)

$$\tau_o - \tau_{gravity} = 0 \tag{3.13c}$$

$$\tau_o = m_{net} g R_o \sin\phi_{inc} \tag{3.13d}$$

$$\frac{\tau_o}{m_{net} g R_o} = \sin\phi_{inc} \tag{3.13e}$$

$$\sin^{-1}\frac{\tau_o}{m_{net} g R_o} = \phi_{inc} \tag{3.13f}$$

Equation 3.13f can be examined further by evaluating τ_o for a barycenter offset and a Dual SP-VSCMG system. The examination of a barycenter offset system is described below. For a barycenter offset system, it has been proven in this document that

$$\tau_o = m_{arm} g r_{cm,arm} * \sin(\theta_b)$$

where m is equal to the mass of the bob and the armature, r is equal to distance of the center of mass of the bob and armature combined to the epicenter of the robot, and $\sin\theta_b$ is equal to the angle between the armature and direction of gravity. For modeling, it is assumed that θ_b is always 90, and thus $\sin\theta_b$ is always 1. It is also assumed that the mass of the enitre robot, m_{net}, is equal to the mass of the arm, m_{arm}, plus the mass of the outer shell, m_{shell}. Incorporating this information into equation 3.13f yields

$$\frac{m_{arm} r_{cm,arm} g \sin\theta_b}{\Big(m_{arm} + m_{shell}\Big) g R_o} = \sin\phi_{inc} \tag{3.14a}$$

Manipulating this equation yields

$$\sin^{-1} \frac{1}{\left(1 + \frac{m_{shell}}{m_{arm}}\right)\left(\frac{R_o}{r_{cm,arm}}\right)} = \phi_{inc} \tag{3.14b}$$

Plotting $\phi = \arcsin x$, where $-\pi < x < \pi$, yields the graph shown in Figure 3.6. As x nears 1, ϕ becomes closer to 90 degrees, meaning that the robot can climb a steaper slope as x becomes closer to 1. Examing equation 3.14b shows that as the denominator becomes closer to 1, the robot will have the ability to climb up a steeper slope. The denominator of equation 3.14b can never be less than 1 as the ratio of the mass of the outer shell to the mass of the armature will never be massless, and the ratio of the radius of the outer shell to radius of the center or mass of the armature will always be greater than 1 since the armatures center of mass can not exist outside of the outer shell. This means that $0 < x < 1$ and thus $0 < \phi < \frac{\pi}{2}$. By using equation 3.14b, a fair estimation of the maximum incline that a barycenter offset spherical robot can climb up can be calculated.

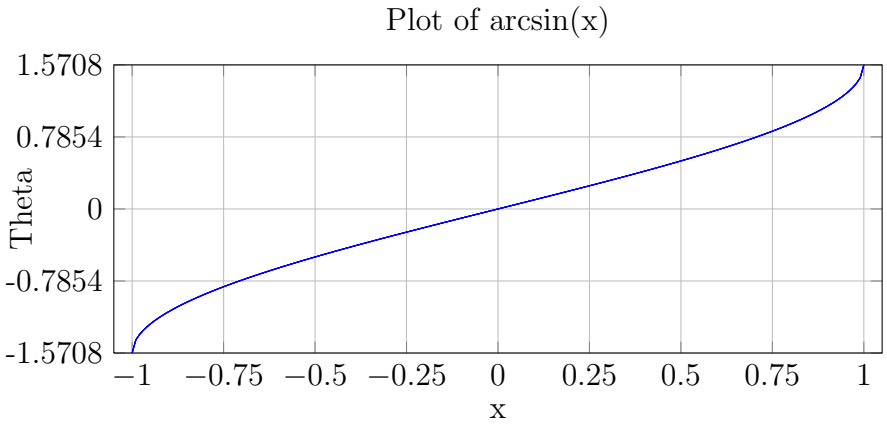

Figure 3.6: Behavior of generic equation, $y = \arcsin x$. Notice the asymptotes at 1 and -1, which indicates the robot would be climbing up a 90 degree slope.

Simlarly, we can substitute the torque output equation for a SP-VSCMG system into

equation 3.13a to yield

$$\sin^{-1} \frac{|2I_r\alpha_r \sin\theta_g + 2I_r\omega_r\omega_g \cos\theta_g|}{m_{net}gR_o} = \phi \tag{3.15}$$

for a non-ideal system and

$$\sin^{-1} \frac{|2I_r\omega_r\omega_g \cos\theta_g|}{m_{net}gR_o} = \phi \tag{3.16}$$

for an ideal system.

The addition of the $\Delta\tau$ term from equation 3.13a is needed in order to evaluate the arcsin function in the domain of -1 to 1. If the $\Delta\tau$ term was not included, the function would return imaginary results. For a Dual SP-VSCMG system, the τ_o term is dynamic, meaning it changes depending on the state of the system. For that reason, a generic equation can not be used to model the maximum incline, but it can, however, be calcluated in real time when the system conditions are known.

3.9 Modeling Maximum Step Size From Rest

Figure 3.7 illustrates how a spherical robot will climb a slope from rest. Image 3.7 a. shows the robot resting up against the step. As it attempts to move forward, it will roll up the step. Assuming no slippage, the outer shell of the robot will pivot at the highest point of the step, and the inner armature, either a SP-CMG or a barycenter offset system, will not rotate as shown in 3.7 b. Finally, the robot will end its climb of the step with the outer shell rotated 90 degrees and the inner armature remaining unrotated as shown in 3.7 c. A view of the forces in action can be seen in 3.8.

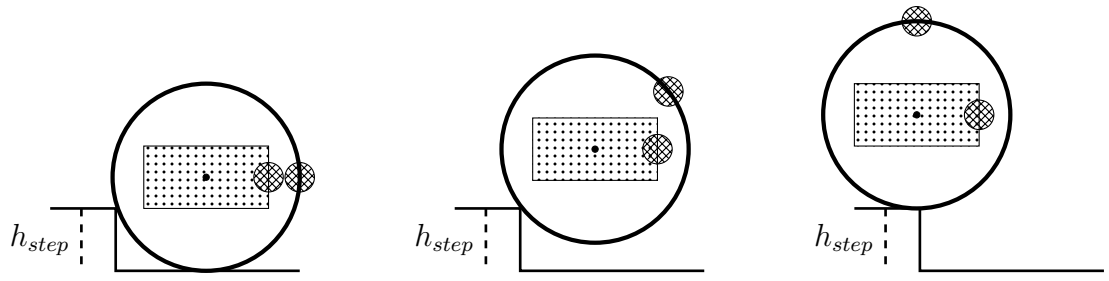

(a) At rest (b) Ascending (c) Stopped

Figure 3.7: Behavior of a spherical robot ascending a step

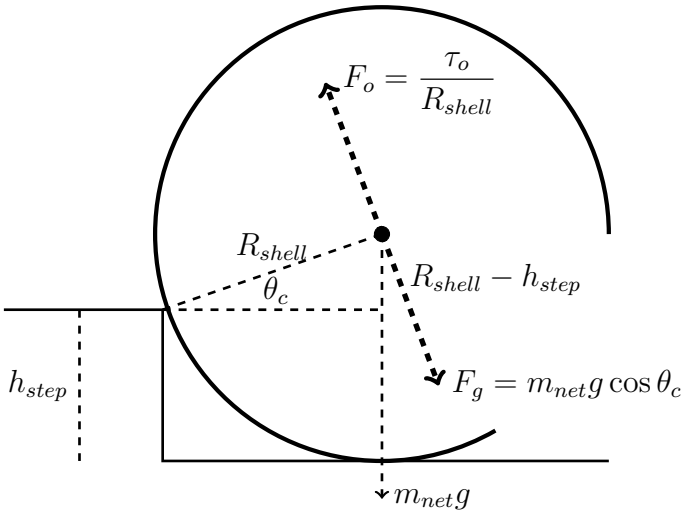

Figure 3.8: Forces acting on a spherical robot ascending a step

From Figure 3.8, we can determine that

$$\sin\theta_c = \frac{R_{shell} - h_{step}}{R_{shell}} \tag{3.17a}$$

$$F_g = m_{net} g \cos\theta_c \tag{3.17b}$$

$$F_o = \frac{\tau_o}{R_{shell}} \tag{3.17c}$$

In order for the robot to climb over the step, pivoting about the highest point of the step, F_o must be greater than F_g. In other words, $\tau_o - \tau_g > 0$. It can also be said that for equilibrium , $\tau_g = \tau_o$. We can solved for the minimum step size a system can roll over by expanding this idea, which yields

$$\tau_o - R_{shell} m_{net} g \cos\left(\arcsin\left(\frac{R_{shell} - h_{step}}{R_{shell}}\right)\right) = 0 \tag{3.18}$$

Using the trig identity

$$\cos\arcsin x = \sqrt{1 - x^2} \tag{3.19}$$

and the quadratic equation, we can solve for h_{step}

$$h_{step} = R_{shell} \pm \sqrt{\left(R_{shell}^2 - \frac{\tau_o^2}{m_{net}^2 g^2} \right)} \tag{3.20}$$

To examine this idea further, we can plug in the output torque equation for a barycenter offset design into (3.20) which yields

$$h_{step} = R_{shell} - \sqrt{\left(R_{shell}^2 - \frac{r_{cm,bob}^2 m_{arm}^2 g^2}{(m_{arm} + m_{shell})^2 g^2} \right)} \tag{3.21}$$

Let us then assume that the designer of the system can minimize the weight of the shell to near zero and thus m_{shell} becomes zero. We can then simplify the equation to become

$$h_{step} = R_{shell} - \sqrt{R_{shell}^2 - r_{cm,bob}^2} \tag{3.22}$$

Now, lets take this one step further and say that $r_{cm,bob}^2$ is a percentage, x, of R_{shell}. We can then manipulate the equation in the following manner.

$$h_{step} = R_{shell} - \sqrt{R_{shell}^2 - (xR_{shell})^2} \tag{3.23a}$$

$$h_{step} = R_{shell} - \sqrt{R_{shell}^2 - x^2 R_{shell}^2} \tag{3.23b}$$

$$h_{step} = R_{shell} - \sqrt{R_{shell}^2 (1 - x^2)} \tag{3.23c}$$

$$h_{step} = R_{shell} - R_{shell}\sqrt{1 - x^2} \tag{3.23d}$$

$$h_{step} = R_{shell}(1 - \sqrt{1 - x^2}) \tag{3.23e}$$

From (3.23e) we can see that as x becomes closer to 1, h_{step} will increase. This is shown in the graph of (3.23e) is shown in Figure 3.9. It is important to note that the h_{step} becomes imaginary when x is greater than 1. This is because physically, a ball can not climb a step with a height that is greater than radius. In a barrycenter offset design, the r_{bob} will never equal R_{shell}, meaning that the center of gravity never exists outside of the shell. However, in a SP-VSCMG design, it can. This means that a SP-VSCMG design can overcome a step size equal to that of its outter radius. This can be shown by

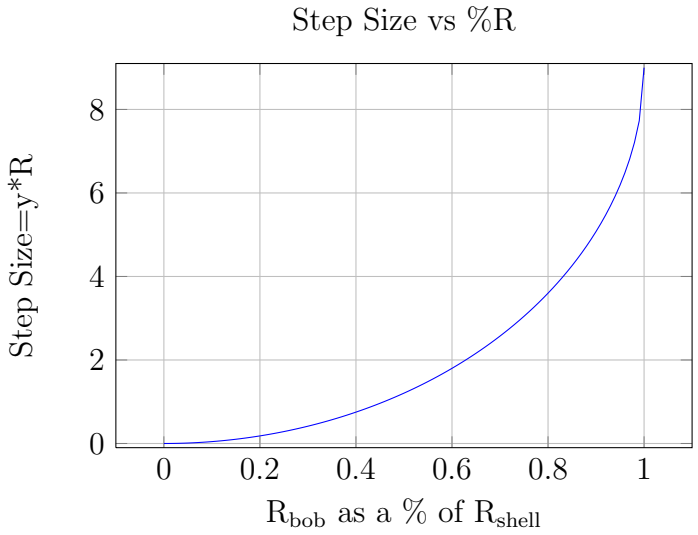

Figure 3.9: Step size a spherical robot can ascend based on the offset of the barycenter as a percentage of the shell radius.

substituting in the output torque of a SP-VSCMG design into (3.20).

3.10 Defining Volumes for Parametric Analysis

The volume of the robot can be modeled by examing the geometry of the components. In this section, the following geometries will be examined:

V_{robot} = The volume of the robot

R_{shell} = The radius of the robot shell (m)

V_{bound} = An imaginary sphere inside V_{robot} in which a CMG can rotate without obstruction

R_{bound} = The radius of the imaginary CMG bounding sphere.

h_{CMG} = The height of the cylindrical CMG as show in Figure 3.10

r_{CMG} = The radius of the cylindrical CMG as show in Figure 3.10

3.10 Determining Inertia of CMG

As the CMG spins about the 1-axis, it will also rotate about a perpendicular axis, the 2-axis. The CMG will require a free space to rotate about the 2-axis (axis of gimbal torque), and this is called the bounding sphere as shown in Figure 3.10. In order to enhanced the performance of the system, the CMG inertia must be maximized while still

being constrained to the geometrical limitations of the bounding sphere. To calculate this, we will assume a standard CMG shape of a cylinder, which is the standard shape used in practice. Other shapes may be used, but a cylinder is used so that the system is balanced.

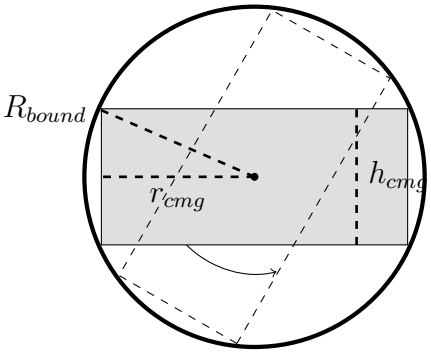

Figure 3.10: Slice of a CMG in an imaginary bounding sphere. The CMG (rectangle) rotates about the center point

Using the Pythagorean theorem in reference to figure 3.10, we can see that

$$\frac{1}{4}h_{CMG}^2 + r_{CMG}^2 = R_{bound}^2 \tag{3.24a}$$

or

$$h_{CMG} = 2\sqrt{R_{bound}^2 - r_{cmg}^2} \tag{3.24b}$$

We also know that inertia is a function of the height and the width of the CMG. Knowing this, we can calculate the inertia for a CMG depending on its geometry. In this example, we will use a solid disc as the geometry. Inertias for other geomtries, such as spoked ring, can be used by doing similar calculations as shown below. The rotational inertia for a disc (see Figure 3.1 for dimensions) are as follows:

$$I_x = \frac{1}{2}m_{CMG}r_{CMG}^2 \tag{3.25a}$$

$$I_z = I_y = \frac{1}{12}m_{CMG}(3r_{CMG}^2 + h_{CMG}^2) \tag{3.25b}$$

Mass of the CMG is

$$m_{CMG} = \rho\pi r_{CMG}^2 h_{CMG} \tag{3.26a}$$

or

$$m_{CMG} = 2\rho\pi r_{CMG}^2 \sqrt{R_{bound}^2 - r_{CMG}^2} \tag{3.26b}$$

Substituting (3.26b) into equations 3.25 yields

$$I_x = \rho\pi r_{CMG}^4 \sqrt{R_{bound}^2 - r_{CMG}^2} \tag{3.27a}$$

$$I_z = I_y = \frac{1}{6}\rho\pi r_{CMG}^2 (4R_{bound}^2 - r_{CMG}^2)\sqrt{R_{bound}^2 - r_{CMG}^2} \tag{3.27b}$$

These equations can be substituted into the master torque equation, (2.33) to adjust the weight, torque and size of the CMG for enhanced performance. The analysis parameters will depend on what the design of the systems requires. For example, in order to gain more torque from the system, the weight and size of the CMG may increase. An example of this will be shown in the results portion of this document.

3.10 Determining Bounding Sphere Size

Next, it is neccessary to calculate the maximum size of the bounding sphere that can fit inside of spherical shell. For the best results, the design should be symmetrical about the axis of rotation. This document has briefly discussed a SP-VSCMG and a Dual SP-VSCMG design, each having two and four internal gyroscopes, repsectively. Given the outer shell radius, R_{shell}, we can calculate the maximum size of the bounding sphere sizes of each design. A cross section of both of the designs is shown in Figure 3.11, illustrating the outer shell radius and the configuration of the respective bounding spheres.

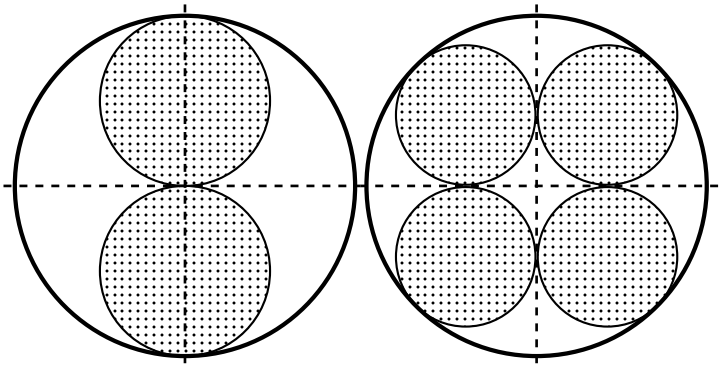

Figure 3.11: Cross sections of bounding spheres illustrating the configuration that yields the largest bounding sphere size

From the geometry we can figure out the maximum bounding sphere size possible given the radius of the outer shell. The respective bounding sphere sizes in terms of the outer shell radius are:

$$R_{bound,dual} = \frac{R_{shell}}{2} \tag{3.28}$$

$$R_{bound,quad} = \frac{R_{shell}}{(1+\sqrt{2})} \tag{3.29}$$

3.11 Defining Barycenter Offset Models

In order to evaluate the performance of a Dual SP-VSCMG design, the parameters must be compared to a control group. The control group for this examination will be calculated from a a barycenter offset spherical robot with varying bob sizes. There is a trade off between bob sizes inside of barycenter offset designs. The heavier that the bob is, the more torque the drive train can generate. However, the larger the bob, the shorter the offset of the center of gravity, meaning less torque. This is illustrated in figure 3.12. As the bob size increases, so does the space that it takes up. This visual representation is shown in Figure 4.1. We know that the torque from a barycenter offset system is

$$\tau_{max} = m_{bob} g (R_{shell} - r_{bob}) \tag{3.30a}$$

and the mass of the bob is equal to

$$m_{bob} = \frac{4}{3}\pi\rho r_{bob}^3 \tag{3.30b}$$

So it can be said that

$$\tau_{max} = \frac{4}{3}\pi\rho g r_{bob}^3 (R_{shell} - r_{bob}) \tag{3.30c}$$

The normalized plot of (3.30c) is shown in figure 3.12. It can be seen that τ_{max} is at its greatest when $r_{bob} = 0.75R_{shell}$. This can also be solved be taking the derivative of (3.30c). From the plot, we will select 4 bob sizes to compare the Dual SP-VSCMG models to. The first will be when $r_{bob} = 75\%R_{shell}$ because it is the the solution for maximized torque. The second, third, and fourth will be when r_{bob} is equal to $50\%R_{shell}$, $33\%R_{shell}$, and $25\%R_{shell}$. This is visually represented in Figure 4.1 as well as graphically represented in Figure 3.12 as red dots.

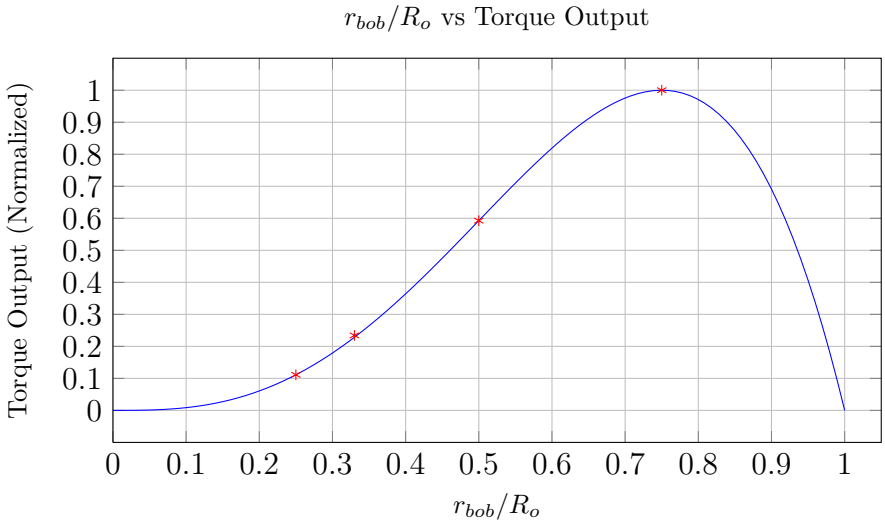

Figure 3.12: Torque output based on the bob radius, where the bob radius is a percentage of the the outer shell radius

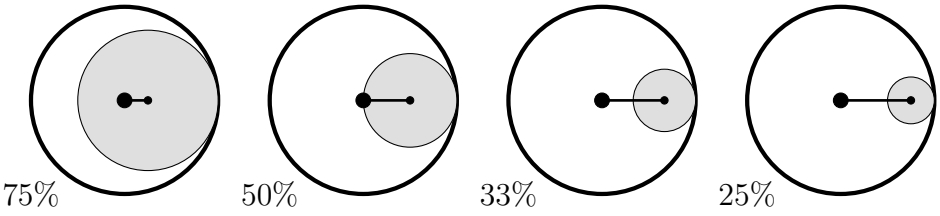

(a) $.75R_{shell}$ (b) $.50R_{shell}$ (c) $.33R_{shell}$ (d) $.25R_{shell}$

Figure 3.13: Visual reference of different bob sizes (gray) in a barycenter offset system. Electronics and motors must be able to fit into the remaining space (white)

3.12 Determining CMG Motor Torque

The CMG motor heavily effects the rate at which the ω_r can change direction, which directly effects ω_g and θ_g. The Λ^2 state is the behavior that will be used for this examination of the CMG Motor Torque. The controls signals for the Δ^2 state were describe in an ideal environment, meaning that $-\omega_s$ could go to ω_s instantaneously. In reality, this is not the case. A non-ideal (realistic) control situation can be seen in figure 3.14. It is important to notice that this control behavior is for one SP-VSCMG. The second SP-VSCMG system would behave the same as this system, just out of phase by 90 degrees.

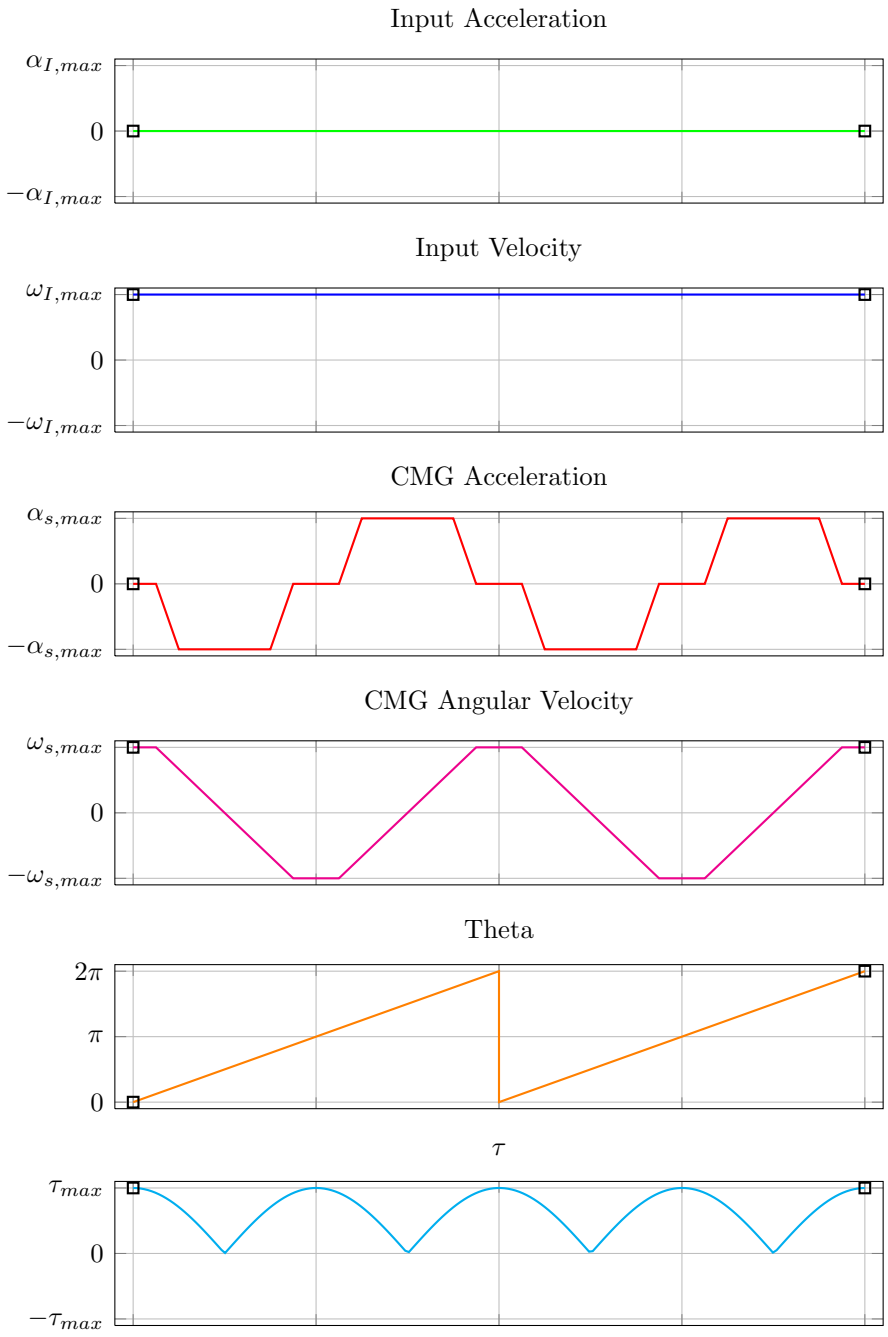

Figure 3.14: This figure shows the non-ideal (realistic) behavior of the Λ^2 oscillation state shown in figure 2.16. This behavior incorporates the ramp up and ramp down time for α_s and ω_s

The the x-axis of figure 3.14 is time independent. The timing depends on both ω_g and τ_r (the torque fo the rotor motor). The total time it takes for one full cycle of the system will be described t_E, or the event time. In other words this means that θ_g will

traverse 2π radians. For computational purposes, one half of the event time, or the time it takes θ_g to traverse from 0 to π, will be described as t_e. Figure 3.15 shows how the time scale is effected by ω_g and τ_r. Using this figure as a reference, we can calculate the t_E and τ_r.

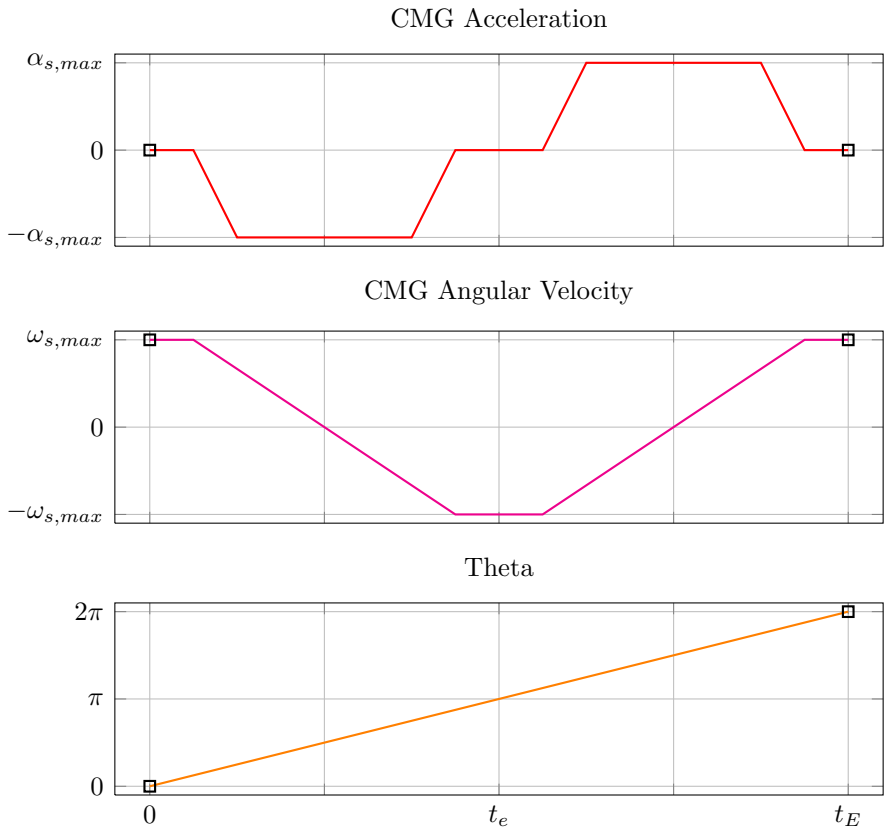

Figure 3.15: This figure is an isolated view of 3.14 showing the parameters of the CMG motor and how they directly effect the timing of the DSP-VSCMG system.

Using the standard equation for rotational velocity, we can deduce

$$\omega_g t_e = \theta_g \tag{3.31a}$$

$$t_e = \frac{\pi}{\omega_g} \tag{3.31b}$$

or

$$t_E = \frac{2\pi}{\omega_g} \tag{3.31c}$$

when the system is the in the Δ^2 steady state. This will be the minimum value for t_E since the system will be oscillating at its fastest speed. We also know

$$\tau_r = I_r \alpha_r \tag{3.32a}$$

$$\frac{\tau_r}{I_r} = \alpha_r \tag{3.32b}$$

Examining figure 3.15 we can see that 1 total oscillation of the system can be broken into 2 different events. The state of the system from π to 2π is the same state of the system from 0 to π with the polarities reversed. Mechanically speaking, this means that the motors will just be spinning in the opposite direction. For calculation purposes, we can examine the system from π to 2π to ease calculations. Doing so, we can find the torque needed for the input motors of the system.

$$\omega_f = \omega_o + \alpha t_e \tag{3.33a}$$

$$\omega_{r,max} = -\omega_{r,max} + \alpha_r t_e \tag{3.33b}$$

$$2\omega_{s,max} = \alpha_r t_e \tag{3.33c}$$

Substituting in equation (3.31b) and (3.32b) yields

$$2\omega_{s,max} = \frac{\tau_r}{I_r}\frac{\pi}{\omega_g} \tag{3.33d}$$

or

$$\frac{2\omega_r \omega_g I_r}{\pi} = \tau_r \tag{3.33e}$$

3.13 Process for Parametric Analysis

Following the modeling flow chart will allow a barycenter offset type of system to be compared to a CMG type of system. The flow chart is shown in Figure 3.16. The output of the flowchart will be different models of the barycenter offset and conservation of angular momentum type of spherical robots.

The first step is to determine the size of the outer shell. This constraint will be set

against all models, and will allow us to compare the power that can be contained inside a fixed volume. The next step will be to design rough physical models in CAD. The CAD software will allow us to calculate parameters that would otherwise be difficult to calculate: inertia, mass, etc. Once the that is done, we can then calculate final characteristics of each of barycenter offset and CMG design.

The barycenter offset designs can consist of any bob size, but the results in the following chapter will focus on 35% and 25% the size of R_{shell}. A bob size of 25% would be an ideal embodiment of a barycenter offset design, and a bob size of 35% represents a realistic embodiment that is seen in practice. Due to the equations defined throughout this document, the peak torque, average torque, weight, velocity curves, acceleration curves, and maximum incline for each barycenter offset embodiment can be calculated without the use of simulation. We can use these values to see how these designs compare to the COAM designs.

For the SP-VSCMG and Dual SP-VSCMG designs, we will first have to determine the bounding sphere of each. We can then choose a CMG geometry that will maximize the inertia. From that, the physical models can be created. With simulation, we can then calculate the same parameters as the barycenter offset design for comparison. However ω_r, α_r,ω_g, and α_g are subject to interpretation. This is due to the fact that these values will be based on the type of motor selected in the design. For these parameters, we will select fair values that are achievable with current technology.

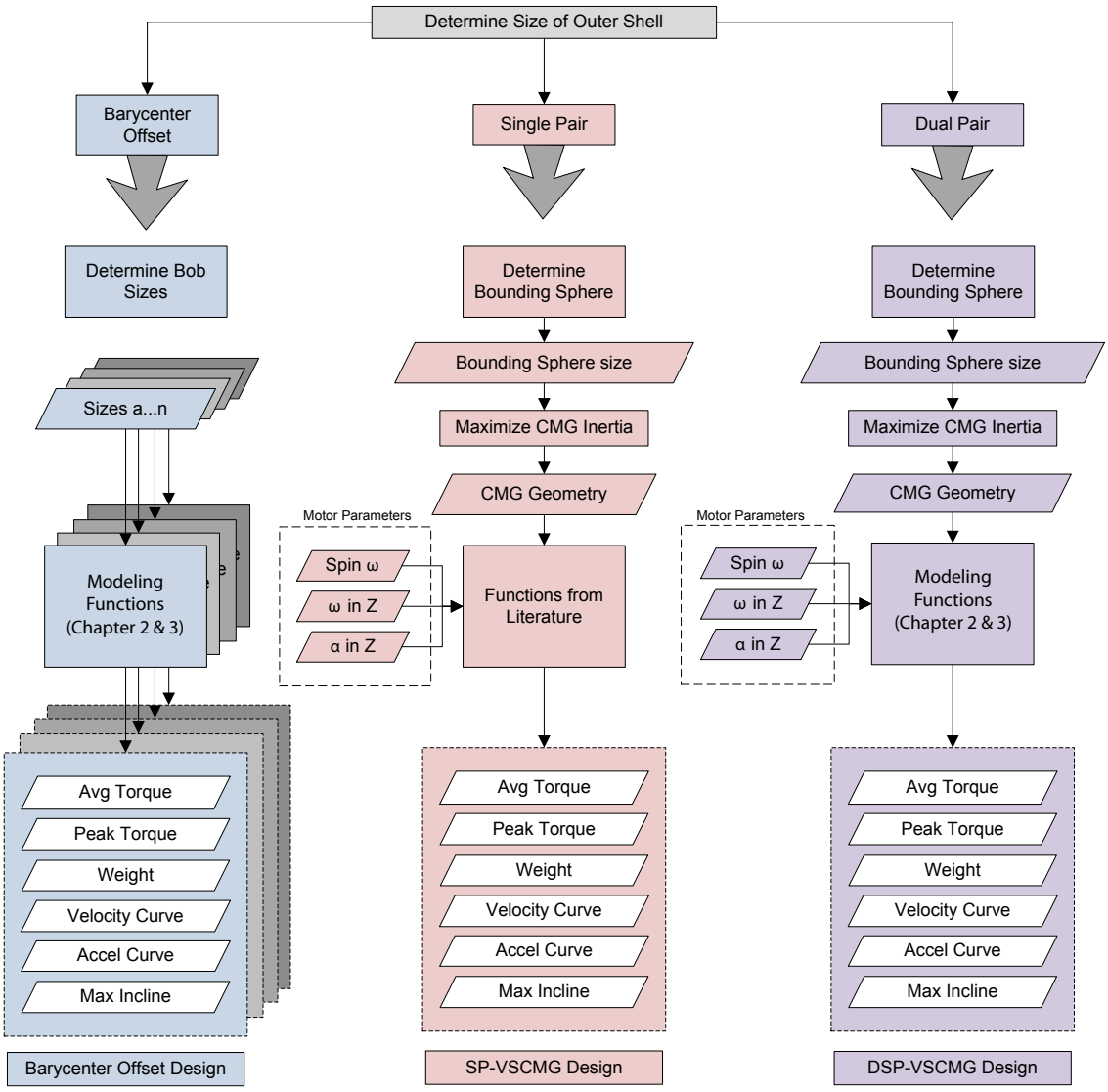

Figure 3.16: Organizational flowchart of parametric analysis

3.14 Summary

In this chapter the key elements to perform a proper modeling simulation were discussed and derived. A general overview of how a barycenter offset, SP-VSCMG, and DSP-VSCMG system was discussed. Output power was also modeled for each system as seen from the output motor (equation 3.1). The power was also described in terms of parameters of the robot (equation 3.6). Also, the equation for the translational velocity (equation 3.11) was also described. An important factor in comparing cross platform designs, inclined planes (equation 3.13f) and maximum step size (3.20), were described.

Some analysis parameters of the design were also discussed. The volume of the robot relates to the size of the outer shell, the weight, and the internal mechanics. With the modeling parameters and functions described, the next chapter will describe the performance characteristics of the three robot designs, parametric analysis of the individual designs, and how varying single parameters can effect the performance of the robot as a whole.

Chapter 4: Comparison and Results of Spherical Robot Designs

Chapter Abstract

With the theory and operating equations of both barycenter offset and CMG based spherical robots described in previous sections, the next step is to analyze the derived equations and determine how varying parameters will effect the each system. This research seeks to determine how a CMG based design compares to a barycenter offset design. Although this research does not exhaust all possible configurations of a CMG based robot, the examples shown are indicative of how a CMG based design can be enhanced to perform as well as or better than a barycenter offset based design. As with the design of any robotic or vehicular system, the designer must first determine what type of conditions the vehicle or robot will operate it. Should the car be able to traverse potholes greater than one meter in diameter? If so, then the tires should be large enough so they do not become stuck in the hole. Similar rules apply to a spherical robot. If the robot is to be able to drive over a one meter hole, it must be larger enough and have enough power to climb out of the hole.

4.1 Introduction

In this section, the equations discussed in the previous chapters will be used to compute initial physical models of barycenter offset and CMG based designs. In the following sections, single parameters of the robot will be varied in order to determine the effects on the system as whole. Outer shell size, mass, output motor RPM, CMG speeds and geometries will be examined to determine the effects on robot incline, step size, power usage, and speed. From the graphs created, the performance between the VSCMG models and the barycenter offset models can be compared. The CMG based models will be compared to a barycenter offset model with a bob radius of 33% that of the outer shell, which is an informed estimate based on current designs. An illustration of these models was presented in Figure 4.1. A SP-VSCMG model consists of a single scissored pair, and a DSP-VSCMG consists of two scissored-pairs. Conclusions between the two models will also be discussed, as well as alternative design considerations.

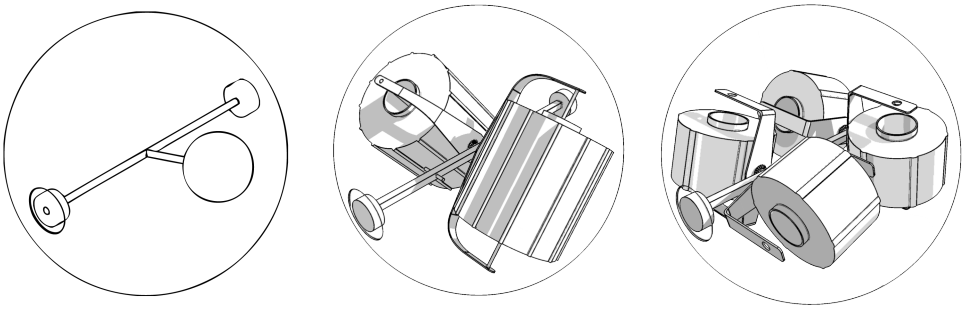

Figure 4.1: Photo of a barycenter offset, SP-VSCMG, and DSP-VSCMG spherical robot model

4.2 Initial Results

In order to make a proper comparison between each uniquely functioning designs, as many design parameters as possible must be kept the same in order to avoid confounding the results. The first set of design parameters that will be set are the geometric constraints (shown in table 4.1), which determine the size and space claim of the robot. The variables are as follows: v_{max} is the maximum translational velocity of the ball, r_{shell} is the radius of the outer shell, r_{thick} is the thickness of the outer shell, m_{shell} is the thickness of the

outer shell, ρ_{shell} is the average density of the shell, ρ_{bob} and ρ_{rotor} are the average densities of the bob and rotor, respectively, and r_r/r_{bound} is the size of the rotor radius divided by the bounding sphere radius. These are the geometric properties that are universal to each design. Properties such as rotor size are specific to CMG based designs and will be investigated during the appropriate section. The initial geometric constraints were chosen by examining real world designs and estimating realistic criteria for the robot to meet: a top speed of 5.36mph, a shell made of carbon fiber, a bob and CMGs made of brass, etc.

Table 4.1: Initial Geometric Constraints

v_{max} (mph)	r_{shell} (m)	r_{thick} (m)	m_{shell} (kg)	ρ_{shell} (kg/m^3)	ρ_{bob} (kg/m^3)	ρ_{rotor} (kg/m^3)	r_r/r_{bound} (-)
5.36	.1143	.043	1.217	1790	8470	8470	.88

Additionally, design constraints are set for initial evaluation. These constraints are based on educated assumptions of existing technology that would be feasible to integrate into a spherical robot. The design constraints shown in 4.2 are defined as follows: $\tau_{r,max}$, the maximum torque of the rotor motor; $\omega_{r,max}$, the maximum rotational velocity of the rotor; $\tau_{g,max}$, the maximum torque of the gimbal motor; $\omega_{g,max}$, the maximum rotational velocity of the gimbal; $\tau_{o,max}$, the maximum torque of the gimbal motor; $\omega_{o,max}$,the maximum rotational velocity of the output motor; *deadband*, the number of radians that the rotors are accelerating or decelerating (when ω_r is not at maximum); *offset*, the phase between each scissored pair system of a dual scissored pair; and r_{bob}/r_{shell}, the radius of the bob in terms of the percentage of the radius of the outer shell.

Table 4.2: Initial Design Constraints

$\tau_{r,max}$ $(N \cdot m)$	$\omega_{r,max}$ (rpm)	$\tau_{g,max}$ $(N \cdot m)$	$\omega_{g,max}$ (rpm)	$\tau_{o,max}$ $(N \cdot m)$	$\omega_{o,max}$ (rpm)	*deadband* (deg)	*offset* (deg)	r_{bob}/r_{shell} (-)
1	1000	1	60	1	200	180	90	.33

With the geometric and design constraints set, an initial cross platform comparison can be made which is shown in table 4.3. Three designs are compared across six categories.

The three designs are a base barycenter offset design, an ideal scissored-pair design, and an ideal dual scissored-pair design. The ideal scissored pair designs reflect the best results that can be achieved, whereas the non-ideal reflect the worst results. In these initial results, only the steady state ideal cases are examined, but the steady state non-ideal cases will be discussed at the end of this chapter. The main difference between ideal and non-ideal system is the incorporation of the torque generated from the acceleration and deceleration of the rotor as discussed in equation 2.28. The six categories of evaluation are the total mass (m_{net}), the average incline (ϕ_{inc}), step size from rest (h_{step}), the power used per 2π cycle (P_{cycle}), the average torque generated (τ_{avg}), and the peak torque generated (τ_{peak}). Finally, the relationship of $\phi_{inc}/P_{cycle}$is also examined. This correlates to the cost in power per degree of incline a system will use over one cycle of steady state operation.

Table 4.3: Initial Performance Characteristics

	m_{net} (kg)	ϕ_{inc} (deg)	h_{step} (m)	P_{cycle} $(W/cycle)$	τ_{avg} $(N \cdot m)$	τ_{peak} $(N \cdot m)$	ϕ_{inc}/P_{cycle} (deg/W)
Barycenter	3.12	24.13	0.0100	33.25	1.43	1.43	0.73
SP (ideal)	8.52	23.92	0.0098	225.43	3.87	6.08	0.11
DSP (ideal)	9.53	16.45	0.0047	217.39	3.02	4.75	0.08

From the initial results, the barycenter offset design outperforms all of the CMG based designs. However, a SP design with an ideal control system performs realitively similar to a barycenter design although it does use more power. It also noticeable that as the complexity of the design increases, the power cost per degree also increases. With the initial results set up, we can examine enhancing the CMG based designs in order to outperform the barycenter offset design. However, with enhancements and experimentation it will be possible to improve the performance of the CMG based designs.

4.3 Rotor Size

For the first enhancement, we will look at adjusting the rotor size. The rotor geometry effects the total mass of the robot, as well as the torque output and power draw. Figure 4.2 shows the effects of adjusting r_{rotor}/r_{bound} on the average incline and power draw per cycle of a SP-VSCMG system. From the graph we can see that when r_{rotor}/r_{bound} is

equal to 0.96, the incline is maximized. Furthermore, the power draw is far less than its potential maximum. Recomputing the performance characteristics with the new rotor width yields the results shown in table 4.4 along with the corresponding differences from the previous iteration. We can see the total power on a SP-VSCMG system was decreased by $31.1W$ and $24.26W$ for a DSP-VSCMG system. Furthermore, the inclines increased $3.13deg$ and $2.18deg$ for a SP-VSCMG and DSP-VSCMG system, respectively. For future calculations, the r_{rotor}/r_{bound} value used will be 0.96.

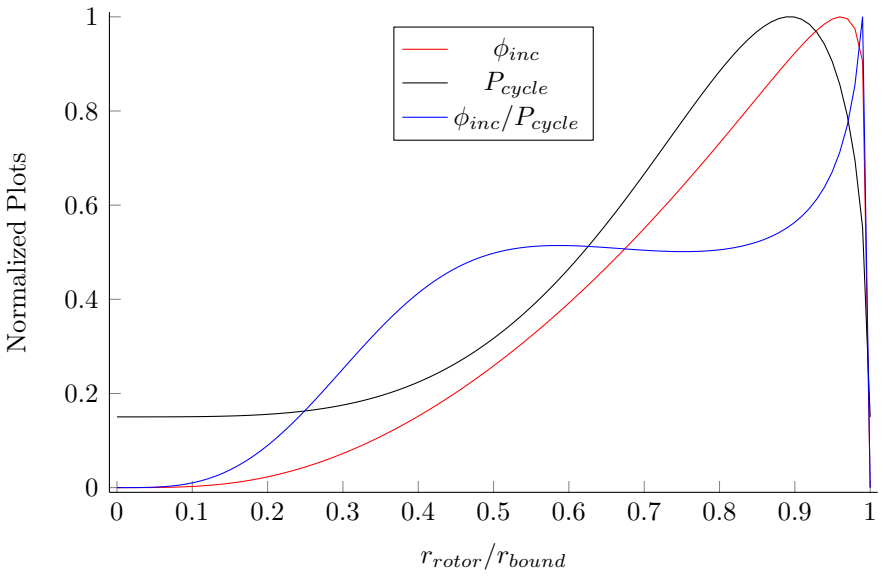

Figure 4.2: Plot showing the effects of adjusting r_{rotor}/r_{bound} on the average incline and power per cycle of a SP-VSCMG configuration

Table 4.4: Performance Characteristics and Δ's from r_{rotor} adjustment

	m_{net} (kg)	ϕ_{inc} (deg)	h_{step} (m)	P_{cycle} $(W/cycle)$	τ_{avg} $(N \cdot m)$	τ_{peak} $(N \cdot m)$	ϕ_{inc}/P_{cycle} (deg/W)
Barycenter	3.12	24.13	0.0100	33.25	1.43	1.43	0.73
SP (ideal)	6.36	27.05	0.0125	194.35	3.24	5.09	0.14
DSP (ideal)	7.07	18.63	0.0060	193.13	2.53	3.97	0.10
	Δm_{net} (kg)	$\Delta\phi_{inc}$ (deg)	Δh_{step} (m)	ΔP_{cycle} $(W/cycle)$	$\Delta\tau_{avg}$ $(N \cdot m)$	$\Delta\tau_{peak}$ $(N \cdot m)$	$\Delta\phi_{inc}/P_{cycle}$ (deg/W)
Barycenter	0	0	0	0	0	0	0
SP (ideal)	-2.16	3.13	0.0027	-31.08	-0.63	-0.99	0.03
DSP (ideal)	-2.46	2.18	0.0013	-24.26	-0.49	-0.78	0.02

4.4 Trade Off Between ω_r and ω_g

An additional enhancement to be examined is the trade off between ω_r and ω_g. The magnitude of the output torque is based on a scalar factor of

$$2I_r\omega_{r,max}\omega_g \tag{4.1}$$

as shown in equation 2.43. The power used per cycle is the power used by the output motor (equation 3.1) plus the power used to spin the rotors up and down (equation 3.10) plus the average gimbal motor power which is

$$\tau_o\omega_{o,avg} + 2I_r\omega_r^2\left(\frac{\omega_g}{2\pi}\right) + 2\tau_g\omega_{g,avg} \tag{4.2}$$

From these two equations, we can see that the magnitude of the output torque is a linear relationship, while the power draw is a squared relationship. The correlation between ω_g and ω_r is shown in figure 4.3. The magnitude of the torque was kept the same while the gimbal rate (x-axis) was increased. Accordingly, the rotor rate was adjusted to keep $\tau_{o,avg}$ the same magnitude. For a single scissored pair, We can see that as the gimbal rate increases, the power per cycle increases as well. However, as the gimbal rate approaches zero, the power also increases, meaning that there is a local minimum. Searching for the local minimum shows that the power is improved when $\omega_r = 638rpm$ and $\omega_g = 94rpm$. The performance characteristics with these values as inputs are show in table 4.5.

Table 4.5: Performance Characteristics with w_g adjustment, single pair as baseline

	m_{net} (kg)	ϕ_{inc} (deg)	h_{step} (m)	P_{cycle} $(W/cycle)$	τ_{avg} $(N\cdot m)$	τ_{peak} $(N\cdot m)$	ϕ_{inc}/P_{cycle} (deg/W)
Barycenter	3.12	24.13	0.0100	33.25	1.43	1.43	0.73
SP (ideal)	6.34	27.06	0.0125	182.52	3.23	5.08	0.15
DSP (ideal)	7.05	18.64	0.0060	207.37	2.52	3.96	0.09

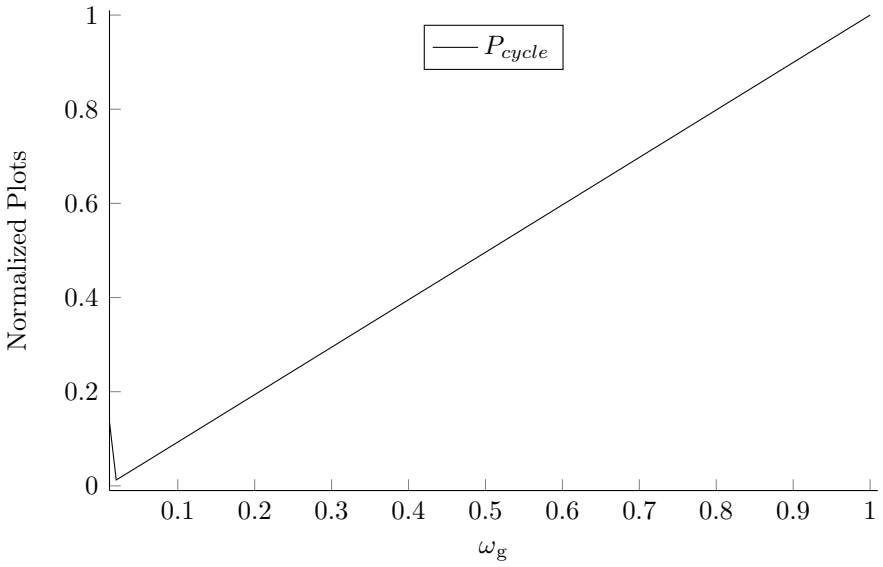

Figure 4.3: Plot showing the effects of adjusting ω_g and ω_r while keeping the same value of $\tau_{o,avg}$ for a SP-VSCMG configuration. Local minimum may disappear with different design constraints

The table illustrates that power for single scissored-pair system decreases $11.83 W/cycle$ whereas the dual scissored-pair increases $14.24 W/cycle$. The addition of the two extra gimbal and rotor motors changes the local minimum of figure 4.3 when tested with a dual scissored pair. The resulting values of ω_r and ω_g are $1035 rpm$ and $58 rpm$, respectively. Plugging in these speeds for a dual scissored-pair only yields the performance characteristics shown in table 4.6. The performance Δ's after adjusting ω_g and ω_r are showin in table 4.7.

Table 4.6: Individually Optmized ω_r and ω_g for each design, separate baseline

	m_{net} (kg)	ϕ_{inc} (deg)	h_{step} (m)	P_{cycle} $(W/cycle)$	τ_{avg} $(N \cdot m)$	τ_{peak} $(N \cdot m)$	ϕ_{inc}/P_{cycle} (deg/W)
Barycenter	3.12	24.13	0.0100	33.25	1.43	1.43	0.73
SP (ideal)	6.34	27.06	0.0125	182.52	3.23	5.08	0.15
DSP (ideal)	7.05	18.65	0.0060	192.83	2.52	3.96	0.10

Table 4.7: Δ's after ω_r and ω_g adjustments

	Δm_{net} (kg)	$\Delta \phi_{inc}$ (deg)	Δh_{step} (m)	ΔP_{cycle} $(W/cycle)$	$\Delta \tau_{avg}$ $(N \cdot m)$	$\Delta \tau_{peak}$ $(N \cdot m)$	$\Delta \phi_{inc}/P_{cycle}$ (deg/W)
Barycenter	0	0	0	0	0	0	0
SP (ideal)	0	0	0	-11.83	0	0	0.01
DSP (ideal)	0	0	0	0.30	0	0	0

4.5 Material Density

An important parameter to consider is material density, specifically the material that the bobs are made of and the material that the CMGs are made from. Three plots are presented in figure 4.4 with a varying value of ρ for a barycenter offset, scissored-pair, and dual scissored-pair system. Each plot shows the total mass of system, the average angle of inclination, and the angle of inclination per watt for a bob. The graphs show three key results. The first and most obvious is that as the density of the material increases, the mass of the system increases. The second is that as the density increases, the average angle of inclination increases. The third, and most important fact is that for CMG based designs, as the density increases, there exists a point where the power cost per degree of incline begins to decrease. This means that after this point, increases the density of the material makes the system less efficient.

Taking into account this key fact, the density of the CMGs was decreased to the $2700 kg/m^3$, the density of aluminum. Although the most efficient density is around $2700 kg/m^3$, aluminum was chosen because it is the closest, readily available material to the best density. Doing this means that the CMG designs are operating in the area where the effect of the weight on the system is most efficient. In general, decreasing the weight results in a lower average angle of inclination. However, the speed of the rotors ω_r can be increased without a gain in power draw because the efficiency has been increased. Changing the density of the CMG material to aluminum and increasing the rotor speed to $1425 rpm$ from $1035 rpm$ yields the performance characteristics shown in table 4.8. The Δ's from the last iteration to this one are shown in table 4.9.

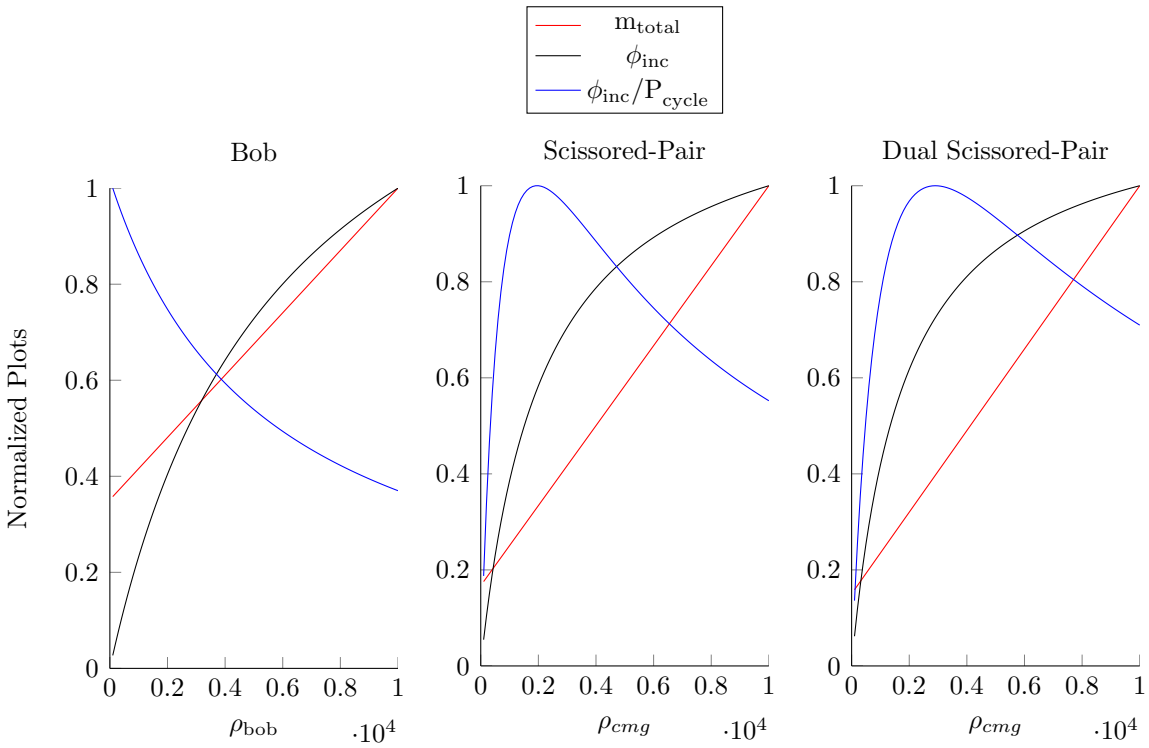

Figure 4.4: Plots showing the effects of adjusting ρ_{bob} and ρ_{cmg}

Table 4.8: Performance Characteristics with ρ adjustment

	m_{net} (kg)	ϕ_{inc} (deg)	h_{step} (m)	P_{cycle} $(W/cycle)$	τ_{avg} $(N \cdot m)$	τ_{peak} $(N \cdot m)$	ϕ_{inc}/P_{cycle} (deg/W)
Barycenter	3.12	24.13	0.0100	33.25	1.43	1.43	0.73
SP (ideal)	2.85	27.37	0.0128	122.94	1.47	2.31	0.22
DSP (ideal)	3.07	19.43	0.0065	137.40	1.15	1.80	0.14

Table 4.9: Performance Δ's after ρ adjustment

	m_{net} (kg)	ϕ_{inc} (deg)	h_{step} (m)	P_{cycle} $(W/cycle)$	τ_{avg} $(N \cdot m)$	τ_{peak} $(N \cdot m)$	ϕ_{inc}/P_{cycle} (deg/W)
Barycenter	0	0	0	0	0	0	0
SP (ideal)	-3.49	0.31	0.0003	-59.58	-1.76	-2.77	0.07
DSP (ideal)	-3.98	0.78	0.0005	-55.43	-1.37	-2.16	0.04

4.6 Conclusions and Results of Parametric Analysis

From these experiments, we can draw the following conclusions and comparisons between the three models. For the barycenter offset model, an incline greater than $30 degrees$ is hard to achieve, and as a the density of the bob goes up, the power efficiency goes down. For a single scissored-pair design, it is more probable to achieve average angles of inclination above $30 degrees$ by simply adjust the average rotor velocity, ω_r but at a significant power cost. However, the output torque will always have conditions that may result in a zero output. Like a single pair design, a dual pair scissored-pair design will be able to achieve average angles of inclination above $30 degrees$ by adjusting ω_r. However, a dual-pair CMG system can be designed to have a continuous, non-zero output torque.

Fortunately, the CMG based designs can be modified to significantly reduce power consumption at no cost to speed, agility, and average incline. Enhanced geometric and design constraints deducted from the previous sections are show in tables 4.10, 4.11, and 4.12. The enhanced performance characteristics are shown in table 4.13. Table 4.14 shows the effects of the optmization techniques on the initial performance characteristics. The table shows that the total mass and power draw of both scissored-pair systems were decreased, while the average incline increased.

Table 4.10: Optimized Geometric Constraints

v_{max} (mph)	r_{shell} (m)	r_{thick} (m)	m_{shell} (kg)	ρ_{shell} (kg/m^3)	ρ_{bob} (kg/m^3)	ρ_{rotor} (kg/m^3)	r_{bob}/r_{shell} (-)
5.36	.1143	.043	1.217	1790	8470	2700	.33

Table 4.11: Optimized Design Constraints (Single Pair - Ideal)

$\omega_{r,max}$ (rpm)	$\omega_{g,max}$ (rpm)	$\tau_{o,avg}$ $(N \cdot m)$	$\omega_{o,max}$ (rpm)	$deadband$ (deg)	$offset$ (deg)	r_r/r_{bound} (-)
1090	78	3.23	200	0	-	.96

Table 4.12: Optimized Design Constraints (Dual Pair - Ideal)

$\omega_{r,max}$ (rpm)	$\omega_{g,max}$ (rpm)	$\tau_{o,avg}$ $(N \cdot m)$	$\omega_{o,max}$ (rpm)	$deadband$ (deg)	$offset$ (deg)	r_r/r_{bound} (-)
1934	44	2.52	200	0	90	.96

Table 4.13: Optimized Performance Characteristics

	m_{net} (kg)	ϕ_{inc} (deg)	h_{step} (m)	P_{cycle} $(W/cycle)$	τ_{avg} $(N \cdot m)$	τ_{peak} $(N \cdot m)$	ϕ_{inc}/P_{cycle} (deg/W)
Barycenter	3.12	24.13	0.0100	33.25	1.43	1.43	0.73
SP (ideal)	2.85	27.37	0.0128	120.51	1.47	2.31	0.23
DSP (ideal)	3.07	19.43	0.0065	134.78	1.15	1.80	0.14

Table 4.14: Δ Performance Characteristics

	m_{net} (kg)	ϕ_{inc} (deg)	h_{step} (m)	P_{cycle} $(W/cycle)$	τ_{avg} $(N \cdot m)$	τ_{peak} $(N \cdot m)$	ϕ_{inc}/P_{cycle} (deg/W)
Barycenter	0	0	0	0	0	0	0
SP (ideal)	-5.67	3.45	0.003	-105.43	-2.4	-3.77	0.12
DSP (ideal)	-6.46	2.98	0.018	-82.61	-1.87	-2.95	0.06

4.7 Consideration of Shell Size

A consideration to take into account is the size of the robot itself. Figure 4.5 shows a normalized plot for each type of design, with a shell radius, r_{shell}, varying from 0 to 1 meter. Each plot was created by employing the same design logic as described previously in this document but varying r_{shell}. The internal components are scaled proportionately with increase in the shell size. The data from these simulations reflects two interesting facts. First, is that regardless of the shell radius, the barycenter offset system's angle of inclination remains the same, whereas both CMG based designs have a greater average angle of inclination as the shell size is increased. This shows that as the size of the robot increases, the gyroscopic effects are more dominant than a pendulum's effect. The second fact is that a barycenter offset's power cost per angle of inclination continues to decreases as shell size increases, whereas both CMG based designs have a local maximum around $15cm$.

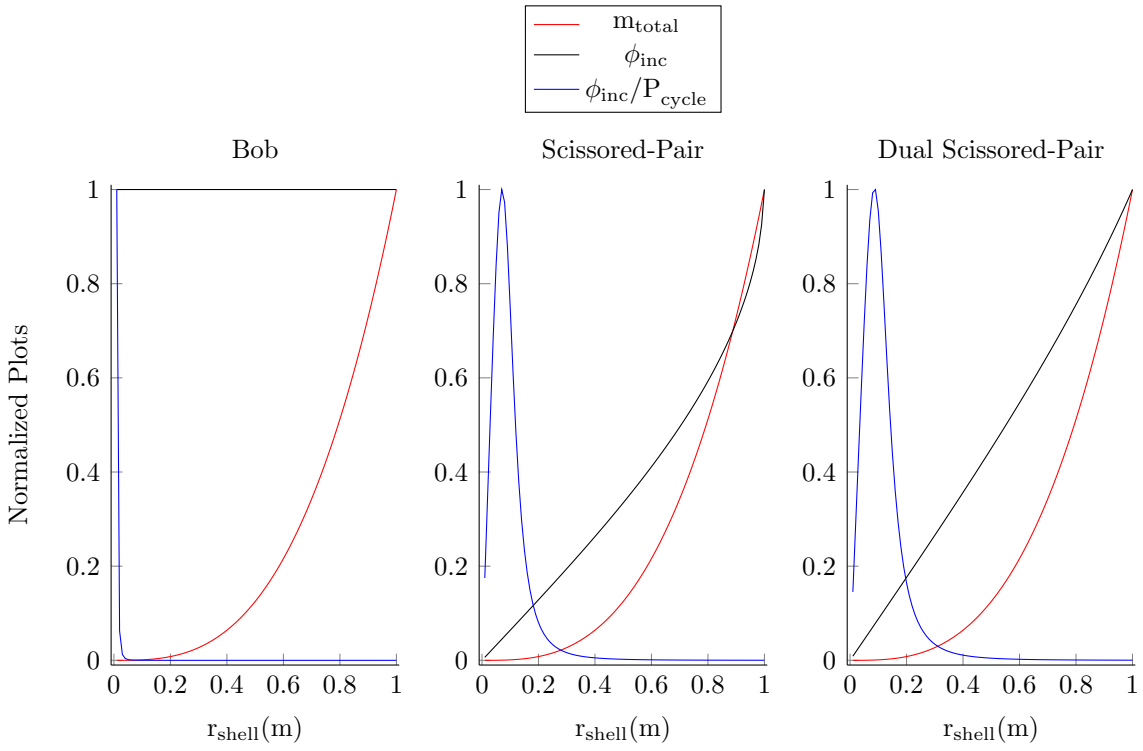

Figure 4.5: Plots showing the effects of adjusting r_{shell}

We can also look at non-normalized plots of the angle of inclination and the power

draw for each of the three models. The previous plots give information related to efficiency which helps to enhance the design, whereas a non-normalized plot will help in designing a system to specification. Figure 4.6 shows how the average incline for CMG based designs increases significantly compared to a barycenter offset design, again showing that the gyroscopic effects become dominant at larger scales. Also, figure 4.7 shows the power draw for CMG designs is significantly larger than a barycenter offset design. So although CMG based designs can traverse steeper incline, they are equally or less efficient than barycenter offset models.

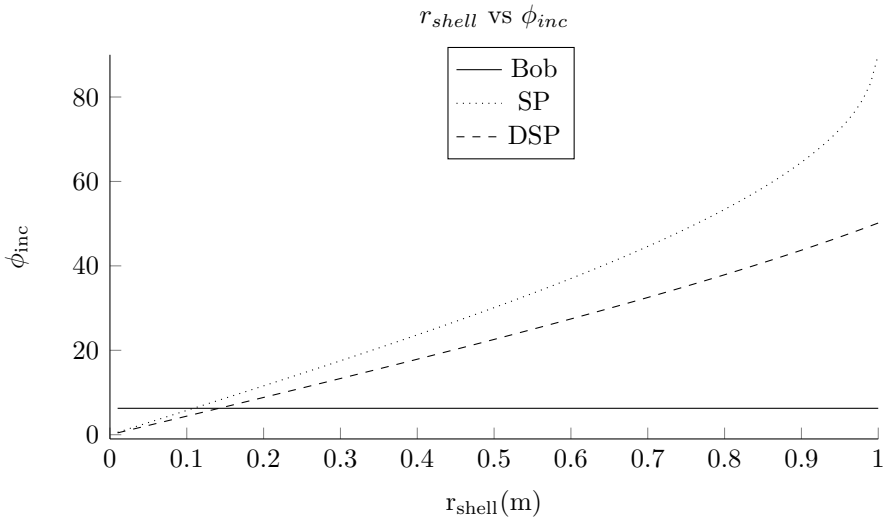

Figure 4.6: Plots showing the effects of adjusting r_{shell} on ϕ_{inc}

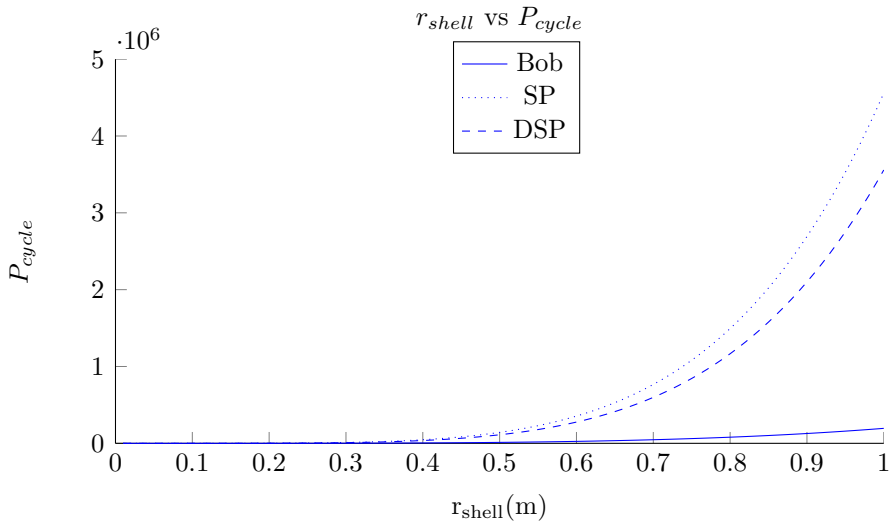

Figure 4.7: Plots showing the effects of adjusting r_{shell} on P_{cycle}

4.8 Effects of Non-Ideal Scenarios

As previously mentioned, the results obtained are of an ideal scenario; the rotor speed can instantaneously switch between $-\omega_r$ and $+\omega_r$ without accelerating. Recall that the output torque for a single scissored pair is

$$\tau_{sp} = 2I_R\omega_g\omega_r cos\theta_g \tag{2.30}$$

The non-ideal output torque introduces a $\sin\theta_g$ term to the equation which comes from the acceleration and deceleration from the rotors - the changing value of ω_r, α_r.

$$\tau_{sp} = 2I_r\omega_{r,max}\omega_g \left\{ \frac{\sin\theta_g}{\pi}u(t) + \frac{cos\theta_g}{2} \right\} \hat{\mathbf{e}}_3^{(1)} \tag{2.43}$$

The theory of this phenomenon is discussed in Section 2.10. Its effect on the results are entirely dependent on the control system. For example, if the ω_g is relatively small, the effect from α_r will be small. One method of this would be to halt the scissored-pair gimbals while the rotors are getting up to speed. In other words, ω_g would be equal to zero when α_r would be high, resulting in a 0 value of the output torque. In a dual scissored-pair setup, the second scissored pair could be generating torque while the first

scissored pair is reconfiguring itself resulting in a continuous non-zero output.

Another solution to negating the effects of the α_r would be to develop a dynamic control system that satisfies all design equations simultaneously. The control signals would be similar to those shown in figure 3.14. However, the zero crossing of the output torque function would change in real time due to the changing acceleration as shown in equation 2.40. This would result in a more complicated control system than discussed in this document, but the base theory for developing a control system would be the same.

4.9 Design Considerations

Although a DSP-VSCMG design may outperform a barycenter offset design in terms of agility and maximum incline, building such a platform is not trivial. A few techniques for achieving an enhanced DSP-VSCMG design are discussed below. In practice, the motor to spin the CMG is placed next to the CMG itself, as shown in figure 4.8. However, an enhanced design would incorporate the motor on the inside of the gyro, as shown in figure 4.8. This will mean that each CMG module is balanced, and will not have an off-axis weight. Further, the outer shell of the motor will also add to the I_s value.

(a) Offset motor with counterbalance (b) Internal motor

Figure 4.8: Two concepts for attaching a CMG Motor

Another consideration is to use one motor to control θ_g. The design in this document eludes to one input motor per CMG module. However, by connecting the motors together through gears and setting their initial positions appropriately, θ_g can be controlled by one motor. However, because the initial positions of the CMGs are mechanically set, this may limit how the DSP-VSCMG system will oscillate. For example, if the system is set

to oscillate in the Δ state (Figure 2.16), the system may have to be physically changed to operate in a different steady state.

Battery integration is obviously important to the design. There are two ways to integrate a power system into the robot. A simple way would be to add a battery hanging off the center axis. This would mean the battery would act as a bob, just like in a barycenter offset model as shown in figure 4.9. This would mean that the system would be a hybrid barycenter offset DSP-VSCMG design and come with appropriate benefits and short comings: outputs more torque but uses more power, etc. An alternate method would be to integrate the battery into the center rod, as shown in figure 4.9. This would be a good equi-weight distribution design, as well as make the mechanics slightly less difficult without having the added pendulum.

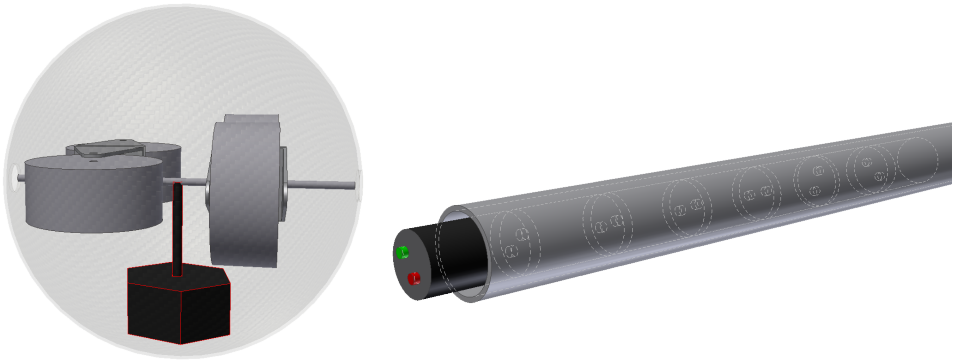

(a) Bob-style power source (b) Embedded power source

Figure 4.9: Two concepts for mounting a power source

4.10 Conclusions Between Models

The main goal of this work is to determine if a CMG based design can out perform a barycenter offset design. The answer is yes, but not without cost. A barycenter offset spherical robot has its advantages. It is a relatively simple design, with a relatively simple control algorithm. As discussed in Chapter 1, there are many different methods for designing a barycenter offset system, each with its own benefits and characteristics. However, because of the mechanical constraints of the system, the design has fundamental limitations: its center of gravity can never be outside of the shell, and thus, can not climb

step inclines/slopes.

The CMG based robot design discussed in this entire document, is a new type of design who's limitations are based on technological, not physical, constraints. However, the design is much more complicated than a barycenter offset system, as are the controls. In this chapter, it is shown that with with proper parametric analysis and design, a DSP-VSCMG system should be able to outperform a barycenter offset system, but a DSP-VSCMG system needs more power to do so.

Although a CMG based design requires more energy in a continuous steady state, there are methods to enhance the overall performance. CMG motor speed, construction materials, and even the control system take part in the efficiency of the system, and thus how much power is needed to operate it. A spherical robot will require a certain amount of energy to traverse up an incline. If a barycenter system can not provide enough power to traverse up the incline, a DSP-VSCMG system will be able to provide enough power without having to change the overall dimensions of the robot. In essence, a DSP-VSCMG design can pack more power inside the shell than a barycenter offset design.

4.11 Future Work

The next action of this research would be to further develop a physical prototype of a scissored-pair system. A physical system could then be checked against the equations discussed in this literature to further validate the underlying mathematics and dynamics. Construction of a physical system will also give insight into other mechanical design options, such as replacing motors with a system of gears in order to save power.

Another area of research stemming from this investigation would be the development of a dynamic control system. This document explains the basis for controlling a SP-VSCMG system, however, the control signals used in the results are determined before the computations. In this basic control scenario, the rotors and gimbals are positioned in such a manner that the system can enter a steady state easily. However, in a physical prototype, a dynamic control system should be developed so that the system can enter a steady state when the initial conditions are random, and not predetermined.

Finally, a database of parts could be integrated into the simulation in order to have a fully automated parametric analysis. In the scenarios discussed in this document, we had the luxury of selecting any type of motor that was needed: low power, high torque, for example. In practice, these numbers will be much less flexible and will be determined by what items are commercially available. A parts list database could be checked during parametric analysis so that the final resulting model would incorporate real components. Another topic that must be investigated are controls in realistic scenarios and how to subdue unwanted oscillations in the that may occur in the $\hat{\mathbf{e}}_2^{(1)}$ and $\hat{\mathbf{e}}_1^{(1)}$ directions.

4.12 Thesis Summary

Chapter one reviewed the current state of the art of spherical robotics. The review looked over barycenter offset, shell transformation, and conservation of angular momentum based designs. Barycenter offset model types consisted of hamster ball, IDU, pendulum driven, double pendulum driven, shifting weights, and some notable enhancements on each of these. Shell transformation designs discussed consisted of pressurized air bladders and shape memory alloys. Conservation of angular momentum designs discussed consisted of balancing robots, uni-dimensional conservation of angular momentum, and tri-dimensional conservation of angular momentum. Lastly, added gyroscopic scissored pairs as a momentary boost to a barycenter offset design was discussed.

Next, in chapter two, the theory of the scissored pair was discussed from first principles. The fundamental limitations of how much power could be transferred from the inner mechanics to the outer shell of the robot was discussed. Following that, a brief review of the physics of a control moment gyroscope was discussed which lead into the derivation of key equations that drive the behavior and performance of the robot. Once the key equation for the output torque of the robot was described, the nature of the equation was examined through mathematics. This included, when to change the polarity of the CMG spin, evaluating potential and average torque output levels. Also discussed were metrics of the scissored pair behavior such as how long was the torque output below / above average, periods of oscillation, and maximum angular velocity of the CMGs. Finally,

dual configurations of scissored-pairs were discussed and evaluated with these metrics.

With the theory of the scissored pair evaluated, chapter three discussed modeling and parametric analysis techniques of the robot. First, the key elements to model were discussed along with the three types of models: barycenter offset, SP-VSCMG, and DSP-VSCMG. Modeling of the power consumption was examined at a general and fine scale. Also discussed was the modeling of the translational velocity, translational acceleration, maximum ability to climb up an incline planed, and maximum step size from rest. Also examined was how to better utilized the available volume of the robot by mathematically determining CMG geometry. Finally the process for designing the robot was overviewed, followed by a table comparing model parameters of the three different types of spherical robots.

The final chapter examined the effects on the robot when various parameters were changed: shell size, rotor speed, material density, and various power trade offs. The effects of the changing parameters were also shown on the robot designs head to head. The results showed that CMG based designs can outperform barycenter offset designs, but require more power to do so. The document finished with a conclusion between the models, future work, and a few alternative designs.

BIBLIOGRAPHY

[1] A. Halme, T. Schonberg, and Y. Wang, "Motion control of a spherical mobile robot," in Advanced Motion Control, 1996. AMC'96-MIE. Proceedings., 1996 4th International Workshop on, vol. 1, pp. 259–264, IEEE, 1996.

[2] X. Lin, S. Guo, K. Tanaka, and S. Hata, "Development of a spherical underwater robot," in Complex Medical Engineering (CME), 2011 IEEE/ICME International Conference on, pp. 662–665, IEEE, 2011.

[3] X. Lin, S. Guo, K. Tanaka, and S. Hata, "Underwater experiments of a water-jet-based spherical underwater robot," in Mechatronics and Automation (ICMA), 2011 International Conference on, pp. 738–742, IEEE, 2011.

[4] F. Michaud, J. Laplante, H. Larouche, A. Duquette, S. Caron, D. Létourneau, and P. Masson, "Autonomous spherical mobile robot for child-development studies," Systems, Man and Cybernetics, Part A: Systems and Humans, IEEE Transactions on, vol. 35, no. 4, pp. 471–480, 2005.

[5] S. Kenyon, D. Creary, D. Thi, and J. Maynard, "A small, cheap, and portable reconnaissance robot," Sensors, and Command, Control, Communications, and Intelligence (C3I) Technologies for Homeland Security and Homeland Defense IV, vol. 5778, no. 1, pp. 434–443, 2005.

[6] M. Seeman, M. Broxvall, A. Saffiotti, and P. Wide, "An autonomous spherical robot for security tasks," in Computational Intelligence for Homeland Security and Personal Safety, Proceedings of the 2006 IEEE International Conference on, pp. 51–55, IEEE, 2006.

[7] Z. Yili, S. Hanxu, J. Qingxuan, S. Chenkun, and Z. Kailiang, "An omni-directional rolling spherical robot with telescopic manipulator," in Systems and Control in

Aerospace and Astronautics, 2008. ISSCAA 2008. 2nd International Symposium on, pp. 1–6, IEEE, 2008.

[8] P. Appelqvist, Mechatronics Design of a Robot Society: A Case Study of Minimalist Underwater Robots for Distributed Perception and Task Execution. Helsinki University of Technology, 2000.

[9] D. Liu, H. Sun, and Q. Jia, "A family of spherical mobile robot: Driving ahead motion control by feedback linearization," in Systems and Control in Aerospace and Astronautics, 2008. ISSCAA 2008. 2nd International Symposium on, pp. 1–6, IEEE, 2008.

[10] J. Alves and J. Dias, "Design and control of a spherical mobile robot," Proceedings of the Institution of Mechanical Engineers, Part I: Journal of Systems and Control Engineering, vol. 217, no. 6, pp. 457–467, 2003.

[11] Q. Zhan, Y. Cai, and C. Yan, "Design, analysis and experiments of an omni-directional spherical robot," in Robotics and Automation (ICRA), 2011 IEEE International Conference on, pp. 4921–4926, IEEE, 2011.

[12] Y. Ming, D. Zongquan, Y. Xinyi, and Y. Weizhen, "Introducing hit spherical robot: dynamic modeling and analysis based on decoupled subsystem," in Robotics and Biomimetics, 2006. ROBIO'06. IEEE International Conference on, pp. 181–186, IEEE, 2006.

[13] "Rotundus website." http://www.rotundus.se. Accessed May 22, 2012.

[14] G. Schroll, DYNAMIC MODEL OF A SPHERICAL ROBOT FROM FIRST PRINCIPLES. PhD thesis, Colorado State University, 2010.

[15] F. Michaud and S. Caron, "Roball, the rolling robot," Autonomous robots, vol. 12, no. 2, pp. 211–222, 2002.

[16] B. Zhao, P. Wang, H. Hu, M. Li, and L. Sun, "Study on turning in place of a spherical robot based on stick-slip principle," in Robotics and Biomimetics (ROBIO), 2009 IEEE International Conference on, pp. 771–775, IEEE, 2009.

[17] B. Zhao, M. Li, H. Yu, H. Hu, and L. Sun, "Dynamics and motion control of a two pendulums driven spherical robot," in Intelligent Robots and Systems (IROS), 2010 IEEE/RSJ International Conference on, pp. 147–153, IEEE, 2010.

[18] J. Yoon, S. Ahn, and Y. Lee, "Spherical robot with new type of two-pendulum driving mechanism," in Intelligent Engineering Systems (INES), 2011 15th IEEE International Conference on, pp. 275–279, IEEE, 2011.

[19] R. Mukherjee, M. Minor, and J. Pukrushpan, "Simple motion planning strategies for spherobot: a spherical mobile robot," in Decision and Control, 1999. Proceedings of the 38th IEEE Conference on, vol. 3, pp. 2132–2137, IEEE, 1999.

[20] N. Chadil, M. Phadoongsidhi, K. Suwannasit, P. Manoonpong, and P. Laksanacharoen, "A reconfigurable spherical robot," in Robotics and Automation (ICRA), 2011 IEEE International Conference on, pp. 2380–2385, IEEE, 2011.

[21] P. Jearanaisilawong, S. Laksanacharoen, V. Piriyawong, and K. Swatdipisal, "Design of a three-legged reconfigurable spherical shape robot," in Advanced Intelligent Mechatronics, 2009. AIM 2009. IEEE/ASME International Conference on, pp. 1730–1733, IEEE, 2009.

[22] Y. Kim, S. Ahn, and Y. Lee, "Kisbot: new spherical robot with arms," in 10th WSEAS International Conference on Robotics, Control and Manufacturing Technology, Hangzhou, China, pp. 63–67, 2010.

[23] B. Li, Q. Deng, and Z. Liu, "A spherical hopping robot for exploration in complex environments," in Robotics and Biomimetics (ROBIO), 2009 IEEE International Conference on, pp. 402–407, IEEE, 2009.

[24] M. Artusi, M. Potz, J. Aristizabal, C. Menon, S. Cocuzza, and S. Debei, "Electroactive elastomeric actuators for the implementation of a deformable spherical rover," IEEE/ASME Transactions on Mechatronics, vol. 16, no. 1, 2011.

[25] K. Wait, P. Jackson, and L. Smoot, "Self locomotion of a spherical rolling robot using a novel deformable pneumatic method," in Robotics and Automation (ICRA), 2010 IEEE International Conference on, pp. 3757–3762, IEEE, 2010.

[26] T. Yamanaka, S. Nakaura, and M. Sampei, "Hopping motion analysis of'superball'-like spherical robot based on feedback control," in Intelligent Robots and Systems, 2003.(IROS 2003). Proceedings. 2003 IEEE/RSJ International Conference on, vol. 4, pp. 3805–3810, IEEE, 2003.

[27] Y. Sugiyama, A. Shiotsu, M. Yamanaka, and S. Hirai, "Circular/spherical robots for crawling and jumping," in Robotics and Automation, 2005. ICRA 2005. Proceedings of the 2005 IEEE International Conference on, pp. 3595–3600, IEEE, 2005.

[28] K. Au and Y. Xu, "Decoupled dynamics and stabilization of single wheel robot," in Intelligent Robots and Systems, 1999. IROS'99. Proceedings. 1999 IEEE/RSJ International Conference on, vol. 1, pp. 197–203, IEEE, 1999.

[29] H. Brown Jr and Y. Xu, "A single-wheel, gyroscopically stabilized robot," in Robotics and Automation, 1996. Proceedings., 1996 IEEE International Conference on, vol. 4, pp. 3658–3663, IEEE, 1996.

[30] G. Shu, Q. Zhan, and Y. Cai, "Motion control of spherical robot based on conservation of angular momentum," in Mechatronics and Automation, 2009. ICMA 2009. International Conference on, pp. 599–604, IEEE, 2009.

[31] V. Joshi and R. Banavar, "Motion analysis of a spherical mobile robot," Robotica, vol. 27, no. 3, p. 343, 2010.

[32] V. Joshi, R. Banavar, and R. Hippalgaonkar, "Design, modeling and controllability of a spherical mobile robot," Proceedings of the 13th National Conference on Mechanisms and Machines (NaCoMM07), 12–13 December 2007.

[33] J. Qingxuan, Z. Yili, S. Hanxu, C. Hongyu, and L. Hongyi, "Motion control of a novel spherical robot equipped with a flywheel," in Information and Automation, 2009. ICIA'09. International Conference on, pp. 893–898, IEEE, 2009.

[34] M. Carpenter and M. Peck, "Dynamics of a high-agility, low-power coelostat telescope," Proceedings of 2006 AIAA Guidance, Navigation, and Control Conference and Exhibit, Keystone, CO, USA, 24 August 2006.

[35] J. Aubrun and G. Margulies, "Gyrodampers for large space structures," NASA Contractor Report 159171; Lockheed Palo Alto Research Laboratory: Palo Alto, CA, USA, 1979.

[36] M. Peck, "Low-power, high-agility space robotics," in 2005 AIAA Guidance, Navigation, and Control Conference and Exhibit, pp. 1–12, 2005.

[37] G. SCHROLL, "Angular momentum torque enhancement for spherical vehicles," May 20 2010. WO Patent WO/2010/057,129.

[38] M. Carpenter, "Power-optimal steering of a space robotic system driven by control-moment gyroscopes," Proceedings of 2008 AIAA Guidance, Navigation and Control Conference and Exhibit, Honolulu, HI, USA, 21 August 2008.

[39] D. Brown, "Control moment gyros as space-robotics actuators," AIAA Guidance, Navigation, and Control Conference, 2008.

[40] M. Peck, M. Paluszek, S. Thomas, and J. Mueller, "Control-moment gyroscopes for joint actuation: a new paradigm in space robotics," 2005.

[41] D. Brown and M. Peck, "Scissored-pair control moment gyros: A mechanical constraint saves power," Journal of Guidance, Control, and Dynamics, to appear, 2008.

[42] J. Peraire, Dynamics: L30: 3D Rigid Body Dynamics: Tops and Gyroscopes, vol. 2.0. MIT: Open Courseware, 2008.

[43] G. Schroll, Design of a spherical vehicle with flywheel momentum storage for high torque capabilities. Doctoral thesis, 2008.

[44] D. Brown and M. Peck, "Energetics of control moment gyroscopes as joint actuators," Journal of guidance, control, and dynamics, vol. 32, no. 6, 2009.

ABSTRACT

ANALYSIS OF A DUAL SCISSORED-PAIR,VARIABLE-SPEED, CONTROL MOMENT GYROSCOPE DRIVEN SPHERICAL ROBOT

by

RICHARD CHASE

May 2014

Advisor: Dr. Abhilash Pandya

Major: Electrical Engineering

Degree: Doctor of Philosophy

The objective of this research is to compare barycenter offset based designs of spherical robots to control moment gyroscope (CMG) based designs in order to determine which approach is most effective. The first objective was to develop a list of current state of the art designs in order to gain an overall understanding of what the obstacles in this area of research were. The investigation showed that barycenter offset designs can produce a low, continuous output torque, whereas CMG based designs can usually only produce a high, momentary output torque. The second objective was to develop a CMG based design that has the potential to outperform current state barycenter offset based designs. A design consisting of a dual, scissored-pair CMG (DSP-VSCMG) configuration was proposed and the dynamics derived from first principles. The third objective was to develop a set of equations that can describe performance characteristics of spherical robots . The equations that were modeled were power consumption, translational velocity, maximum incline plane, step size from rest, as well as CMG inertias and geometries. The fourth objective was to perform a series of parametric analysis using the developed equation set to compare barycenter and DSP-VSCMG based designs in a controlled environment. The analysis showed that DSP-VSCMG based designs can be more agile than barycenter designs, but require more power to do so.

AUTOBIOGRAPHICAL STATEMENT

Richard Chase received his Undergraduate at Wayne State University in Electrical Engineering. He went on to study at the University of Michigan Dearborn where he received his Master's degree in Electrical Engineering with a concentration in signal theory. He received his Ph.D from Wayne State University in August 2013. He also earned his professional engineering license in the state of Michigan. His work experience has focused on developing innovative army technologies for the Department of Defense since 2004. He is currently a lead research scientist at U.S. Army TARDEC.

In his spare time, Richard is active in the arts community in Detroit, Michigan. He has had sculptures in shows around the city and at some large events such as MOVEMENT and Dally in the Alley. He is also active in the community, and has worked on building one of the premiere public gardens in Detroit's Midtown and does regular volunteer work with local urban animal farms.